

NASA Contractor Report 181818

MODELING AND CHARACTERIZATION OF THE EARTH RADIATION BUDGET EXPERIMENT (ERBE) NONSCANNER AND SCANNER SENSORS

**Nesim Halyo
Dhirendra K. Pandey
Deborah B. Taylor**

INFORMATION & CONTROL SYSTEMS, INCORPORATED
28 RESEARCH DRIVE
HAMPTON, VIRGINIA 23666

CONTRACT NAS1-18018
March 1989



National Aeronautics and
Space Administration

Langley Research Center
Hampton, Virginia 23665

FOREWORD

The work described in this report was performed by Information & Control Systems, Incorporated under Contract Number NAS1-18018 for the National Aeronautics and Space Administration, Langley Research Center, Hampton, Virginia. Mr. Robert J. Keynton was the NASA Technical Representative for this contract. Dr. Nesim Halyo directed the technical effort at ICS.

TABLE OF CONTENTS

	page
Foreword.....	11
List of Figures.....	vi
List of Tables.....	x
PART I: MODELING AND CHARACTERIZATION OF THE EARTH RADIATION BUDGET EXPERIMENT (ERBE) NONSCANNER SENSORS.....	
1. Introduction.....	1
2. Nonscanner Sensors.....	3
2.1 Description.....	3
2.1.1 Basic Operations.....	3
2.1.2 Sensor Modeling.....	11
2.2 Total Wavelength Channels.....	15
2.2.1 Active Cavity Power Balance.....	15
2.2.2 Active Heater Electronics.....	17
2.2.3 Reference Cavity.....	20
2.3 Shortwave Channels.....	20
2.4 Sensor Data Interpretation Algorithm Development...	24
2.4.1 Steady-State Sensor Models.....	24
2.4.2 Total Wavelength Channels.....	25
2.4.3 Shortwave Channels.....	31
2.5 Sensor Data Output Interpretation Algorithm.....	34
2.5.1 Total Wavelength Channels.....	34
2.5.2 Shortwave Channels.....	36

TABLE OF CONTENTS (CONTINUED)

	page
3. Ground Calibration.....	37
3.1 Description of Calibration Sources.....	37
3.1.1 Master Reference Blackbody (MRBB).....	37
3.1.2 Integrating Sphere (IS).....	41
3.2 Count Conversion Equations.....	41
3.3 Calibration Data Background.....	42
3.3.1 ERBS Calibration Data.....	42
3.3.2 NOAA-9 Calibration Data.....	42
3.3.3 NOAA-10 Calibration Data.....	43
3.4 Ground Count Conversion Coefficients Results.....	43
4. In-Flight Calibration.....	48
4.1 In-Flight Calibration Sources.....	48
4.2 In-Flight Count Conversion Equations.....	48
4.2.1 Total Channels.....	48
4.2.2 Shortwave Channels.....	50
4.2.3 Dome Degradation Factor.....	50
4.2.4 A_F Term of NOAA-9 Shortwave Channels.....	57
4.3 Total Channel Offsets.....	57
4.4 Shortwave Channel Offsets.....	59
4.4.1 NOAA-10 Shortwave Offsets Determination.....	66
4.5 Final In-Flight Count Conversion Coefficients.....	83
4.5.1 ERBS Nonscanner Results.....	83
4.5.2 NOAA-9 Nonscanner Results.....	93
4.5.3 NOAA-10 Nonscanner Results.....	93

TABLE OF CONTENTS (CONCLUDED)

	page
References.....	103
Appendix A Configuration Factor.....	104
Appendix B $B_{MRBB-IBB}$ Correction Factor.....	106
Appendix C Solar Calibration Data.....	107
PART II: MODELING AND CHARACTERIZATION OF THE EARTH RADIATION BUDGET EXPERIMENT (ERBE) SCANNER SENSORS.....	
I. Introduction.....	114
II. Scanner Description and Modeling.....	117
A. Spectral Considerations.....	122
B. Scanner Dynamic Model.....	130
C. Effective Point Spread Function.....	139
D. Interpretation Algorithms (Count Conversion).....	151
III. Calibration.....	153
A. Calibration Sources.....	153
B. Calibration Procedures.....	157
1. Total and Longwave Channels.....	159
2. Shortwave Channels.....	161
C. In-Flight Offset Stability.....	162
D. SWICS Stability.....	162
E. "Striping" Algorithm.....	167
References.....	170

LIST OF FIGURES

	page
PART I: CALIBRATION AND INTERPRETATION OF THE EARTH RADIATION BUDGET EXPERIMENT (ERBE) NONSCANNER SENSORS	
Figure 2.1 Nonscanner Total Channel.....	4
Figure 2.2 Nonscanner Shortwave Channel.....	5
Figure 2.3a Electronic Block Diagram.....	7
Figure 2.3b Active Cavity Feedback.....	8
Figure 2.3c Nonscanner Electronics (ACR).....	9
Figure 2.4 Angle Conventions.....	13
Figure 2.5 Transmission of 1mm SUPRASIL-W.....	22
Figure 3.1 ERBE Calibration Chamber.....	38
Figure 3.2 Cross section of Master Reference Blackbody (MRBB)...	39
Figure 3.3 Integrating Sphere.....	40
Figure 4.1 Nonscanner Elevation Positions.....	49
Figure 4.2 Solar Measurement vs Calibration Day For ERBS MFOVSW Sensor.....	51
Figure 4.3 Solar Measurement vs Calibration Day For ERBS WFOVSW Sensor.....	52
Figure 4.4 Solar Measurement vs Calibration Day For NOAA-9 MFOVSW Sensor.....	53
Figure 4.5 Solar Measurement vs Calibration Day For NOAA-9 WFOVSW Sensor.....	54
Figure 4.6 Solar Measurement vs Calibration Day For NOAA-10 MFOVSW Sensor.....	55
Figure 4.7 Solar Measurement vs Calibration Day For NOAA-10 WFOVSW Sensor.....	56
Figure 4.7a MFOVSW (Nighttime) Energy vs MFOVSW FOVL Temperature, T_F	58

LIST OF FIGURES (CONTINUED)

	page
Figure 4.8 Offset Variation Obtained By Using IBB Data vs Calibration Day For ERBS MFOVT Channel.....	60
Figure 4.9 Offset Variation Obtained By Using IBB Data vs Calibration Day For ERBS WFOVT Channel.....	61
Figure 4.10 Offset Variation Obtained By Using IBB Data vs Calibration Day For NOAA-9 MFOVT Channel.....	62
Figure 4.11 Offset Variation Obtained By Using IBB Data vs Calibration Day For NOAA-9 WFOVT Channel.....	63
Figure 4.12 Offset Variation Obtained By Using IBB Data vs Calibration Day For NOAA-10 MFOVT Channel.....	64
Figure 4.13 Offset Variation Obtained By Using IBB Data vs Calibration Day For NOAA-10 WFOVT Channel.....	65
Figure 4.14 Estimated Shortwave Energy (Orbital Average) From Darkside Data Analysis For ERBS MFOVSW Channel For April 1985.....	69
Figure 4.15 Estimated Shortwave Energy (Daily Average) From Darkside Data Analysis For ERBS MFOVSW Channel For April 1985.....	70
Figure 4.16 Final Offset Term For ERBS MFOVSW Channel For April 1985.....	71
Figure 4.17 Estimated Shortwave Energy (Orbital Average) From Darkside Data Analysis For ERBS WFOVSW Channel For April 1985.....	72
Figure 4.18 Estimated Shortwave Energy (Daily Average) From Darkside Data Analysis For ERBS WFOVSW Channel For April 1985.....	73
Figure 4.19 Final Offset Term For ERBS WFOVSW Channel For April 1985.....	74
Figure 4.20 Estimated Shortwave Energy (Orbital Average) From Darkside Data Analysis For NOAA-9 MFOVSW Channel For April 1985.....	75
Figure 4.21 Estimated Shortwave Energy (Daily Average) From Darkside Data Analysis For NOAA-9 MFOVSW Channel For April 1985.....	76

LIST OF FIGURES (CONTINUED)

	page
Figure 4.22 Final Offset Term For NOAA-9 MFOVSW Channel For April 1985.....	77
Figure 4.23 Estimated Shortwave Energy (Orbital Average) From Darkside Data Analysis For NOAA-9 WFOVSW Channel For April 1985.....	78
Figure 4.24 Estimated Shortwave Energy (Daily Average) From Darkside Data Analysis For NOAA-9 WFOVSW Channel For April 1985.....	79
Figure 4.25 Final Offset Term For NOAA-9 WFOVSW Channel For April 1985.....	80
Figure 4.26 Differences In Offset Levels By Looking At Different Data Sources for ERBS WFOVSW Channel.....	81
Figure 4.27 Differences In Offset Levels By Looking At Different Data Sources for NOAA-9 WFOVSW Channel.....	82
Figure 4.28 Differences In Offset Levels By Looking At Different Data Sources for ERBS MFOVSW Channel.....	85
Figure 4.29 Differences In Offset Levels By Looking At Different Data Sources for NOAA-9 MFOVSW Channel.....	86
Figure A.1 Representation of Configuration.....	104
 PART II: CALIBRATION AND INTERPRETATION OF THE EARTH RADIATION BUDGET EXPERIMENT (ERBE) SCANNER SENSORS	
Figure 1. ERBE Scanner with Contamination Covers Open.....	116
Figure 2. ERBE Scanner.....	118
Figure 3. Scan Pattern.....	119
Figure 4. Precision Aperture Shape.....	121
Figure 5. Detector Bridge Diagram.....	123
Figure 6. Scanner Electronics Block Diagram.....	124
Figure 7. ERBE Scanner Spectral Response.....	126

LIST OF FIGURES (CONCLUDED)

	page
Figure 8. ERBE Scanner Spectral Response.....	127
Figure 9. ERBE Scanner Spectral Response.....	128
Figure 10. Spectral Considerations.....	129
Figure 11. Scanner Heater Controller Model.....	132
Figure 12. Simulation of ERBE Total Scanner Thermal and Electrical Variables.....	136
Figure 13. Spatial Frequency Response of the Optics.....	145
Figure 14. Shape and Spatial Frequency Response of the Detector Aperture.....	147
Figure 15. Frequency Response of the Electronics as a Function of Cycles/Degrees.....	148
Figure 16. Effective Spatial Frequency Response Function of ERBE Scanners.....	149
Figure 17. Effective Spatial Response of ERBE Scanners.....	150
Figure 18. ERBE Calibration Chamber.....	154
Figure 19. Cross Section of Master Reference Blackbody (MRBB)...	155
Figure 20. Integrating Sphere.....	156
Figure 21. Active Measurements of the ERBE Shortwave Scanner Instrument Scanning the ERBE Integrating Sphere.....	158
Figure 22. NOAA-9 SWICS Amp Output.....	166
Figure 23. NOAA-9 Scanner SW Channel: SWICS Data.....	168

LIST OF TABLES

	page
PART I: CALIBRATION AND INTERPRETATION OF THE EARTH RADIATION BUDGET EXPERIMENT (ERBE) NONSCANNER SENSORS	
Table 3.1 ERBS Flight Model One (FM1) Ground Count Conversion Coefficients.....	44
Table 3.2 NOAA-9 Flight Model Two (FM2) Ground Count Conversion Coefficients.....	45
Table 3.3 NOAA-10 Proto-Flight Model (PFM) Ground Count Conversion Coefficients.....	47
Table 4.1 ERBS Shortwave Offset Determination For April 6, 1985 Using Darkside Data Analysis.....	67
Table 4.2 NOAA-9 Shortwave Offset Determination For April 6, 1985 Using Darkside Data Analysis.....	68
Table 4.3 NOAA-10 WFOVSW Offsets.....	84
Table 4.4 ERBS MFOV Total In-Flight Count Conversion Coefficients.....	87
Table 4.5 ERBS WFOV Total In-Flight Count Conversion Coefficients.....	88
Table 4.6 ERBS MFOV SHORTWAVE In-Flight Count Conversion Coefficients.....	89
Table 4.7 ERBS WFOV Shortwave In-Flight Count Conversion Coefficients.....	91
Table 4.8 NOAA-9 MFOV Total In-Flight Count Conversion Coefficients.....	94
Table 4.9 NOAA-9 WFOV Total In-Flight Count Conversion Coefficients.....	95
Table 4.10 NOAA-9 MFOV Shortwave In-Flight Count Conversion Coefficients.....	96
Table 4.11 NOAA-9 WFOV Shortwave In-Flight Count Conversion Coefficients.....	98
Table 4.12 NOAA-10 MFOV Total In-Flight Count Conversion Coefficients.....	100

LIST OF TABLES (CONCLUDED)

	page
Table 4.13 NOAA-10 WFOV Total In-Flight Count Conversion Coefficients.....	100
Table 4.14 NOAA-10 MFOV Shortwave In-Flight Count Conversion Coefficients.....	101
Table 4.15 NOAA-10 WFOV Shortwave In-Flight Count Conversion Coefficients.....	101
Table A.1 Configuration Factors.....	105
Table B.1 $B_{MRBB-IBB}$ Correction Factors.....	106
Table C.1 ERBS MFOVSW Solar Calibration Data.....	108
Table C.2 ERBS WFOVSW Solar Calibration Data.....	109
Table C.3 NOAA-9 MFOVSW Solar Calibration Data.....	110
Table C.4 NOAA-9 WFOVSW Solar Calibration Data.....	111
Table C.5 NOAA-10 MFOVSW Solar Calibration Data.....	112
Table C.6 NOAA-10 WFOVSW Solar Calibration Data.....	113
PART II: CALIBRATION AND INTERPRETATION OF THE EARTH RADIATION BUDGET EXPERIMENT (ERBE) SCANNER SENSORS	
Table 1. Scanner Electronics.....	133
Table 2. NOAA-9 Count Conversion Equations.....	160
Table 3. ERBE ERBS (FM1) Scanner Data Interpretation Coefficients.....	163
Table 4. ERBE NOAA-10 (FM2) Scanner Data Interpretation Coefficients.....	163
Table 5. ERBE NOAA-9 (PFM) Scanner Data Interpretation Coefficients.....	163
Table 6. ERBS Scanner Offset Stability.....	164
Table 7. ERBS Total Scanner.....	165

PART I

MODELING AND CHARACTERIZATION OF THE EARTH RADIATION BUDGET EXPERIMENT (ERBE) NONSCANNER SENSORS

1. INTRODUCTION

Three Earth Radiation Budget Experiment (ERBE) satellites, namely ERBS, NOAA-9 and NOAA-10 were launched on October 5, 1984, December 5, 1984, September 17, 1986 respectively to measure the radiances from the sun and reflected and emitted radiances from the earth-atmosphere system. The first spacecraft, ERBS, which has a non-sun-synchronous trajectory, is favorable for mid and low latitudes. The other two satellites, NOAA-9 and NOAA-10, which have sun-synchronous trajectories, are favorable for high altitudes. A general overview of the concept behind the three-satellite ERBE radiometric system and its instruments has been described in many internal NASA documents, such as the Science Team Meeting Minutes and Contractor Status Reports, as well as in journal publications [1].

Each ERBE satellite has five nonscanner sensors with active cavity radiometer detectors. Four of them are aimed to measure the radiances leaving the earth-atmosphere system, while the fifth sensor, known as the Solar Monitor, measures the solar incident radiance. One wide and one medium field-of-view sensor make measurements across the total spectral band, while the other two measure the Earth's reflected radiation, which is then subtracted from the total measurements to determine the Earth's emitted radiation. The fifth instrument, the Solar Monitor, uses the same type of Active Cavity Radiometer (ACR) that is used by the nonscanners. Details of these sensors can be found elsewhere [2] - [4]

This report describes the development of governing equations, calibration procedure and interpretation of calibration data to determine the Ground and In-Flight Count Conversion Coefficients for the nonscanner active cavity radiometers. Chapter 2 details the nonscanner instruments and mathematical developments, while Chapters 3 and 4 describe the Ground and In-Flight Count Conversion Coefficients, respectively.

2. NONSCANNER SENSORS

2.1 Description

The ERBE Non-Scanning sensors are state-of-the-art active cavity radiometers (ACR) designed for high accuracy and stability. Each of the three Non-Scanner instruments consists of four sensors. Two of the sensors have a wide field-of-view (WFOV) which provides limb-to-limb coverage of the top of the atmosphere (TOA) plus a “space ring” to accommodate small deviations in spacecraft roll angle and possible installation misalignments. The other two Non-Scanners have a medium field-of-view (MFOV) covering a circular area with a diameter corresponding to about 10° Earth Central Angle at the top of the atmosphere.

The WFOV and MFOV sensors each consist of a Shortwave (SW) and a Total (T) sensor, measuring the spectral bands from $0.2\mu\text{m}$ to $5\mu\text{m}$ and from $0.2\mu\text{m}$ to $50 + \mu\text{m}$, respectively. In comparison to the Total channels, the Shortwave channels contain a suprasil dome filter to filter out the incoming longwave radiation. A schematic diagram showing the major elements of the MFOV-T and the WFOV-SW sensors is shown in Figs. 2.1 and 2.2, respectively. A more detailed description of the ERBE Non-Scanner Instruments can be found in [1] - [3].

2.1.1 Basic Operation.

As shown in Figs. 2.1 and 2.2, the active and reference cavities are cylindrical near the primary aperture and conical near the bottom. The active and reference cavity heater wires are wound around the bottom or conical part of the cavities. Temperature sensing wires are wound around the cylinders which hold the cavities, and thermally connect the cavities to the copper heat sink, shown as node 2 in the schematic diagrams.

The copper heatsink is maintained at a constant temperature by resistance heater windings, as shown in Figs. 2.1 and 2.2. The resistance heater windings extend somewhat

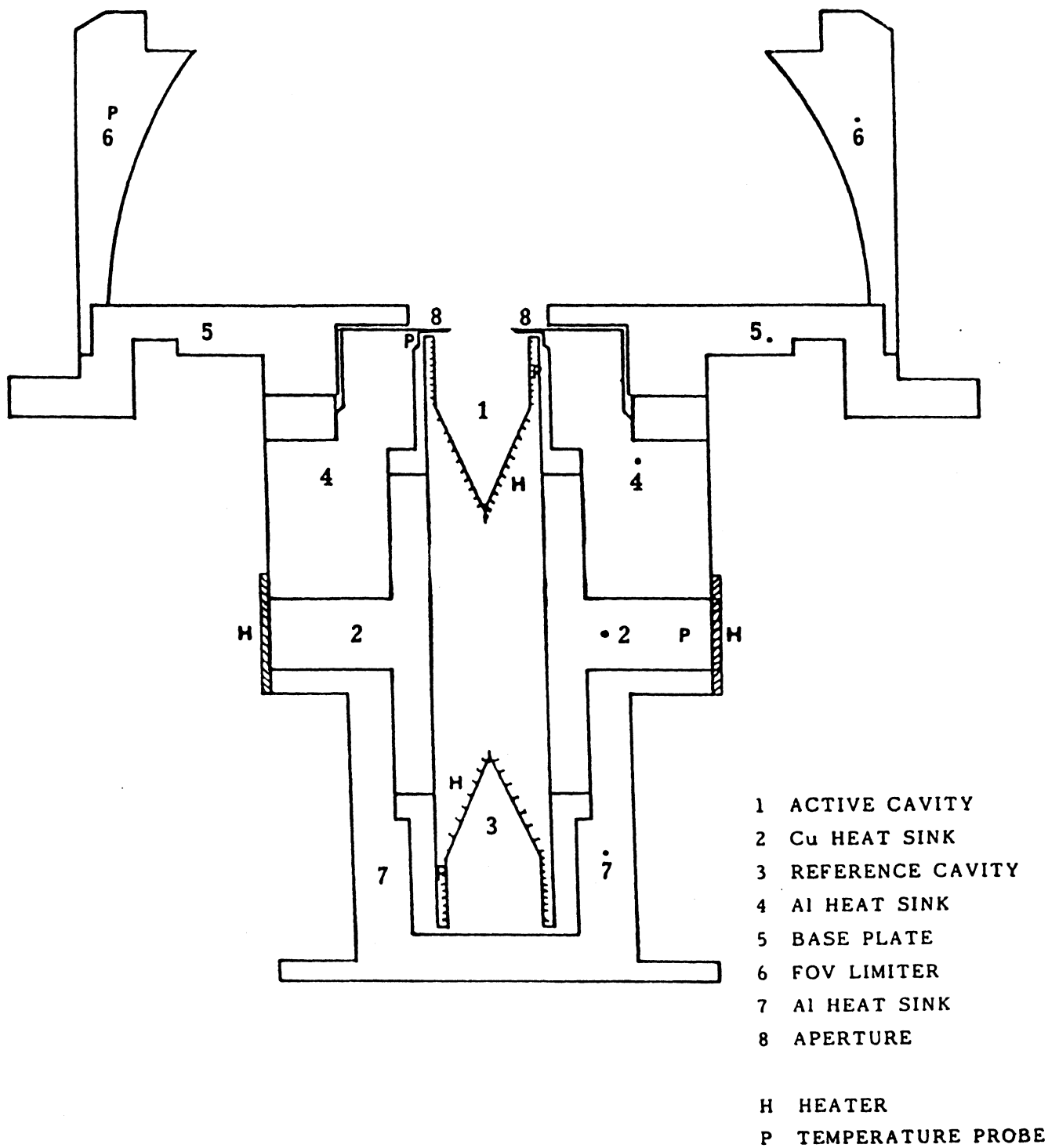


Figure 2.1 Nonscanner Total Channel

beyond the copper heatsink, also adding heat to the two aluminum heatsinks corresponding to nodes 4 and 7. The heatsink has three set temperatures of operation, although normal operation is around 34 °C.

In the normal operation modes, the reference cavity maintains a constant temperature nearly equal to the heatsink temperature. The reference cavity has a conductive path to the copper heatsink; its radiative exchange is mainly with the aluminum heatsink and to a lesser degree with the copper heatsink and the active cavity. In the Earth-looking modes, the reference cavity heater is off, so that the only source of heat to the cavity comes from the current flowing in the temperature sensor wire around the cavity. Since all these effects remain essentially constant, the reference cavity remains at a constant temperature.

On the other hand, the activity cavity has two extra major sources of energy: the radiation arriving through the primary aperture (node 8), and the Joule heating produced by the active cavity heater windings. The radiation arriving through Joule heating produced by the active cavity heater windings. The radiation arriving through the primary aperture consists of radiation arriving through the sensor field-of-view (FOV), or the secondary aperture, which is the signal to be measured, radiation emitted by or reflected from the field-of-view limiter (FOVL) and the baseplate (node 5). The radiative exchange with the primary aperture itself must also be considered.

On the other hand, the active cavity heater, through a feedback control circuit shown in Fig. 2.3, maintains the active cavity temperature approximately $\frac{1}{2}$ °C above the reference cavity temperature. Since the reference cavity temperature remains constant, so does the active cavity temperature. When the radiation arriving from the primary aperture increases, the active cavity heater reduces its heat input by the same amount to maintain the active cavity at a constant temperature. The active cavity heater voltage, in digital format, constitutes the sensor output from which the desired signal is to be estimated.

Thus, the active cavity heater input varies with the energy variations from all other sources. To obtain an estimate of the desired signal (i.e., the radiation arriving through

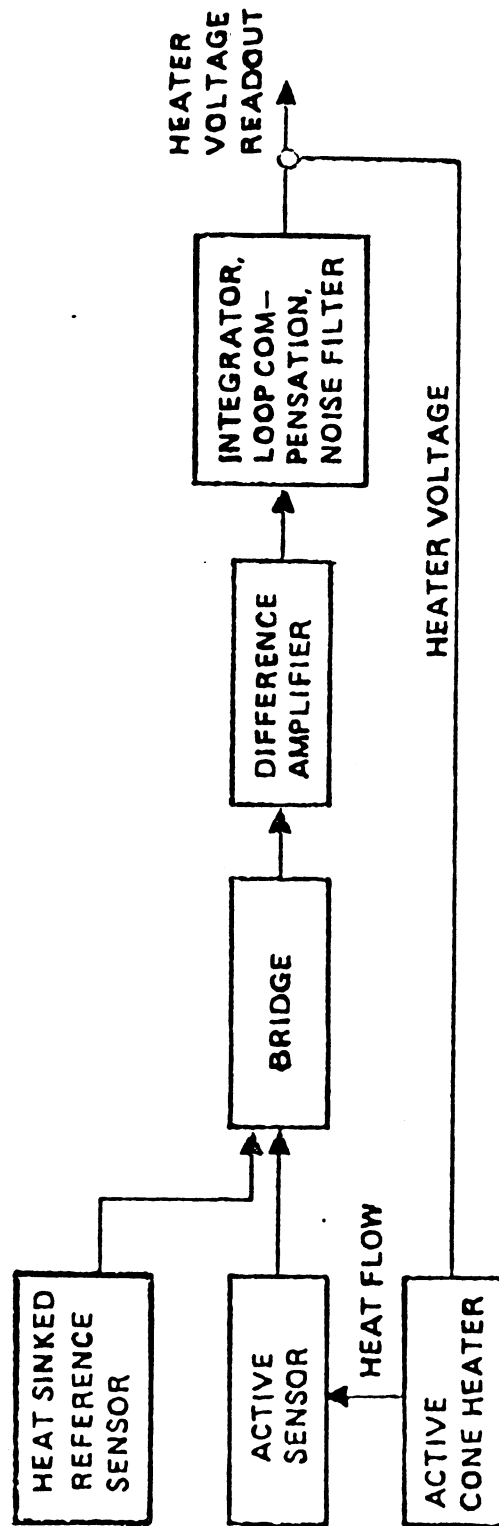
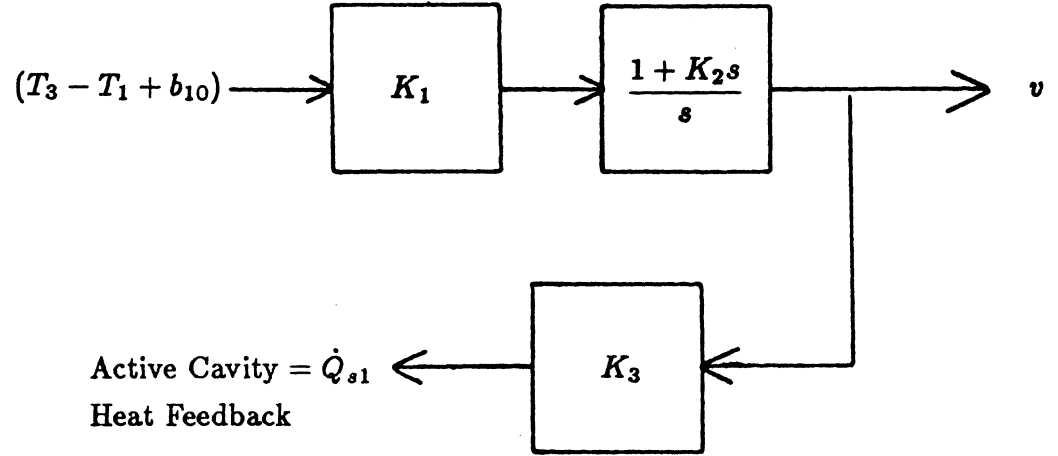


Figure 2.3a Electronic Block Diagram



$$(V_1, \gamma_1 C_1) T_1 = \sum_{j=1}^n \frac{T_j - T_1}{R_{ji}} + A_1 \phi_1 + \dot{Q}_{s1}$$

$$\dot{T}_{10} = K_1(T_3 - T_1 + b_{10}) + n_{10}$$

$$\dot{Q}_{s1} = K_3 T_{10} + K_1 K_2 K_3 (T_3 - T_1 + b_{10})$$

$$v = T_{10} + K_1 K_2 (T_3 - T_1 + b_{10}) + n$$

Figure 2.3b Active Cavity Feedback

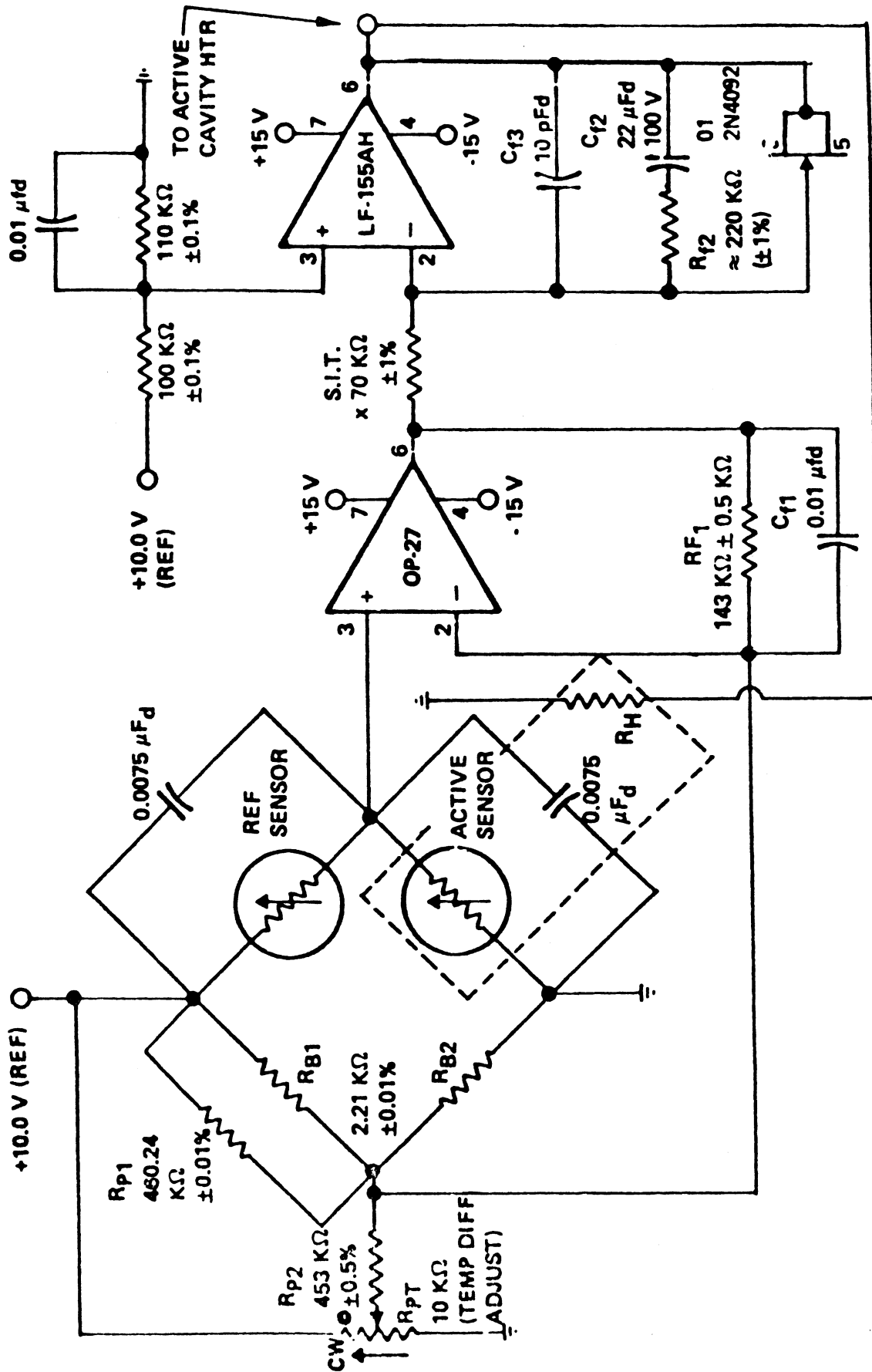


Figure 2.3c Nonscanner Electronics (ACR)

the secondary aperture), it is necessary to carefully eliminate the effects from the other energy sources such as variations due to the field-of-view limiter baseplate, the dome filter and other component temperatures, the energy loss through the conductive path to the Cu heatsink, etc. When all of these effects, most of which are second order, are carefully accounted for and subtracted from the active cavity heater input, the remaining energy is due to absorbed radiation arriving through the sensor field-of-view, which is the desired signal. In the following sections, the radiative, conductive and electrical interactions of the various elements of the radiometers are modeled and investigated in detail to obtain the best estimate of the desired incoming flux.

All the nonscanner sensors have field-of-view limiters and baseplates with specular, characteristics to the extent possible. As the FOVL's are hemispherical with their origin at the center of the primary aperture, this specular characteristic tends to minimize the amount of reflected radiation which enters the active cavity through the primary aperture. This effect may be somewhat reduced in the shortwave channels due to the presence of the dome filter between the FOVL and the active cavity.

As mentioned earlier, in Earth-looking modes, the reference cavity heater is turned off, so that the cavity temperature is nearly equal to the heatsink temperature. However, the sensors can also be operated at three other levels of reference cavity heater voltage. At each of these modes, a higher amount of constant heat is provided to the reference cavity. While some of this energy is emitted, and some conducted to the copper heatsink, the cavity temperature settles at a level higher than the one reached during the normal Earth-looking mode. Thus, the reference cavity temperature reaches a temperature higher than the heatsink temperature. The feedback control electronics drives the active cavity heater input to the level necessary to maintain the active cavity temperature slightly higher than that of the reference cavity.

In these modes, although the active and reference cavities are both at higher temperatures, the principle of operation remains the same at the new operating point. The

active cavity temperature is maintained at a constant, albeit higher, temperature by the feedback control law which compensates exactly for the variations in absorbed energy arriving through the precision aperture. These modes of operation where the active cavity temperature differential over the heatsink temperature is higher, substantially increase the dynamic range of the sensors with no change in the sensitivity of the sensor. In particular, solar calibration, where the signal measured is significantly higher than the one experienced during Earth-looking modes, is performed at a non-zero reference cavity heater voltage.

The field-of-view limiter and the baseplate are thermally isolated from the detector which consists of nodes 1, 2, 3, 4, 7, 8 and 9 shown in the sensor schematic in Figs. 2.1 and 2.2. The baseplate is connected to the detector by a bolt using thermal insulation, but it is connected to the elevation beam through a conductive link to minimize signal induced variations in the FOVL and baseplate.

While the discussion above provides the basic operation of the non-scanning ERBE sensors and describes the major elements of the ACR's, many of the significant details involved in the design and assembly of the sensors are too numerous to be mentioned here. A more detailed description of the sensors is given in [1] - [3].

2.1.2 Sensor Modeling.

The main objective in modeling the ERBE sensors has been to obtain a thorough understanding of the various interrelationships and interactions among the components of the sensors. This involves modeling the radiative exchange, thermal conduction and electronic interactions to form the overall model describing the significant behavior of the sensors. Since the sensors cannot be characterized and calibrated in the actual conditions of orbital operations, it is necessary to infer the sensor response in normal operation from calibration data measured under somewhat different conditions, namely the calibration chamber. A thorough understanding of the sensor under as wide a variety of conditions as possible provides a most reliable approach to achieve this inference with the aid of flight calibration data. Furthermore, ascertaining the stability of the sensors, and interpreting

actual changes in the sensors themselves during the life of the sensors also necessitate a good understanding of the sensors.

While a thorough understanding of the significant sensor response is indispensable, practical considerations limit the level of detail that can be included in a model before extraneous effects, possibly caused by numerical difficulties, limit the usefulness of the model. Therefore, for a given application, a trade-off of the level of detail needed to model what is considered significant in the sensor response is necessary.

As mentioned in the Introduction, the quantity desired is the irradiance, or flux, reaching a point at satellite altitude through the sensor's designated field-of-view and spectral waveband. Using the angle conventions shown in Fig. 2.4, let $L_{E\lambda}(x, y; \psi, \chi)$ be the spectral radiance leaving the top of the atmosphere and arriving at the point (x, y) on the primary aperture from the direction (ψ, χ) . Let Ω_{iT} be the solid angle formed by the secondary aperture at the center of the primary aperture, i.e., at the origin $(0, 0)$, for the i^{th} Total waveband sensor. For example, Ω_{WT} corresponds to the FOV of the Wide Field-of-View Total channel. Similarly, Ω_{MS} corresponds to the FOV of the Medium Field-of-View Shortwave channel.

The desired radiant incidence, or flux, at the point $(0, 0)$ arriving from the top of the atmosphere within the sensor's spectral band and FOV is given by

$$E_{iT} = \iint_{\Omega_{iT}} \int_0^\infty L_{E\lambda}(0, 0; \psi, \chi) d\lambda d\Omega = \iint_{\Omega_{iT}} L_E(0, 0; \psi, \chi) d\Omega \quad , \quad (2.1)$$

$$E_{iS} = \iint_{\Omega_{iS}} \int_0^5 L_{E\lambda}(0, 0; \psi, \chi) d\lambda d\Omega \quad , \quad (2.2)$$

where $L_E(x, y; \psi, \chi)$ is the radiance at (x, y) , and

$$d\Omega = \sin \chi \cos \chi d\chi d\psi \quad . \quad (2.3)$$

Ideally, we would like to measure the radiant incidence, E_{iT} , at an infinitesimally small

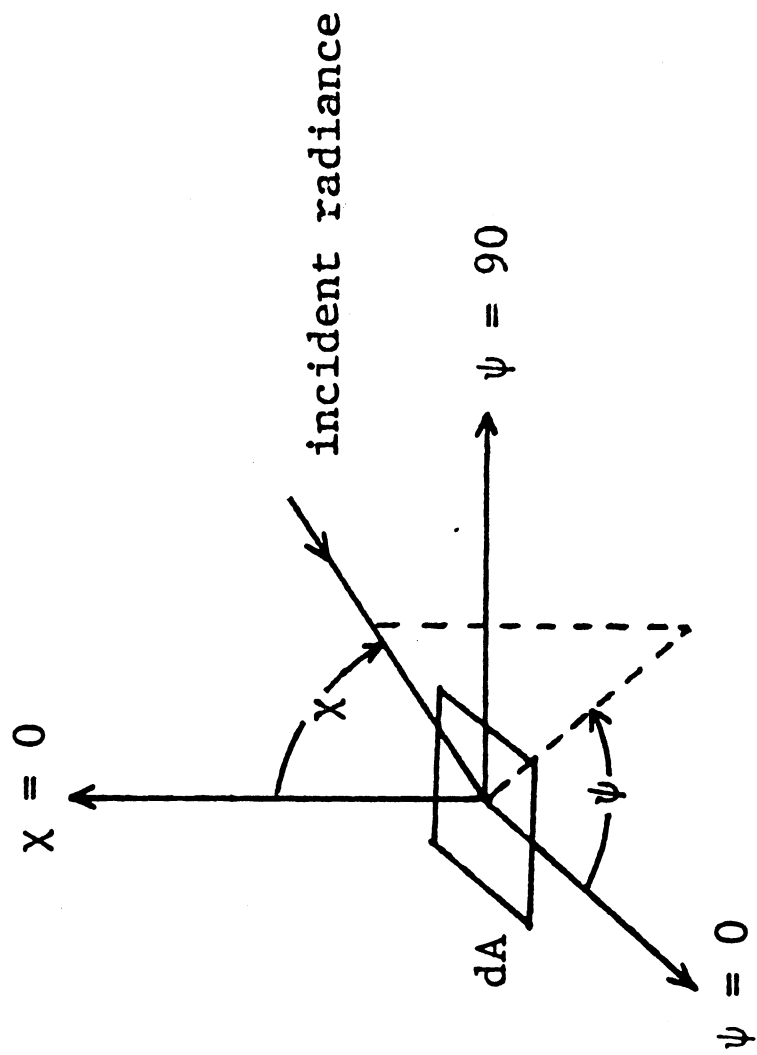


Figure 2.4 Angle Conventions

area or a point. From satellite orbit, it is possible to closely approximate this condition, by spatial averaging over the small primary aperture. Thus, in the Earth-looking modes, the desired irradiance can be expressed as

$$E_{iT} \cong \frac{1}{A_{iT}} \iint_{A_{iT}} \iint_{\Omega_{iT}} \int_0^\infty L_{E\lambda}(x, y; \psi, \chi) d\lambda d\Omega dA = \frac{1}{A_{iT}} \bar{p}_{iT} \quad , \quad (2.4)$$

$$E_{iS} \cong \frac{1}{A_{iS}} \iint_{A_{iS}} \iint_{\Omega_{iS}} \int_0^\infty L_{E\lambda}(x, y; \psi, \chi) d\lambda d\Omega dA = \frac{1}{A_{iS}} \bar{p}_{iS} \quad , \quad (2.5)$$

where A_{iT} , A_{iS} are the areas of the primary aperture opening for the appropriate sensors, and \bar{p}_{iT} , \bar{p}_{iS} represent the power absorbed by an ideal flat plate collector with spectral absorptivity and transmissivity of 1 and perfect cosine angular response over the appropriate field-of-view and spectral band, and over the collector area of A_{iT} or A_{iS} according to the sensor.

Having defined the desired signals, mathematical models which describe the significant sensor behavior and which lead to simple algorithms for estimating the desired fluxes will be developed.

The basic approach taken in modeling the sensors is to develop a lumped-parameter thermal-electronic model by partitioning the sensor into a set of appropriately selected nodes [8]. The selection of nodes used in the model is shown in Figs. 2.1 and 2.2 for the Total and Shortwave channels, respectively.

The energy balance for the j^{th} node can then be expressed as

$$(V_j \gamma_j c_j) \dot{T}_j = \sum_{k=1}^n \frac{T_k - T_j}{R_{jk}} + A_j \phi_j + \dot{Q}_j \quad , \quad 1 \leq j \leq n \quad , \quad (2.6)$$

where V_j , γ_j and c_j are the volume, density and specific heat capacity of the j^{th} node, R_{jk} is the thermal resistance between the j^{th} node, and k^{th} nodes, A_j is the area of radiant interaction for the j^{th} node, ϕ_j is the net flux absorbed by the j^{th} node, T_j the temperature of the j^{th} node and \dot{Q}_j the total power of all heat sources acting on the

j^{th} node. Writing a power balance equation for each node of the sensor, it is possible to obtain a thermal model for the radiative and conductive exchange among the sensor nodes. When a model of the electrical processing and control circuits is adjoined to the thermal exchange, a complete dynamic model of the sensor is obtained.

2.2 Total Wavelength Channels

2.2.1 Active Cavity Power Balance.

The active cavity is the most important node of the sensors as it is the focus of both the thermal and electrical systems. The power balance equation for the active cavity can be expressed as

$$M_1 \dot{T}_1 = \frac{T_2 - T_1}{R_{12}} + \sum_{k=1}^n D_{1k} \sigma T_k^4 + \dot{Q}_a + \dot{Q}_{J1} + p \quad , \quad (2.7)$$

$$M_j = V_j \gamma_j c_j \quad , \quad 1 \leq j \leq n \quad , \quad (2.8)$$

where \dot{Q}_a is the power provided by the active cavity heater windings, \dot{Q}_{J1} the Joule heat power produced by the current flowing in temperature sensor wires, and p the power absorbed by the cavity due to radiation arriving through the primary and secondary apertures. The effects of the radiative interchange between the active cavity and the remaining nodes is modeled here through the distribution factors D_{jk} . The distribution factors can be obtained by Monte Carlo simulation using ray-tracing techniques by standard radiative exchange equations in a cavity using diffuse-grey assumptions or by the coupled-enclosure radiative exchange method developed for approximating complicated cavity geometries.

The active cavity heater power \dot{Q}_a and the sensor wire Joule heating term \dot{Q}_{J1} will be discussed in more detail subsequently. First consider the absorbed power, p_{iT} , by the i^{th} Total sensor, which contains information about the desired irradiance E_{iT} given by Eq. (2.1). Let A_{iT} denote the area of the primary aperture opening of the i^{th} Total sensor and $L_\lambda(x, y; \psi, \chi)$ the spectral radiance arriving through the secondary aperture and entering

the active cavity at the point (x, y) from the direction (ψ, χ) . Then p_T can be expressed as

$$p_{iT} = \iiint_{A_{iT}} \iint_{\Omega_{iT}(x,y)} \int_0^\infty L_\lambda(x, y; \psi, \chi) \alpha_{iT}(\lambda) g_{iT}(\psi, \chi) d\lambda d\Omega dA, i = W, M \quad (2.9)$$

where $\Omega_{iT}(x, y)$ is the solid angle formed by the secondary aperture at the point (x, y) for the i^{th} Total sensor. Except for machining tolerances, the primary aperture for all channels have the same dimensions and edge characteristics, so that

$$A_{WT} \cong A_{MT} \cong A \quad . \quad (2.10)$$

$\alpha_{iT}(\lambda)$ is the effective spectral absorptivity of the inside of the active cavity of the i^{th} sensor, and $g_{iT}(\psi, \chi)$ represents the angular response characteristics of the i^{th} sensor to radiation arriving from the direction (ψ, χ) . It has been assumed that the spectral and angular characteristics of the sensor are separable; i.e., that the product of a function of λ and a function of (ψ, χ) can describe the sensor's combined spectral and directional characteristics.

It should be noted that the effective spectral absorptivity of the active cavity includes the effect of multiple bounces of entering radiation at several points inside the cavity. The selection of the dimensions of the cylindrical and conical portions of the cavities was based on the results of where it is shown that incoming radiation must have at least three bounces before leaving the cavity. Thus, if the cavity paint has an absorptivity of .9, then the effective cavity absorptivity would be .999, or, for all practical purposes, unity.

The geometry and radiative properties of the surfaces of the FOV limiter and baseplate are designed to minimize the amount of reflected radiation that enters the cavity. However, due to imperfections and the finite (non-zero) opening of the primary aperture, some angular nonuniformity in response may occur. The term $g_i(\psi, \chi)$ accounts for deviations

from the ideal “cosine response”; so that for an ideal sensor with a cosine response $g_i(\psi, \chi)$ would be unity for all angles (ψ, χ) .

Comparing Eqs. (2.4) and (2.9), it is seen that the actual absorbed power p_{iT} depends on the actual spectral absorptivity and angular response, as opposed to the ideal absorbed power in Eq. (2.4).

2.2.2 Active Heater Electronics.

As mentioned earlier, the active cavity temperature is maintained at a constant level above the reference cavity temperature. This is achieved by the control circuit shown in Fig. 2.3b. The functional block diagram in Fig. 2.3a shows that the bridge configuration produces a signal proportional to the difference between the active and reference cavity temperatures with an additional offset. This signal is then amplified and fed into a proportional-integral (PI) controller which provides the voltage that drives the current through the active cavity heater windings, thus closing the feedback loop. The voltage is sampled every 0.8 seconds and transmitted to Earth through a down-link, providing the main radiometer sensor output.

To model the electronics, first consider the bridge. The active and reference sensor wires provide two legs of the bridge, while the other two legs are set to constant resistance values. If the active or reference cavities change in temperature the bridge goes out of balance thus forcing the controller to add more or less heat to the active cavity and maintain its temperature.

Now note that the bridge output voltage ΔV is given by

$$\Delta V = V_B \left[\frac{R_1(T_1)}{R_1(T_1) + R_3(T_3)} - B_E \right] , \quad (2.11)$$

$$B_E = \frac{R_4}{R_2 + R_4} , \quad (2.12)$$

where $R_1(T_1)$ and $R_3(T_3)$ are the sensor wire electrical resistances for the active and

reference cavities, respectively, and R_2 and R_4 are the electrical resistances of the copper and aluminum heatsinks, respectively. Linearizing the sensor wire resistance in terms of its temperature, assume that within a small temperature range,

$$R_1(T_1) = a_1 + b_1 T_1 \quad , \quad R_3(T_3) = a_3 + b_3 T_3 \quad . \quad (2.13)$$

It may further be noted that, when the sensor wires are exactly matched,

$$\Delta V \approx K_B(T_1 - T_3 - b_E) \quad , \quad (2.14a)$$

where T_2 is the copper heatsink temperature and K_B , b_E are given by

$$K_B = \frac{V_B b}{4R} \quad (2.14b)$$

$$b_E = 4R(B_E - \frac{1}{2})/b \quad (2.14c)$$

where second order terms have been neglected. So that the bridge will come to balance when the active cavity temperature is slightly higher than that of the reference cavity. Although the sensor wires are selected to have as close characteristics as possible, perfect matching is not essential to the basic operation. After some manipulation, it can be shown that the bridge balance will occur when

$$T_1 = \frac{(a_1 + a_3)B_E - a_1}{b_1(1 - B_E)} + \frac{b_3 B_E}{b_1(1 - B_E)} T_3 \quad . \quad (2.15)$$

It is seen that appropriate selection of the electronic bias term B_E by tuning the resistances R_2 and R_4 , can produce any desired offset between the active and reference cavity temperatures.

It should also be noted that any drift in the sensor wire resistance versus temperature parameters or other bridge impedances will alter the bridge balance and result in slightly

different temperature relationship between T_1 and T_3 .

Further note that since the resistance versus temperature characteristics depend on the operating heat sink temperature, T_2 . The Cu heat sink temperature is, therefore, very tightly controlled. To date, the data show that noticeable variations of the heat sink temperature are rare and do not exceed 0.01 °C.

To obtain a dynamic model of the amplifier and proportional-integral (PI) controller feedback the following equations can be added to the energy (power) balance equations.

$$\dot{T}_9 = K_A K_E \Delta V + K_E n_E \quad (2.16)$$

$$\dot{T}_{10} = \frac{1}{\tau_3} [T_9 - T_{10} + \tau_1 (K_A K_E \Delta V + K_E n_E)] \quad (2.17)$$

$$\dot{T}_{11} = \frac{1}{\tau_4} \{T_{10} - T_{11} + \frac{\tau_2}{\tau_3} [T_9 - T_{10} + \tau_1 (K_A K_E \Delta V + K_E n_E)]\} \quad (2.18)$$

$$v = T_{11} + n_v \quad (2.19)$$

where T_9, T_{10}, T_{11} are variables representing electrical quantities rather than temperatures, n_E and n_v represent random noise introduced by the electronics, and v is the sensor output voltage which is applied to the active cavity heater windings.

Thus, the active cavity heater closes the loop according to

$$\dot{Q}_a = v^2 / R_a \quad , \quad (2.20)$$

where R_a is the electrical resistance of the active heater windings, and \dot{Q}_a the power added to the active cavity in Eq. (2.7).

2.2.3 Reference Cavity.

The reference cavity power balance can be written according to the general Eq. (2.6).

$$M_3 \dot{T}_3 = \frac{T_2 - T_3}{R_{32}} + \sum_{k=1}^n D_{3k} \sigma T_k^4 + \dot{Q}_r + \dot{Q}_{J3} \quad (2.21)$$

In the case of the reference cavity, the heater, \dot{Q}_r is not in the feedback loop, but is driven by a constant voltage, v_r , when the appropriate operation mode is selected. Thus,

$$\dot{Q}_r = \frac{v_r^2}{R_r} \quad (2.22)$$

Using the general energy balance equation in Eq. (2.6), each node temperature can be modeled by a differential equation. The combined set of these coupled ordinary differential equations forms a dynamic model of the sensor. The results of a sensitivity analysis based on a computer simulation of this thermal-electronic model is shown in [8].

2.3 Shortwave Channels

The model of the Shortwave sensors differs from that of the Total wavelength sensors only for the active cavity, the dome filter and the primary aperture to which the dome filter is attached. The form of the energy balance equation for the other nodes remains unchanged, except that radiative interaction among the field-of-view limiter, baseplate, primary aperture and the active cavity is now included.

The major effect of the quartz dome is to filter out longwave radiation before it is absorbed by the active cavity. Thus, longwave radiation is partially absorbed and partially reflected by the dome filter with no transmission occurring. This produces a secondary but non-negligible effect in the radiative exchange. When the longwave radiation in the observed scene increases, more heat is absorbed by the dome. So that the dome temperature, hence the radiation emitted by the dome increases. Accordingly, when the observed longwave radiation increases, the active cavity receives more (longwave) energy

with a lag, even if the scene shortwave radiation is unchanged. Therefore, the model of the Shortwave sensors must account for this secondary effect so that a variation in longwave radiation is not interpreted as a variation in shortwave radiation.

The power balance for the active cavity can be expressed as

$$M_1 \dot{T}_1 = \frac{T_2 - T_1}{R_{12}} + \sum_{k=1}^m D_{1k} \sigma T_k^4 + \dot{Q}_a + \dot{Q}_{J1} + p \quad , \quad (2.23)$$

where the number of nodes m for the Shortwave channels include the dome filter and exceeds the number of nodes for the total wavelength channels by one.

For the active cavity, the absorbed power, p , with appropriate subscripts for the channel, is highly dependent on the spectral transmissivity of the dome filter, as can be seen in Fig. 2.2. Thus, the expression for the absorbed power becomes

$$p_{is} = \iint_{A_{is}} \iint_{\Omega_{is}(x,y)} \int_0^\infty L_\lambda(x,y;\psi,\chi) \tau_{is}(\lambda) \alpha_{is}(\lambda) g_{is}(\psi,\chi) d\lambda d\Omega dA \quad (2.24)$$

where $\Omega_{is}(x,y)$ is the solid angle formed by the secondary aperture when viewed from the point (x,y) on the primary aperture opening and τ_{is} is the spectral transmissivity of the dome filter for i^{th} shortwave sensor.

The spectral transmissivity of the fused quartz dome filter used in the ERBE shortwave sensor is shown in Fig. 2.5. As can be seen from the plot, the transmission of the filter after $5\mu\text{m}$ is negligible, as these measurements do not show a noticeable “longwave leak” after $50\mu\text{m}$. It should be noted, however, that the approach taken here in determining the shortwave channel coefficients would automatically include the effects of any longwave transmission.

To model the dome filter heating effects, the power balance for the dome, or node 9, can be expressed as

$$M_9 \dot{T}_9 = \frac{T_8 - T_9}{R_{98}} \frac{T_4 - T_9}{R_{94}} + \sum_{k=1}^m D_{9k} \sigma T_k^4 + p_f \quad , \quad (2.25)$$

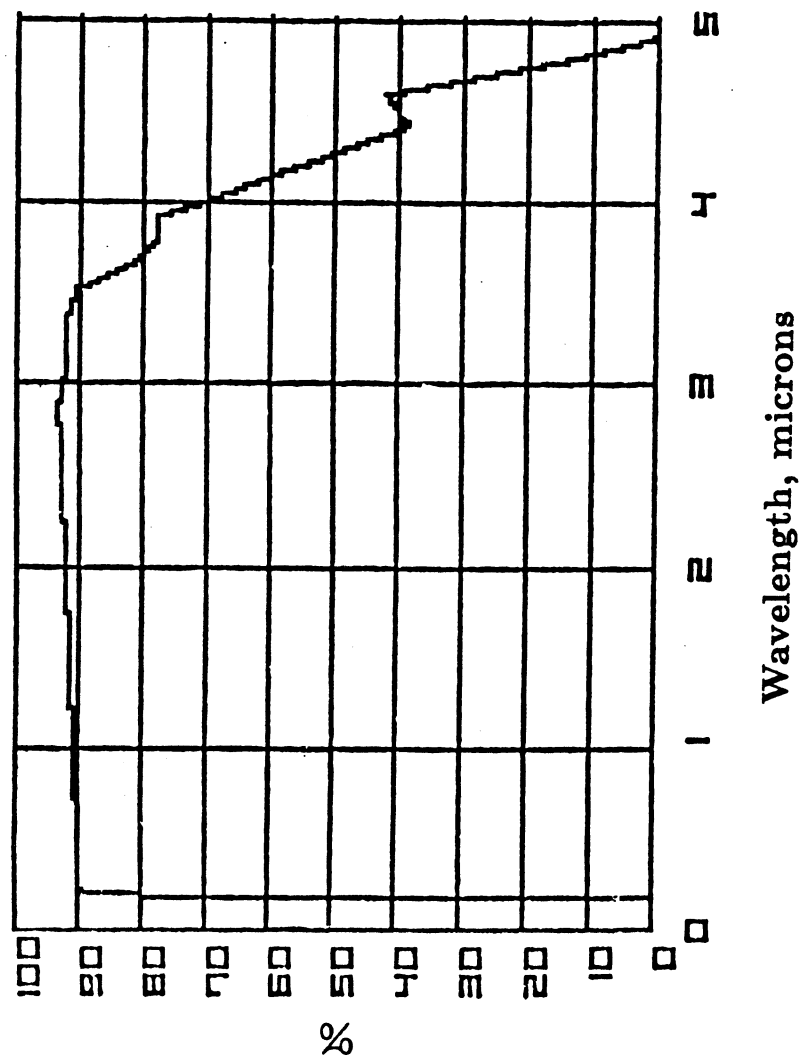


Figure 2.5 Transmission of 1mm SUPRASIL-W

where p_f is the power arriving through the secondary aperture which is absorbed by the dome filter. This power can be expressed in a form similar to the power absorbed by the active cavity.

$$p_{if} = \iint_{A_{if}} \iint_{\Omega_{if}(x,y)} \int_0^\infty L_{f\lambda}(x, y; \psi, \chi) \alpha_{if}(\lambda) g_{if}(\phi, \chi) d\lambda d\Omega dA, \quad i = W_1 M_1 \quad (2.26)$$

where $\alpha_{if}(\lambda)$ is the spectral absorptivity of the dome filter and $g_{if}(\chi, \psi)$ the angular response of the filter relative to a cosine response for the i^{th} sensor. Similarly A_{if} is the outer surface area of the dome which sees the secondary aperture, and $\Omega_{if}(x, y)$ is the solid angle formed by the secondary aperture when viewed from the point (x, y) on A_{if} .

The power balance equation for the dome shows the effect of absorbed longwave radiation on the dome temperature. It should be noted that the FOV limiter and baseplate temperatures are influenced by the variations in absorbed energy from the scene and participate in the radiative exchange with the dome filter. However, the FOV limiter and baseplate are conductively linked to the box beam, whereas the dome filter is a poor conductor and is thermally insulated from the primary aperture to which it is glued. Thus, the temperature of the dome filter varies with the longwave content of the scene and the temperature of the FOVL, baseplate and the primary aperture which is conductively coupled to the heat sink. However, the dome temperature lags the incoming longwave flux as can be seen by Eq. (2.25). Linearizing the power balance equation, the time constant for this differential equation can be found to be

$$\tau = M_9 \left(\frac{1}{R_{98}} + \frac{1}{R_{94}} - 4 \sigma D_{19} T_{90}^3 \right) \quad (2.27)$$

where T_{90} is the nominal dome temperature.

For the shortwave, or filtered, channels it is seen that when the longwave radiation is a ramp of 1 W/m² sec, the shortwave channel output has a lag of about 40 sec.

2.4 Sensor Data Interpretation Algorithm Development

The dynamic sensor models discussed in the preceding section are coupled nonlinear differential equations which describe the dynamic response of the sensors to incoming radiation under given conditions. On the other hand, to interpret the sensor output (radiometric and housekeeping data) in normal operation, what is required is a (sensor) data interpretation algorithm (SDIA) which estimates the magnitude of the incoming radiation from the sensor's radiometric and housekeeping data input. Viewing the sensor as a transformation from the set of incoming radiation signals into the set of sensor outputs, it is necessary to determine the inverse transformation which maps the sensor output back into the corresponding input irradiance.

The determination of this inverse transformation for the dynamic (i.e., time dependent) models is a complex process which results in a rather complex algorithm to implement. Therefore, the approach taken here is to determine the steady-state model of the sensor, then invert this model to obtain an algorithm for interpreting the sensor output. In most cases, as the non-scanner footprint, hence the incoming radiation signal, changes slowly in comparison to the sensor settling time, neglecting the transient behavior in the normal Earth-looking modes introduces little error. In modes of operation where the sensor transient response has not died down, the steady-state assumption should not be used.

2.4.1 Steady-State Sensor Models.

The steady-state sensor response is obtained by allowing sufficient time for the sensor's transient response to decay to negligible levels while the incoming radiation remains constant. In this condition, the temperature of each node reaches a constant value; however, thermal gradients are still present in the steady-state response. Thus, the energy or power balance equation for the steady-state condition is obtained by simply setting the time derivative of the node temperatures, \dot{T}_j , to zero in Eq. (2.6); i.e.,

$$\sum_{k=1}^n \frac{T_k - T_j}{R_{jk}} + A_j \phi_j + \dot{Q}_j = 0 \quad , \quad 1 \leq j \leq n \quad . \quad (2.28)$$

2.4.2 Total Wavelength Channels.

The active cavity power balance in steady-state can be written as follows using Eq. (2.7) and Eq. (2.20):

$$p = \frac{T_1 - T_2}{R_{12}} - \sum_{k=1}^n D_{1k} \sigma T_k^4 - \frac{v^2}{R_a} - \dot{Q}_{J1} \quad , \quad (2.29)$$

where p with appropriate subscripts is given by Eq. (2.9) and represent the steady-state signal power absorbed by the active cavity, and v is the steady-state voltage output of the sensor.

Now, for a given amount of absorbed power, the active heater control electronics reacts, as described in the previous section, in a way to maintain the active cavity temperature, T_1 , at a fixed level above the reference cavity temperature, T_3 . This is achieved by balancing the bridge output voltage ΔV in Eq. (2.11). As shown in Eq. (2.15), in steady-state, the bridge is balanced, so that T_1 and T_3 satisfy

$$T_1 = a + b T_3 \quad , \quad (2.30)$$

$$a = \frac{(a_1 + a_3)B_E - a_1}{b_1(1 - B_E)} \quad , \quad b = \frac{b_3 B_E}{b_1(1 - B_E)} \quad , \quad (2.31)$$

where a and b are constants which depend on the resistance versus temperature characteristics of the temperature sensing wires wound around the active and reference cavities.

On the other hand, the reference cavity temperature is given by

$$T_3 = T_2 + R_{32} \left(\sum_{k=1}^n D_{3k} \sigma T_k^4 + \frac{v_r^2}{R_r} + \dot{Q}_{J3} \right) \quad (2.32)$$

Substituting Eq. (2.32) and Eq. (2.30) into Eq. (2.29), we obtain

$$p = \frac{a + (b - 1)T_2}{R_{12}} - \sum_{k=1}^n \left(D_{1k} - b \frac{R_{32}}{R_{12}} D_{3k} \right) \sigma T_k^4 - \frac{v^2}{R_a} + b \frac{R_{32}}{R_{12}} \frac{v_r^2}{R_r} - \left(\dot{Q}_{J1} - b \frac{R_{32}}{R_{12}} \dot{Q}_{J3} \right) . \quad (2.33)$$

Thus, Eq. (2.33) and Eq. (2.9) provide a nonlinear steady-state description of the Total channels. In this model, the independent variables other than the incoming radiance are the Cu heatsink temperature, T_2 , the reference cavity heater voltage, v_r , and the box beam temperature, T_B , which is conductively coupled to the baseplate. It should be noted that the thermal resistances R_{12} and R_{32} are nearly equal, and that b is close to unity. This thermal and electrical balancing has a tendency to reduce the effect of many terms in Eq. (2.33) by reducing many of the coefficients. However, exact cancellations do not occur since the balance is not perfect. The cancellation tendency is nevertheless beneficial, as the sensitivity to some parameters is reduced.

The temperatures of the copper heatsink, T_2 , the field-of-view limiter, T_6 , the primary aperture, T_8 , and the reference cavity heater voltage, v_r , are measured and telemetered to Earth along with housekeeping data and the main radiometric output voltage, v . The remaining temperatures are not measured, but can be estimated. Due to the close conductive and radiative coupling of these nodes to the Cu heatsink whose temperature is tightly controlled, the temperatures of the aluminum heatsinks, and the reference and active cavities are assumed to be constant when the Cu heatsink temperature is constant. Note that the temperatures need not be, and in fact are not, equal; they simply are assumed to remain constant at their respective values. On the other hand, the baseplate temperature is only assumed to maintain a constant temperature of the field-of-view limiter. It should be noted that, due to the geometry and surface finish, the amount of radiation emitted from the baseplate which enters the cavity through the primary aperture is extremely small, as explained in the previous section.

In order to simplify the expression in Eq. (2.33) and to obtain a simpler algorithm

with which to interpret the sensor output using only the available, or measured, data, some terms can be grouped together. First, recall the identity

$$T_k^4 = T_{ko}^4 + 4 T_{ko}^3 (T_k - T_{ko}) + 6 T_{ko}^2 (T_k - T_{ko})^2 + 4 T_{ko} (T_k - T_{ko})^3 + (T_k - T_{ko})^4 \quad (2.34)$$

$$\cong T_{ko}^4 + 4 T_{ko}^3 \Delta T_k \quad |\Delta T_k / T_k| \ll 1 \quad , \quad (2.35)$$

where T_{ko} is the nominal node temperature and ΔT_k is the change in the temperature, T_k . For a peak-to-peak temperature variation of 4 °K, and a nominal node temperature of 300 °K, if the linear term in ΔT_k is about 2 W/m², the error that may be introduced by this approximation is nearly 0.02 W/m² which is well within the noise of the sensors.

$$p = -\frac{v^2}{R_a} - \sum_{k=1}^n d_k \Delta T_k + b \frac{R_{32}}{R_{12}} \frac{v_r^2}{R_r} + \left[\frac{a + (b-1)T_2}{R_{12}} - \sum_{k=1}^n \left(D_{1k} - b \frac{R_{32}}{R_{12}} D_{3k} \right) \sigma T_{ko}^4 - \left(\dot{Q}_{J1} - b \frac{R_{32}}{R_{12}} \dot{Q}_{J3} \right) \right] \quad (2.36.a)$$

$$d_k = 4\sigma \left(D_{1k} - b \frac{R_{32}}{R_{12}} D_{3k} \right) T_{ko}^3 \quad , \quad 1 \leq k \leq n \quad . \quad (2.36.b)$$

If all the node temperatures, hence ΔT_k , were known precisely, then these values could be used in Eq. (2.36.a) or Eq. (2.33) to compute the absorbed power. However, since only some of these temperatures are measured, it is necessary to estimate the remaining node temperatures. Since the heatsink temperature, T_2 , is tightly controlled about its set temperature, and due to the high conductive coupling of the detector nodes, it will be assumed that the only temperatures directly influenced by the incoming radiation are

the FOVL and the baseplate. The FOVL and baseplate are structurally attached to, but thermally insulated from the detector, and are conductively coupled to the instrument boxbeam which tempers any variations caused by the absorption of incoming radiation. Although thermally insulated, some minimal conductive coupling between the detector and the baseplate may be present and will be accommodated.

First consider the change in the node temperatures, ΔT_k , due to a change in the reference heater voltage from zero to v_o volts. From Eq. (2.32), it can be seen that

$$\Delta T_3 \cong R_{32} \left(\sum_{k=1}^n 4\sigma D_{3k} T_{k0}^3 \Delta T_k + \frac{v_r^2}{R_r} + \Delta Q_{J3} \right) . \quad (2.37)$$

In this mode, the active cavity heater will increase the active cavity temperature until the bridge is balanced; from Eq. (2.31), it follows that

$$\Delta T_1 = b \Delta T_3 , \quad (2.38)$$

where b is given by Eq. (2.31). Neglecting any temperature changes in the other detector nodes, and solving for ΔT_3 ,

$$\Delta T_3 = \frac{R_{32} \left(\frac{v_r^2}{R_r} + \Delta Q_{J3} \right)}{1 - 4\sigma R_{32} (D_{33} T_{30}^3 + b D_{31} T_{10}^3)} = . \quad (2.39)$$

Now let T_F and ΔT_F be the FOVL temperature and the change from the nominal FOVL temperature, respectively; let ΔT_k represent the total change in the k^{th} node temperature from the nominal, and

$$\Delta T_k = f_k \Delta T_F + g_k v_r^2 + e_k , \quad 1 \leq k \leq n , \quad (2.40)$$

where f_k accounts for any correlation between ΔT_k and ΔT_F due to conductive or radiation interactions, g_k accounts for changes in T_k due to v_r when T_2 is constant, and e_k represents the sensor noise and effects not explicitly modeled here, such as $\Delta \dot{Q}_{J3}$. Since most of the

node temperatures are constant, f_k and e_k are negligible for most nodes. Substituting Eq. (2.37) into Eq. (2.36),

$$p = -\frac{1}{R_a}v^2 + c_F T_F + c_r v_r^2 + c_o + e \quad , \quad (2.41)$$

$$c_F = -\sum_{k=1}^n d_k f_k \quad , \quad c_r = \frac{b}{R_r} \frac{R_{32}}{R_{12}} - \sum_{k=1}^n d_k g_k \quad (2.42)$$

$$e = -\sum_{k=1}^n d_k e_k \quad (2.43)$$

$$c_o = \frac{a + (b-1)T_2}{R_{12}} - \sum_{k=1}^n \left(D_{1k} - b \frac{R_{32}}{R_{12}} D_{3k} \right) \sigma T_{k_o}^4 - c_F T_{F_o} - \left(Q_{J1} - b \frac{R_{32}}{R_{12}} Q_{J3} \right) \quad . \quad (2.44)$$

Eq. (2.41), coupled with Eq. (2.9), provide a simple steady-state model, where the coefficients c_F , c_r and c_o are given by Eqs. (2.42), (2.43) and (2.44). With some exceptions, this model still maintains most of the significant relationships among the various system parameters.

From the expression for c_o in Eq. (2.44), it can be shown that, when the Cu heatsink temperature, T_r , is constant, c_o will remain constant. Since the nominal temperatures are constant by definition, it remains to show that the Joule heating term arising from the current flowing in the temperature sensitive sensor wires wound around the active and reference cavities is also constant. From the bridge model obtained in the preceding section in Eq. (2.11), it is seen that in steady-state the bridge will be balanced at

$$R_1(T_1) = \frac{B_E}{1 - B_E} R_3(T_3) \quad . \quad (2.45)$$

After some manipulation, it can be shown that the Joule heating produced by the bridge can be expressed as

$$\dot{Q}_{J1}(V_B B_E)4^2 \frac{1}{R_1} = [V_B(1 - B_E)]^2 \left(\frac{B_E}{1 - B_E} \right) \frac{1}{R_3} , \quad (2.46)$$

$$\dot{Q}_{J3} = [V_B(1 - B_E)]^2 \frac{1}{R_3} , \quad (2.47)$$

$$\dot{Q}_{J1} - b \frac{R_{32}}{R_{12}} \dot{Q}_{J3} = V_B^2(1 - B_E)B_E \left[1 - \left(\frac{b_3}{b_1} \right) \left(\frac{R_{32}}{R_{12}} \right) \right] \frac{1}{R_3} , \quad (2.48)$$

where the arguments of R_1 and R_3 have been dropped for convenience.

The beneficial effects of thermal and electrical balancing can clearly be seen in Eq. (2.48). Perfect balance would imply $b_1 = b_3$, and $R_{32} = R_{12}$, which would result in the complete cancellation of this term. Although perfect balancing is not likely, the term in brackets on the RHS of Eq. (2.48) becomes quite small, so that the effect of the term is considerably smaller than otherwise. Furthermore, the sensitivity of the term to variations in R_3 is also of second order, as this term would be of order $\sigma((1/R_3)^2)$. As R_3 is near 2200 Ω , the change in the Joule heating term due to a 1 Ω change in R_3 would be less than an easily negligible 0.05 %. The sensitivity of the term to expected variations in B_E , b_1 and b_3 are also small, although not always negligible.

The major sensitivity of c_o is to variations in the bridge resistances and to variations in the boxbeam and satellite temperatures. The former effect is clearly seen from Eq. (2.48) and Eq. (2.31) where an extremely small variation in B_E , a_1 , a_3 , b_1 or b_3 can produce a noticeable change in c_o . The latter effect is due to the fact that ambient satellite temperature may, in steady-state, produce thermal gradients in the aluminum heatsink, node 7, near the reference cavity. This may then change the reference cavity temperature by an extremely small amount, which then results in a similar change in the active cavity temperature. Even though the temperature variation in either cavity temperature may be small, the high sensitivity of the sensor to such changes requires careful consideration. For example, a change of 0.001° C in the active cavity may be interpreted as a change

of about 3 W/m^2 in the incoming flux. Similarly, a change of 0.01Ω in the resistance of any of the bridge components may be interpreted as a change of 8 W/m^2 in the incoming flux. To minimize such changes, the temperature sensing wires of the ERBE sensor were painstakingly processed using a heating treatment, and the heatsink temperature was tightly controlled about its set value.

Equation (2.9) and Eqs. (2.41) - (2.44) provide a steady-state model which describes the sensor behavior under the assumptions stated. It should be noted that a variety of measurement conditions can be obtained by appropriate treatment of Eq. (2.9) to obtain the incoming flux. This will be done in the following sections for the Earth-looking modes, as well as for the measurement conditions encountered in ground and flight calibrations.

2.4.3 Shortwave Channels.

The only significant difference between the Shortwave and Total sensors is the presence of the dome filter in the former sensors which filters out longwave radiation. Otherwise the sensors are designed to operate in the same way. Thus, most of the steady-state model development for the Total sensors is also valid for the Shortwave sensors, when the number of nodes, n , is replaced by the number of Shortwave sensor nodes, m , which simply includes the filter dome as an additional node. Since the interactions among the detector nodes and the electronics are the same, Eqs. (2.29) - (2.39) continue to hold.

Now, if all the node temperatures, including the dome filter temperature, were precisely known, the power absorbed by the cavity could be computed using Eq. (2.33) or Eq. (2.36.a). Whereas measuring the dome temperature for use in the interpretation of the sensor response would be desirable, the placement of a temperature sensor in the dome filter would modify the uniformity of the filter as well as add to the manufacturing challenge. Thus, it is necessary to estimate the dome temperature.

From Fig. 2.2, it can be seen that the only nodes directly influenced by incoming radiation are the FOVL, the baseplate, the dome filter and the primary aperture, excluding the active cavity whose temperature is controlled. The steady-state change in the dome

temperature due to incoming radiation can be obtained by manipulating Eq. (2.25).

$$\Delta T_9 \cong \frac{1}{\frac{R_{98} + R_{94}}{R_{98}R_{98}} - 4\sigma D_{99}T_{90}^3} \left[\left(\frac{1}{R_{98}} + 4\sigma D_{98}T_{80}^3 \right) \Delta T_A + 4\sigma \left(D_{95}T_{50}^3 + D_{96}T_{60}^3 \right) \Delta T_F + p_f \right] \quad (2.49.a)$$

$$= h_F \Delta T_F + h_A \Delta T_A + h_f p_f \quad , \quad (2.49.b)$$

where it has been assumed that only the change in the FOVL and the baseplate are the same in steady-state, and that the nodes which do not directly see the incoming radiation remain unchanged.

The effect of the reference cavity heater voltage, v_r , on the dome filter temperature is only seen through the change in the emitted radiation from the active cavity. As for the Total channels, the change in the cavity temperatures due to the reference cavity heater voltage can be seen to be directly proportional to the added heat, hence to v_r^2 , by combining Eq. (2.38) and Eq. (2.39).

The total change in the node temperatures can be expressed in the form

$$\Delta T_k = h_{Fk} \Delta T_F + h_{Ak} \Delta T_A + h_{rk} v_r^2 + h_{fk} p_f + e_k \quad , \quad (2.50)$$

where e_k represents sensor noise and effects which are not explicitly modeled shown in Eq. (2.50). It should be noted that while this expression allows a linear relationship between the power absorbed by the filter, p_f , and all the node temperatures for generality, in fact h_{fk} ought to vanish except for $k = 9$; i.e., the dome filter itself. Similar comments apply to the other coefficients.

Substituting Eq. (2.50) into Eq. (2.36.a),

$$p + c_f p_f = -\frac{1}{R_a} v^2 + c_F T_F + c_A T_A + c_r v_r^2 + c_o + e \quad , \quad (2.51)$$

$$c_F = - \sum_{k=1}^m d_k h_{Fk} \quad , \quad c_A = \sum_{k=1}^m d_k h_{Ak} \quad , \quad (2.52)$$

$$c_r = \frac{b}{R_r} \frac{R_{32}}{R_{12}} - \sum_{k=1}^m d_k h_{rk} \quad , \quad e = - \sum_{k=1}^m d_k e_k \quad , \quad (2.53)$$

$$c_o = \frac{a + (b-1)T_2}{R_{12}} - \sum_{k=1}^m \left(D_{1k} - b \frac{R_{32}}{R_{12}} D_{3k} \right) \sigma T_{ko}^4 - c_F T_{Fo} \\ - \left(\dot{Q}_{J1} - b \frac{R_{32}}{R_{12}} \dot{Q}_{J3} \right) \quad (2.54)$$

$$c_f = + \sum_{k=1}^m d_k h_{fk} \quad (2.55)$$

where T_{Fo} is the nominal FOVL temperature and the Joule heating terms \dot{Q}_{J1} and \dot{Q}_{J3} are given by Eq. (2.46) and Eq. (2.47), respectively.

From Eq. (2.51), it is seen that the form of the steady-state model for the Shortwave and Total channels is essentially the same, when the LHS is interpreted as the power absorbed by the active cavity, including the extra power emitted by the dome filter into the cavity. It should be noted, however, that the values of the coefficients c_F , c_r and c_o are different for the two sensors.

Since the power emitted by the FOVL and baseplate is largely longwave radiation which is filtered by the dome, the active cavity does not receive this radiation directly. However, the indirect effect of increased dome filter emission will be felt by the active cavity. As this is a very small effect, the dominating tendency is not clearly determined.

The steady-state model for the Shortwave channels can thus be expressed in the form of Eqs. (2.51) - (2.55), Eq. (2.24) and Eq. (2.26). At this stage, the model is sufficiently general to accommodate the type of measurement conditions which will be normally encountered during the Earth-looking mode as well as the ground and flight calibration conditions.

2.5 Sensor Data Output Interpretation Algorithm

Using the steady-state models developed, simple algorithms which can be used to interpret the operational data during the normal Earth-looking modes are obtained in this section. The specialization of the models to the ground and flight calibration conditions will be performed in the following sections.

The steady-state models developed can be used to obtain power absorbed by the active cavity. However, the desired quantity is the flux originating within the sensor's field-of-view and spectral band, as given in Eq. (2.1) and Eq. (2.2). The desired fluxes can be estimated from the absorbed power using standard approximations.

2.5.1 Total Wavelength Channels.

For the Total channels, the power absorbed by the active cavity is given by Eq. (2.9). Let $\Omega_{iE}(x, y)$ be the solid angle subtended by the portion of the top of the atmosphere seen through the secondary aperture at the point (x, y) on the primary aperture opening. Note that

$$\Omega_{ME}(x, y) = \Omega_M(x, y) \quad , \quad \Omega_{WE}(x, y) \cong \Omega_E \quad . \quad (2.56)$$

This is due to the fact that, for the MFOV channels, the Earth (or the TOA) fills the sensor's field-of-view completely; whereas the WFOV channels include a space ring beyond the TOA so that all of the TOA can be seen through the secondary aperture at every point of the primary aperture opening. Therefore, in the Earth-looking modes, the WFOV sensors' fields-of-view are not completely filled with the TOA, as no significant signal is contributed by the solid angle formed by the space ring, under normal conditions, i. e., where the sun or the moon is not in the space ring.

The power absorbed by the active cavity can now be approximated as

$$p_{iT} = \bar{\alpha}_{iT} A_{iT} \left(\frac{G_{iE}}{F_{iE}} \right) \hat{E}_{iT} \quad , \quad i = M, W \quad (2.57)$$

where $\bar{\alpha}_{iT}$ is the effective absorptivity of the active cavity, F_{iE} the standard configuration factor from the primary aperture opening to the portion of the TOA “seen”, G_{iE} an angular response factor and \hat{E}_{iT} the estimate of the radiant incidence, or flux, arriving from the TOA within the appropriate field-of-view.

$$F_{iE} = \frac{1}{\pi A_{iT}} \iint_{A_{iT}} \iint_{\Omega_{iE}(x,y)} 1 d\Omega dA \quad , \quad i = M, W \quad (2.58)$$

$$G_{iE} = \frac{1}{\pi A_{iT}} \iint_{A_{iT}} \iint_{\Omega_{iE}(x,y)} g_{iT}(\psi, \chi) d\Omega dA \quad , \quad i = M, W \quad (2.59)$$

It should be noted that the angular response factor, G_{iE} , tries to account for a sensor response which is different than the standard cosine response using a single factor. When the sensor has a perfect cosine response, so that $g_{iT}(\psi, \chi)$ is unity for all directions (ψ, χ) of interest, G_{iE} reduces to the standard geometric configuration factor, and the term in parenthesis in Eq. (2.57) reduces to unity; i.e.,

$$p_{iT} = \bar{\alpha}_{iT} A_{iT} \hat{E}_{iT} \quad . \quad (2.60)$$

when the sensor has small deviations in angular response, the average effect of these deviations can be accounted for by this angular response factor. When large deviations are present, it is necessary to include the angular response into the process of inverting the flux from satellite altitude to the TOA. The flux estimate obtained here is given by

$$\begin{aligned} \hat{E}_{iT} &= \frac{1}{A_{iT} \bar{\alpha}_{iT}} \left(\frac{F_{iE}}{G_{iE}} \right) \iint_{A_{iT}} \iint_{\Omega_{iE}(x,y)} \int_0^\infty L_{E\lambda}(x, y; \psi, \chi) \alpha_{iT}(\lambda) g_{iT}(\psi, \chi) d\lambda d\Omega dA \\ &\cong \frac{1}{A_{iT}} \iint_{A_{iT}} \left[\iint_{\Omega_{iE}(x,y)} L_E(x, y; \psi, \chi) d\Omega \right] dA \quad , \quad i = M, W \end{aligned} \quad (2.61)$$

Combining the steady-state sensor model in Eq. (2.41) with Eq. (2.57), and solving for the estimated flux, we obtain a simple algorithm of the form

$$\hat{E}_T = A_v v^2 + A_F T_F + A_r v_r^2 + B \quad , \quad (2.62)$$

$$A_v = \frac{1}{AR_a \bar{\alpha}} \left(\frac{F_E}{G_E} \right) \quad , \quad A_F = \frac{c_F}{A \bar{\alpha}} \left(\frac{F_E}{G_E} \right) \quad , \quad (2.63)$$

$$A_r = \frac{c_r}{A \bar{\alpha}} \left(\frac{F_E}{G_E} \right) \quad , \quad B = \frac{c_o}{A \bar{\alpha}} \left(\frac{F_E}{G_E} \right) \quad , \quad (2.64)$$

where the subscripts denoting the channel are not explicitly shown, for convenience.

With this simple algorithm, it is possible to estimate the desired flux when the coefficients A_v , A_F , A_r and B are determined. While the expressions given for the coefficients provide an understanding of the trends and relationships among the system parameter, they are not intended for use in determining the actual values of these coefficients.

The determination of the actual coefficient values for each sensor is described in the following section on ground calibration. In this context, calibration is the process of determining the values of the algorithm coefficients needed to interpret the digital sensor output by using measurements obtained by each sensor under well-controlled calibration conditions and well-established calibration sources traceable to accepted standards.

2.5.2 Shortwave Channels.

For the Shortwave channels, the power absorbed by the active cavity due to the incoming radiation can be obtained similarly as

$$E_S = A_V V^2 + A_F T_F + A_R V_R^2 + B + A_E E_T \quad (2.65)$$

where $A_E E_T$ is due to the longwave dome heating effects.

3. GROUND CALIBRATION

This chapter describes the ground calibration sources, procedures and analysis for determining the count conversation coefficients for total and shortwave nonscanner sensors. Further, the results are tabulated for each sensor.

3.1 Description of Calibration Sources

Figure 3.1 shows the ERBE calibration chamber, which is an 8 foot diameter cylinder containing a Master Reference Blackbody (MRBB) at one end and an Integrating Sphere (IS) on the other end. The Solar Simulator can project a beam through a quartz window onto an instrument mounted on a carousel in the middle of the chamber. The chamber walls, chilled with liquid nitrogen (LN_2), are used as a Space Reference Source for scanner calibration.

3.1.1 Master Reference Blackbody (MRBB).

The ERBE Master Reference Blackbody (MRBB), shown in Fig. 3.2, is traceable to the IPTS68. The radiating surface is a concentrically grooved piece of aluminum with a black anodized face. Six calibrated platinum resistance thermometers (PRTs) are mounted on the back of the groove to determine its temperature. The temperature stability is attained by placing the aluminum in a thermally controlled housing. The instrument Fields-Of-view are completely filled by the blackbody. To simulate the energy exchange to space that occurs during flight operation of the instruments, the instrument is placed at the narrow end of the cone where a grooved ring is cooled by the liquid nitrogen.

The absorptivity of the grooved surface, measured at the Naval Ocean Systems Center, is found to be 0.991. The grooved surface temperature variations measured by an infrared radiometer appear to be less than ± 0.01 K over the operating range of the MRBB (-80°C to 75°C). The thermal control is accurate to ± 0.01 K over this temperature range.

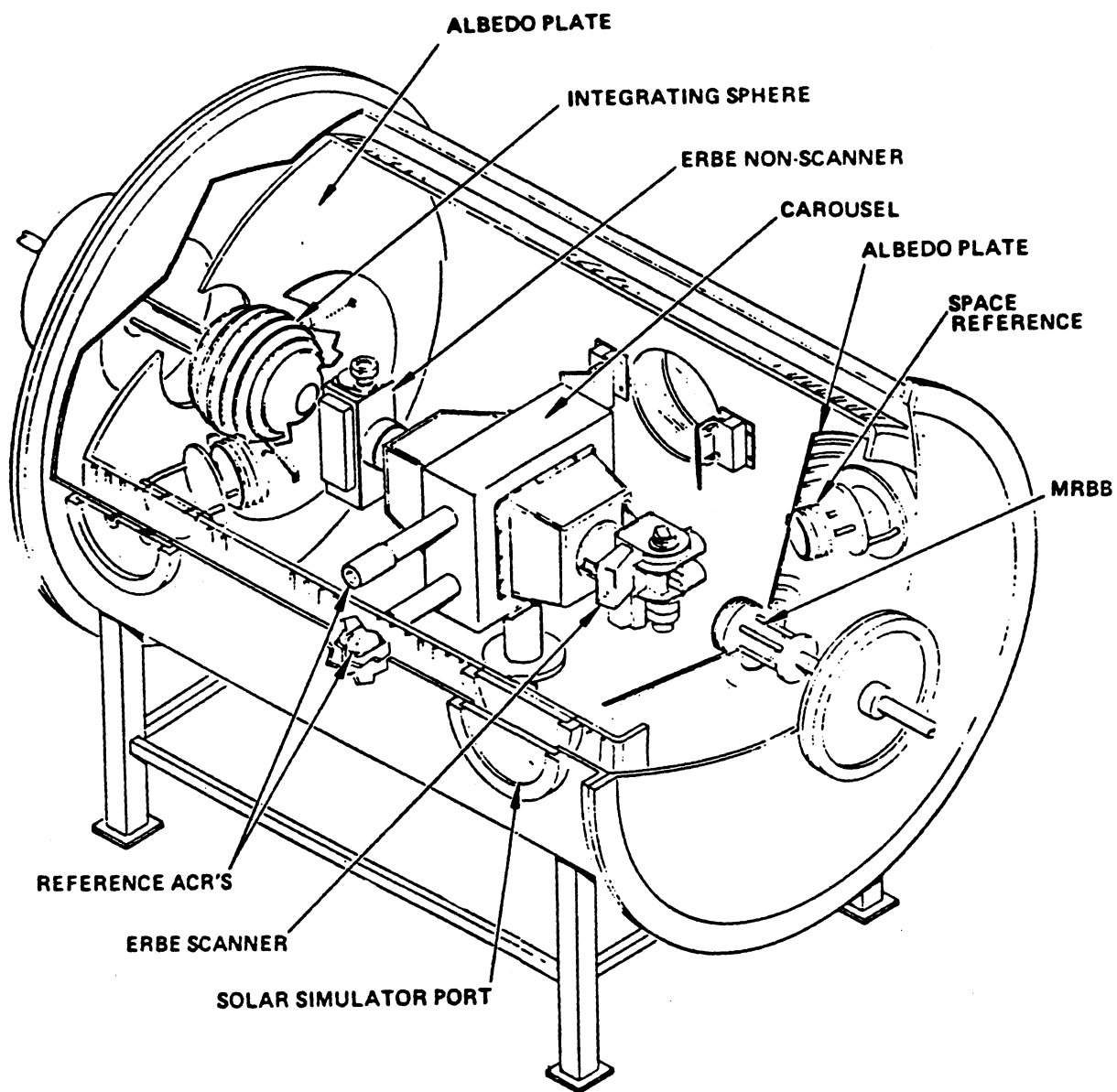


Figure 3.1 ERBE Calibration Chamber

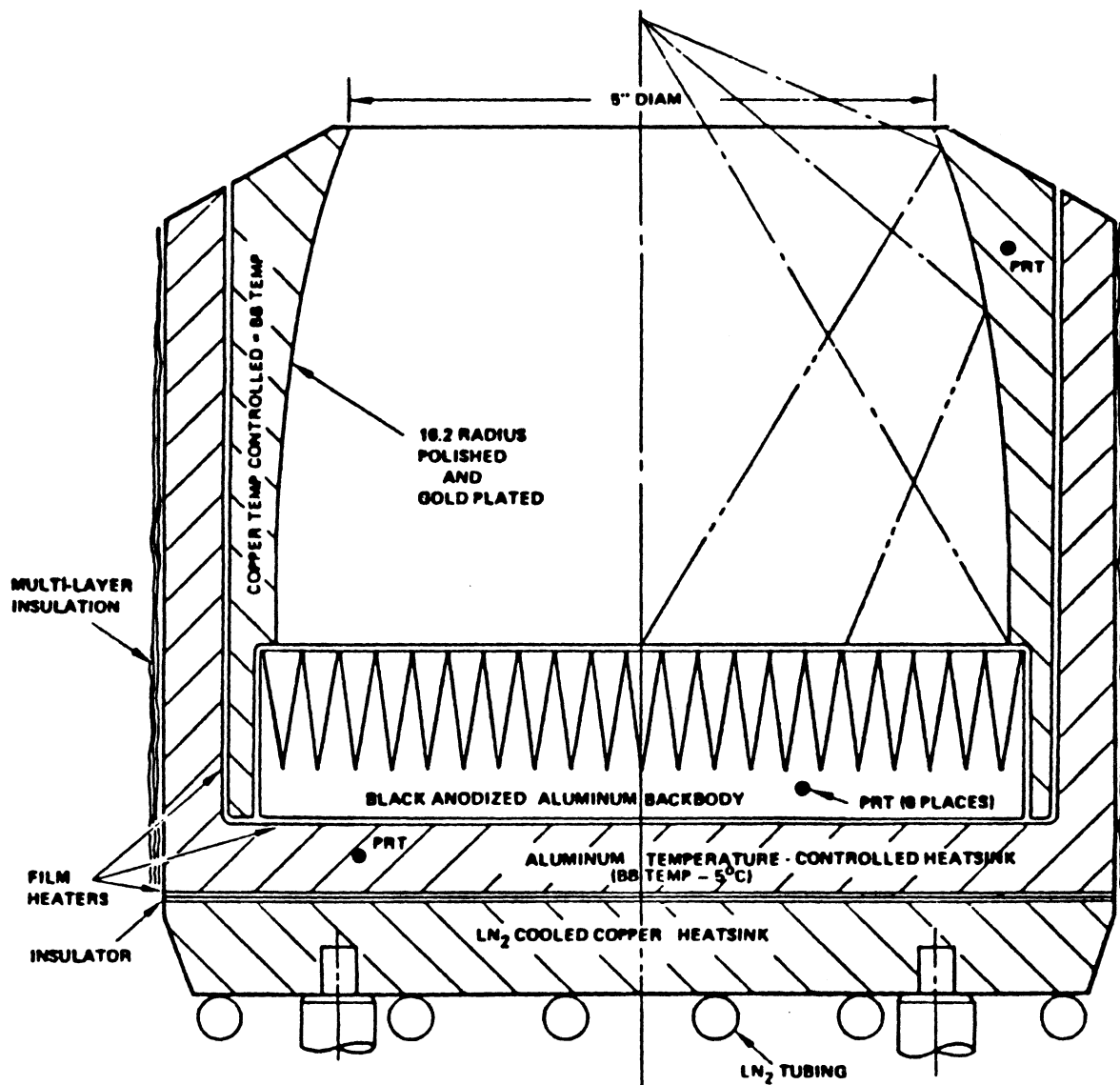


Figure 3.2 Cross section of Master Reference Blackbody (MRBB)

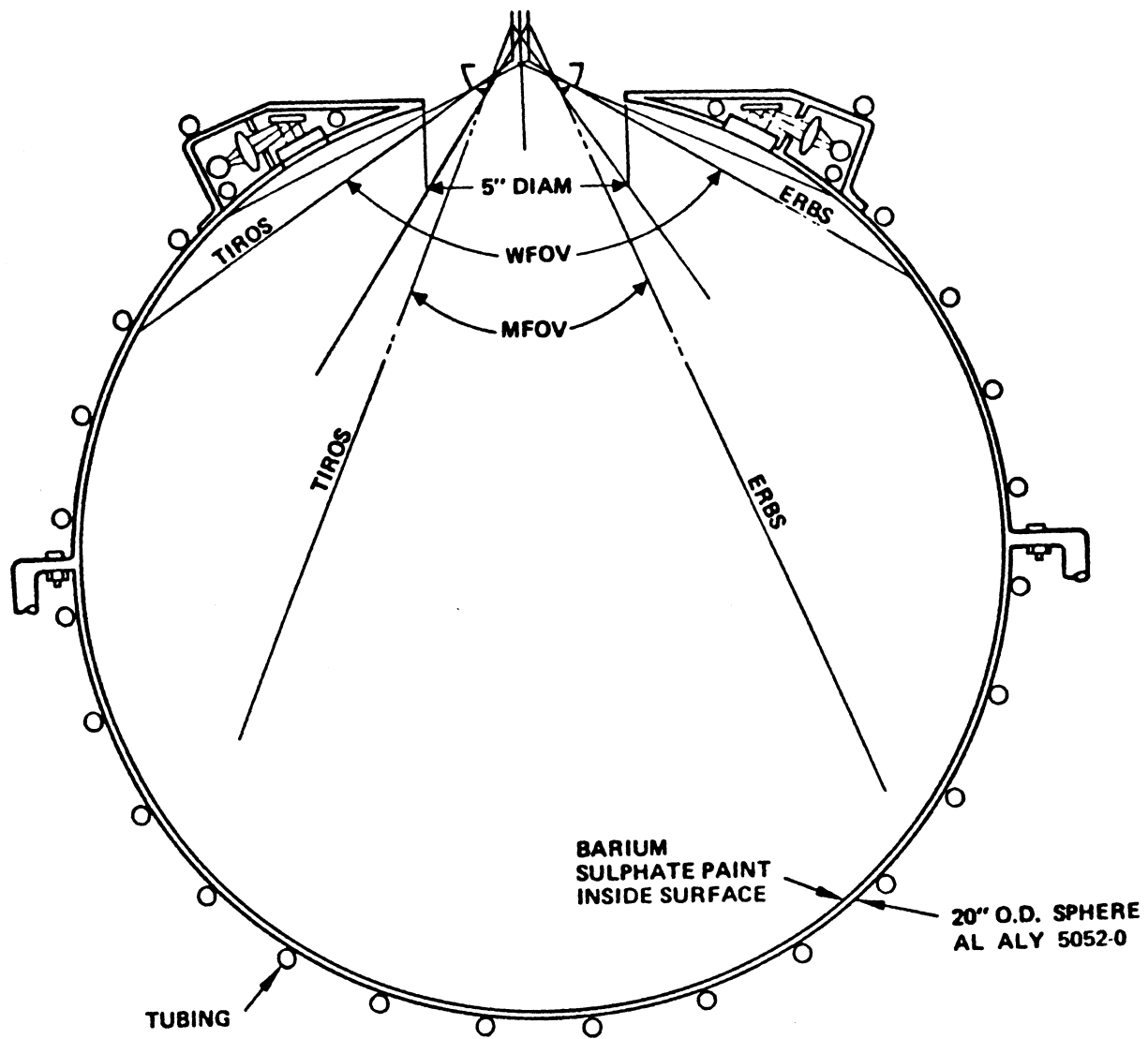


Figure 3.3 Integrating Sphere

3.1.2 Integrating Sphere (IS).

The Integrating Sphere, shown in Fig. 3.3, is used to calibrate the nonscanner short-wave sensors. The 20 inch diameter sphere is illuminated by four 250 watts tungsten lamps through projection optics system that reflects the light off a mirror and then transmits through a piece of flashed opal glass to the interior of the sphere.

The inside wall of the Integrating Sphere is coated first by 3M White Velvet and then by barium sulfate. A uniform angular radiance for the Sphere's interior coat is found within a few percent. Further, the silicon photodiode (SiPD) is used to measure the shortwave radiation. The Integrating Sphere is also maintained thermally stable by circulating water and alcohol in a pipe wound around its outside.

3.2 Count Conversion Equations

Following the development of sensor modeling detailed in Chapter II, one can rewrite the Count Conversion Equation for Total Channel as

$$E_T = A'_V V^2 + A'_F (T_F - \bar{T}_{Fo}) + A'_H T_H + A'_A T_A + A'_R V_R^2 + B'_{ICS} \quad (3.1)$$

where $E_T = \epsilon \sigma T^4$, V , T_F , \bar{T}_{Fo} , T_H , T_A and V_R are known variables. Here the emissivity, ϵ , is considered to be one. Sigma, σ , is the Stefan-Boltzmann constant. T is the source temperature. The unknown ground coefficients like A'_V , A'_F , A'_R , A'_H , A'_A and B'_{ICS} are determined by performing the multi-regression analysis. Note that the contributions of primary aperture and heat sink are found negligible due to a very small temperature variations. Therefore, the terms $A'_H T_H$ and $A'_A T_A$ are dropped from the above equation. Thus, Eq. (3.1) reduces to

$$E_T = A'_V V^2 + A'_F (T_F - \bar{T}_{Fo}) + A'_R V_R^2 + B'_{ICS} \quad (3.2)$$

Similarly, the Count Conversion Equation for Shortwave Channel can be rewritten from Eq. (2.65) as

$$E_S = A'_V V^2 + A'_F (T_F - \bar{T}_{Fo}) + A'_R V_R^2 + B'_{ICS} + (A'_E E_T) \quad (3.3)$$

This equation is very similar to the above Eq. (3.2), except for a last term, $A'_E E_T$, which is due to the longwave dome heating effects. The unknown coefficients are determined again by performing multi-regression analysis. Silicon Photodiode (SiPD) is calibrated using the procedure outlined in [10].

3.3 Calibration Data Background

Calibration data for total and shortwave sensors were obtained by looking at the Master Reference Blackbody (MRBB) and Integrating Sphere (IS) sources described in the previous section. Internal Blackbody (IBB) sources are used to monitor the changes in the nonscanner sensors during In-Flight operation. Therefore IBB ground data is used as a transfer standard for total channels from MRBB to IBB. This section describes the important features of the data selected for determining the ground Count Conversion Coefficients.

3.3.1 ERBS Calibration Data.

Details about the calibration data sets are given in [5]. It is important to note that the calibration testing was interrupted by power outages and a failure in the elevation drive. As a result, there are three types of data sets available: (1) Pre-recovery, (2) Recovery and (3) Restart. Each data set is analyzed in this study.

3.3.2 NOAA-9 Calibration Data.

There are two types of data sets available. One is available in the preliminary calibration report and the other is documented in the final calibration report [6]. Note that the heat sink temperature reported in the preliminary report is 38.8°C which is different from the final calibration report, 33.58°C. The Integrating Sphere (IS) data for Medium Field-of-View Total (MFOVT) Channel, which is needed to calibrate the Silicon Photodiode (SiPD) is not available.

3.3.3 NOAA-10 Calibration Data.

There are two calibration data sets: one is documented in [7] and the other is available in loose form. The important point to be mentioned is that the WFOVT channel calibrated in May 1983 was replaced by a new WFOVT channel calibrated in May 1984. After a thorough analysis, the following conclusions are drawn:

- (1) Total channels should be calibrated using May 1984 data sets because of the availability of May 1984 IBB data. Note that May 1983 IBB data is not reported.
- (2) Shortwave channels are calibrated using May 1983 data sets. Silicon Photodiode (SiPD) was calibrated by Total channels count conversion coefficients determined from May 1983 data sets. Note that the May 1984 Integrating Sphere (IS) data for Total channels is not reported.

3.4 Ground Count Conversion Coefficients Results

Count Conversion Coefficients for total and shortwave channels were obtained by using multi-regression analysis. Table 3.1 displays the ERBS Nonscanner ground count conversion coefficients with the number of data points used in this analysis and standard deviation of error in watt/m². Coefficients for total channels are computed using MRBB pre-recovery period data. Silicon Photodiodes (SiPD) are calibrated using IS data of total channels. Using SiPD's gain and ΔE_L given in Table 3.1, count conversion coefficients for Shortwave channels are obtained using MRBB and IS data (excluding $V_R = 6.77$ data). The Shortwave channel gains are recalibrated using solar calibration in orbit. Note that the A'_F term of MFOVSW is found to be positive which contradicts the theoretical value obtained neglecting conductive thermal transfer.

NOAA-9 Nonscanner ground count conversion coefficients are given in Table 3.2. Count conversion coefficients for MFOVT and WFOVT channels are determined using MRBB data from final and preliminary calibration reports respectively. Numerous runs were also made with the available data and the coefficients found are not very different. As

Table 3.1 ERBS Flight Model One (FM1)
Ground Count Conversion Coefficients

SYMBOLS	MFOVT	WFOVT	MFOVSW	WFOVSW
A'_V	-53.5596	-26.2164	-58.454	-28.2194
A'_E			-0.03641	-0.02902
A'_F	-2.1768	-1.607	2.799	-0.7097
A'_R	59.2633	30.0461	66.4883	29.2817
B'_{ICS}	2487.64	1560.32	2984.17	1234.19
\bar{T}_{Fo}	292.4233	292.5614	293.6555	293.4491
SiPD (GAIN & OFFSET)			$g = 34.4596$ $\Delta E_L = 3.9127$	$g = 21.1822$ $\Delta E_L = 5.1004$
DATA POINTS	17	14	24	28
σ of ERROR (watt/m ²)	1.63	0.14	2.95	1.53

Table 3.2 NOAA-9 Flight Model Two (FM2)
Ground Count Conversion Coefficients

SYMBOLS	MFOVT	WFOVT	MFOVSW	WFOVSW
A'_V	-94.4978	-27.5846	-105.3788	-30.6239
A'_E			-0.03561	-0.03384
A'_F	-2.2093	-0.4799	-20.2739	-6.1145
A'_R	100.1814	29.8788	119.9772	35.506
B'_{ICS}	4559.82	1609.58	4822.18	1543.95
\bar{T}_{Fo}	292.7021	293.3871	293.4132	294.316
SiPD (GAIN & OFFSET)			$g = 24.0911^*$ $\Delta E_L = 3.8238$	$g = 22.3074$ $\Delta E_L = 2.8823$
DATA POINTS	17	24	25	40
σ of ERROR (watt/m ²)	3.85	0.88	7.27	4.47

* Due to the unavailability of MFOVT data for the integrating sphere, the MFOVSW channel SiPD gain and offset were not obtained by the established procedure. Details are given in the text.

we know that the calibration of Shortwave channels require the behavior of SiPD, which is gain (g) and offset (ΔE_L). For MFOVSW channel, the behavior of SiPD is not known due to the unavailability of IS data for MFOVT channel. To resolve this problem, the SiPD gains of all Shortwave sensors were compared and found that the SiPD's gain of NOAA-9 WFOVSW was greater by 5.3% than the SiPD gain of ERBS WFOVSW. With this conclusion, the SiPD gain for MFOVSW channel was computed as $g = 24.0911$, which is 5.3% higher than the ERBS MFOVSW SiPD gain. Thus the count conversion coefficients for MFOVSW was computed using MRBB and IS ground data. Further, note that the A_F term of MFOVSW is negative which is opposite to ERBS MFOVSW channel.

Table 3.3 describes NOAA-10 Nonscanner ground count conversion coefficient results. MFOVT channel is calibrated using May 1984 MRBB data (excluding $V_R = 6.77$ data). In addition, the count conversion coefficients for MFOVT channel using May 1983 MRBB data (excluding $V_R = 6.77$ data) are not found to be very different from the coefficients given in Table 3.3. Similarly, the count conversion coefficients for WFOVT channel is determined. Further, the count conversion coefficients for MFOVSW and WFOVSW channels are obtained using May 1983 MRBB and IS calibration data. Note that the A_F term for each channel is found to be negative, which is consistent with the NOAA-9 Nonscanner sensors.

Table 3.3 NOAA-10 Proto-Flight Model (PFM)

Ground Count Conversion Coefficients

SYMBOLS	MFOVT	WFOVT	MFOVSW	WFOVSW
A'_V	-97.2831	-27.1754	-103.2228	-27.6993
A'_E			-0.02232	-0.02859
A'_F	-8.3056	-0.5087	-13.9002	-1.4872
A'_R	93.8456	28.7406	120.1269	32.6115
B'_{ICS}	4544.25	1392.75	4307.47	1264.18
\bar{T}_{FO}	293.9253	294.1156	293.5307	293.72460
SiPD (GAIN & OFFSET)			$g = 34.4596$ $\Delta E_L = 3.9127$	$g = 32.2839^*$ $\Delta E_L = 4.3029$
DATA POINTS	17	18	15	41
σ of ERROR (watt/m ²)	1.56	0.61	4.59	2.67

* g and ΔE_L for WFOVSW channel were computed by using May 1983 IS data for WFOVT channel.

4. IN-FLIGHT CALIBRATION

This chapter describes the in-flight calibration sources, count conversion equations, calibration procedures and analysis for determining the final in-flight count conversion coefficients for total and shortwave sensors.

4.1 In-Flight Calibration Sources

Figure 4.1 shows the nonscanner elevation beam positions. The nonscanner sensors are mounted in the elevation beam, which can be rotated to observe the Earth, the sun, or the internal blackbodies. Thus, the in-flight calibrations for total channels are maintained through the use of internal blackbody sources and space-look data during solar calibration, while shortwave channels are calibrated using solar calibration data, space-look data, SWICS lamps-off, and SWICS lamps-on data. Further, the dark side of the Earth data can be used to determine the shortwave channels offsets.

4.2 In-Flight Count Conversion Equations

The development of in-flight count conversion equations for total and shortwave channels are given in this section.

4.2.1 Total Channels.

In-flight count conversion equations for total channels can be obtained by multiplying the ground count conversion equations with a configuration factor, f . Thus, the Eq. (3.1) becomes

$$E_T = A_V V^2 + A_F T_F + A_R V_R^2 + B_{EDMT} \quad (4.1)$$

where $E_T = f E'_T$, $A_V = f A'_V$, $A_F = f A'_F$, $A_R = f A'_R$, and $B_{EDMT} = f(B'_{ICS} - A'_F \bar{T}_{Fo})$. The configuration factor, f , for each sensor is given in Appendix A. Note that A_V , A_F ,

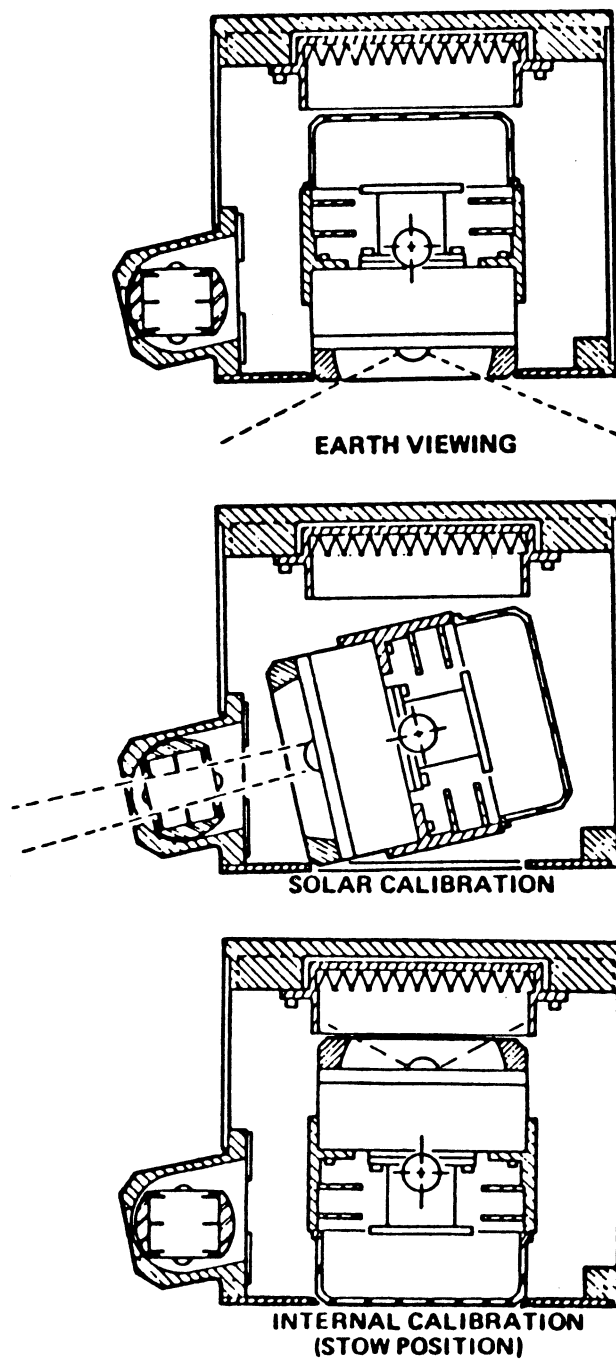


Figure 4.1 Nonscanner Elevation Positions

A_R and B_{EDMT} are known coefficients determined from the ground MRBB calibration data. These coefficients would remain unchanged except the offset term, B_{EDMT} , which would be determined by utilizing in-flight calibration data. This will be discussed in the next section.

4.2.2 Shortwave Channels.

Similarly, the count conversion equations for the shortwave channels can be obtained by multiplying Eq. (3.3) by a configuration factor, f , as follows.

$$E_S = A_V V^2 + A_F T_F + A_R V_R^2 + A_E E_T + B_{EDMT} \quad (4.2)$$

where $A_V = fA'_V$, $A_F = fA'_F$, $A_R = fA'_R$ and $B_{EDMT} = f(B'_{ICS} - A'_F \bar{T}_{Fo})$. These coefficients are determined from the ground MRBB and IS data.

Due to the use of dome for preventing the longwave radiation from getting into the active cavity, the determination of count conversion coefficients for shortwave channels are not straight forward like it is for total channels. The dome's transmissivity is decreasing, which may be due to ultraviolet energy in the solar spectrum. As a result, both the gain and offset are varying with time during in-flight operations. Methods to determine the gain and offset are described in the next subsection.

4.2.3 Dome Degradation Factor.

Dome degradation factor (DF) is required to upgrade the in-flight count conversion coefficients, Eq. (4.2), determined directly from the ground calibration data. This factor, which can be computed from the solar measurements data, is defined as

$$DF = \frac{\tau(R)}{\tau(X)} = \frac{S(X)}{S(R)}$$

where X is a day in question and R is a reference day. $S(X)$ and $S(R)$ are computed from an equation fitted to solar measurements data. Note that the use of such equation would reduce sensor noise and error in the solar measurements. Further, a_1 , $(A_V/(1 - A_E))$

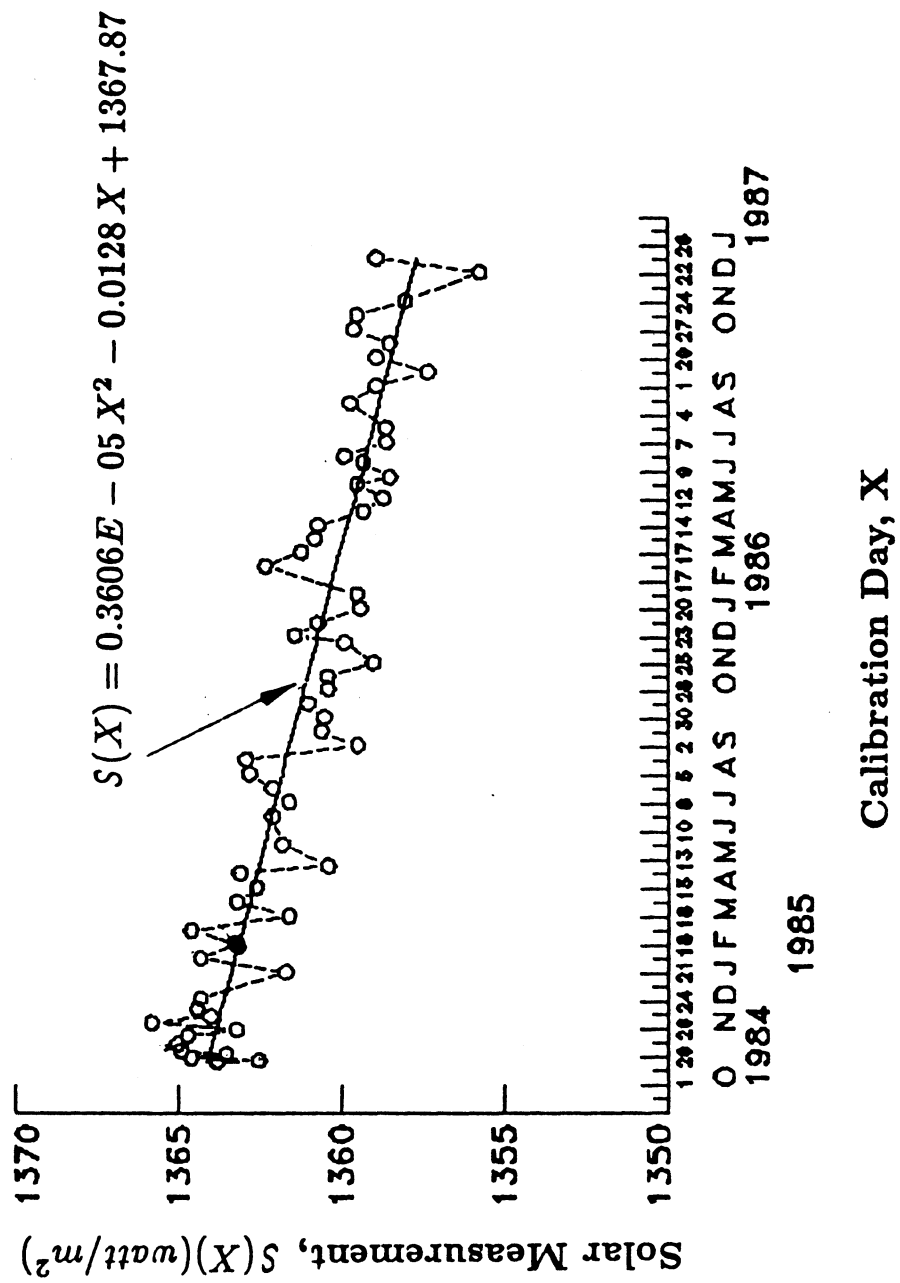


Figure 4.2 Solar Measurement vs Calibration Day
For ERBS MFOVSW Sensor

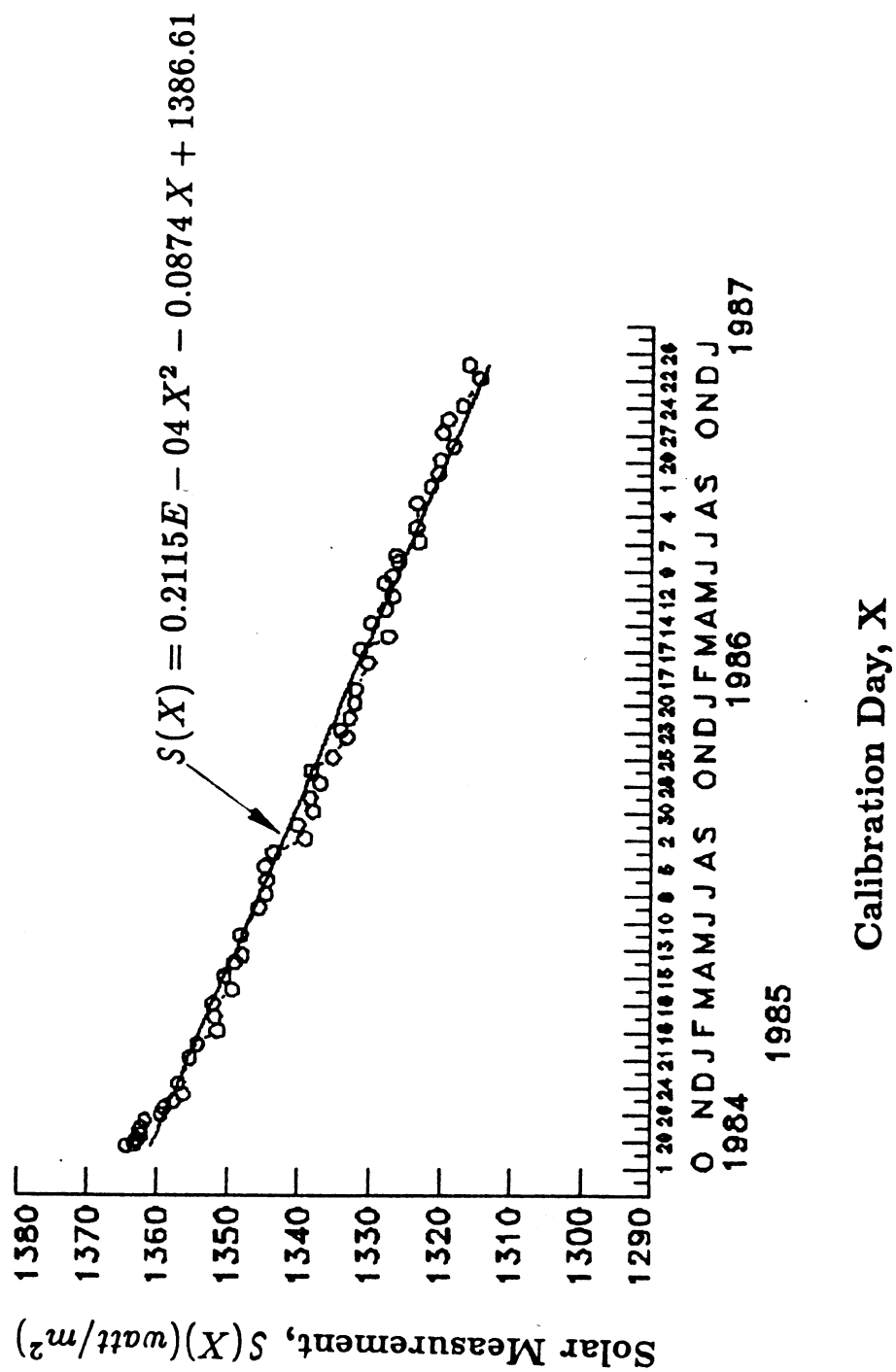


Figure 4.3 Solar Measurement vs Calibration Day
For ERBS WFOVSW Sensor

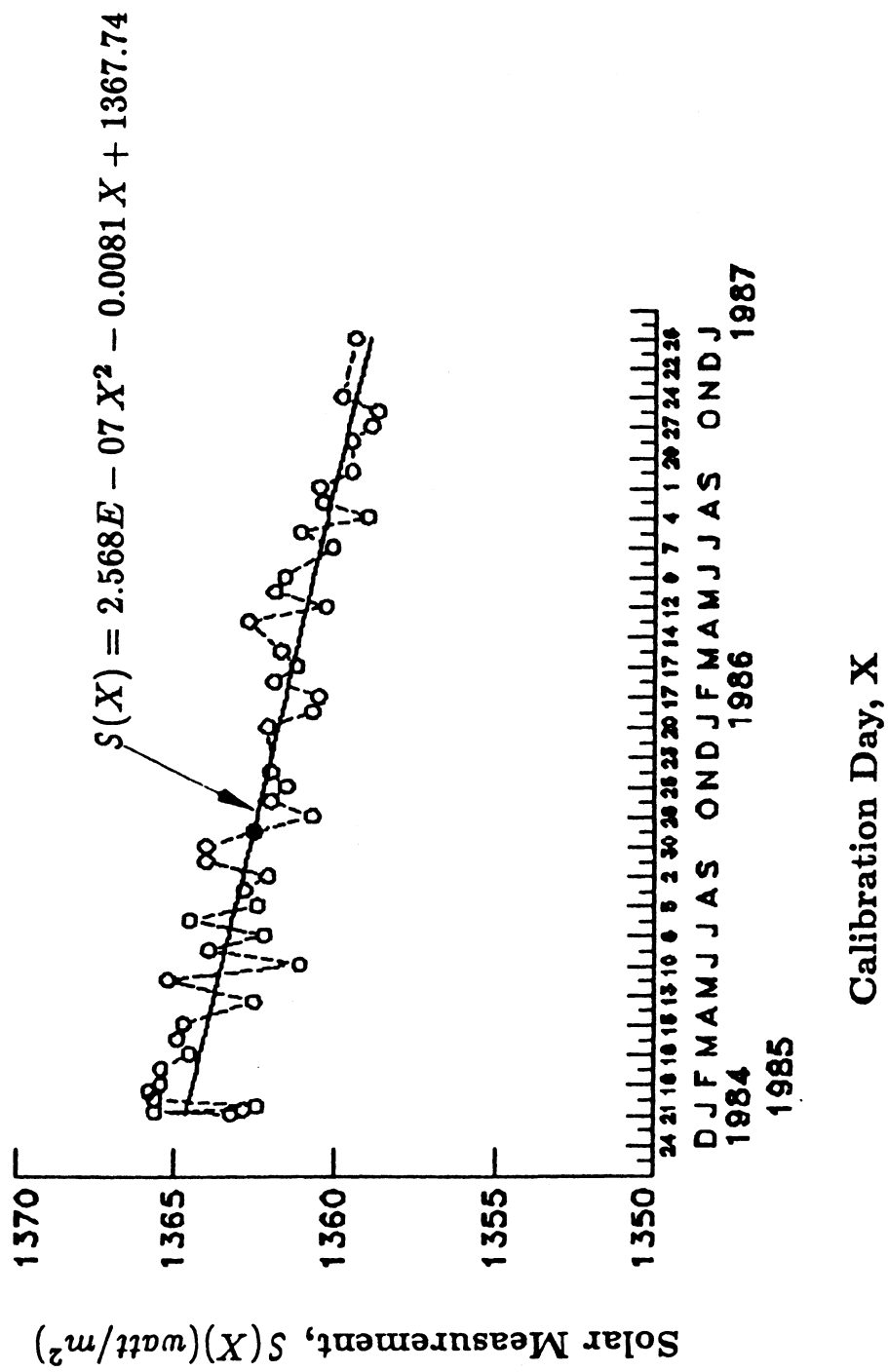


Figure 4.4 Solar Measurement vs Calibration Day
For NOAA-9 MFOVSW Sensor

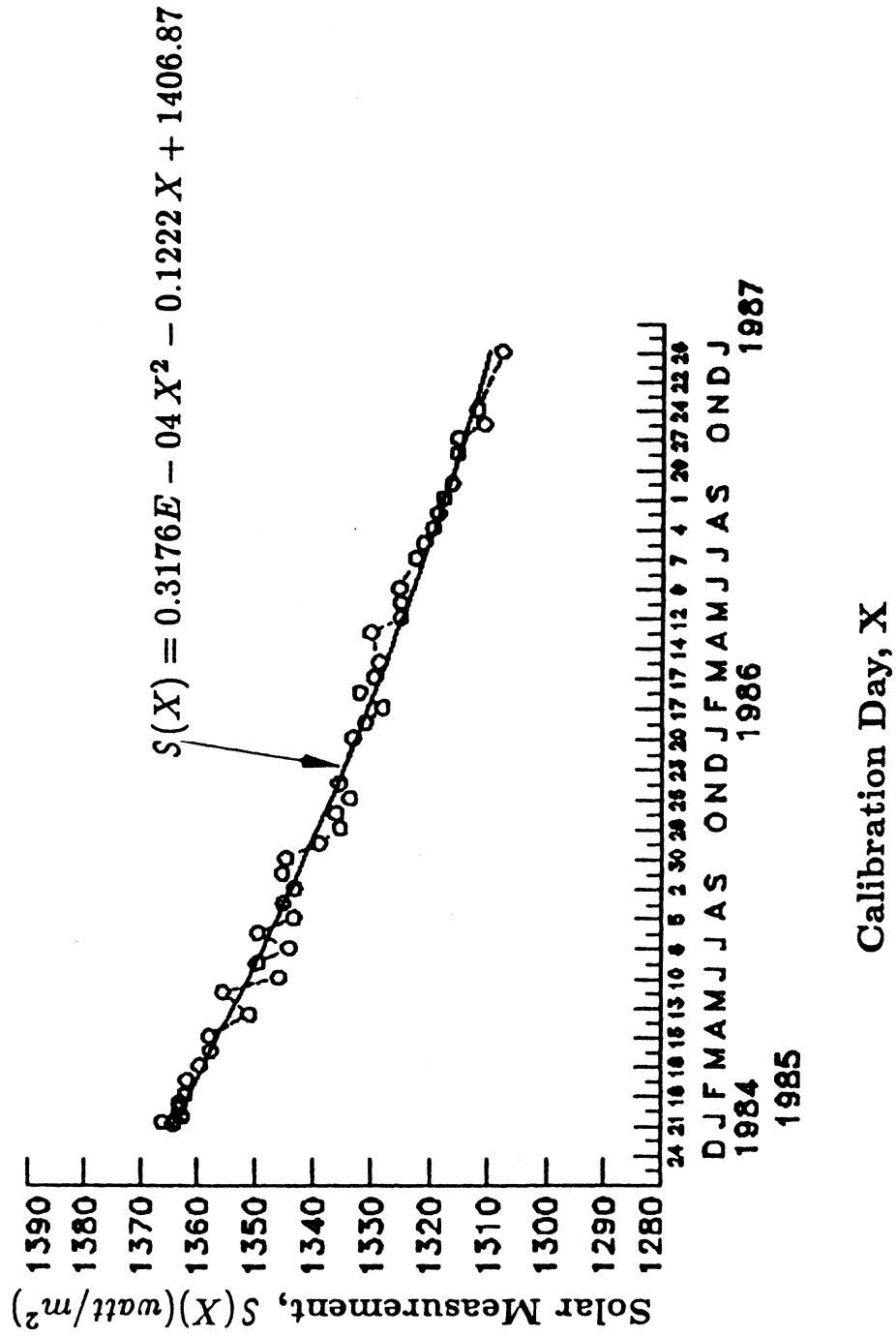


Figure 4.5 Solar Measurement vs Calibration Day
For NOAA-9 WFOVSW Sensor

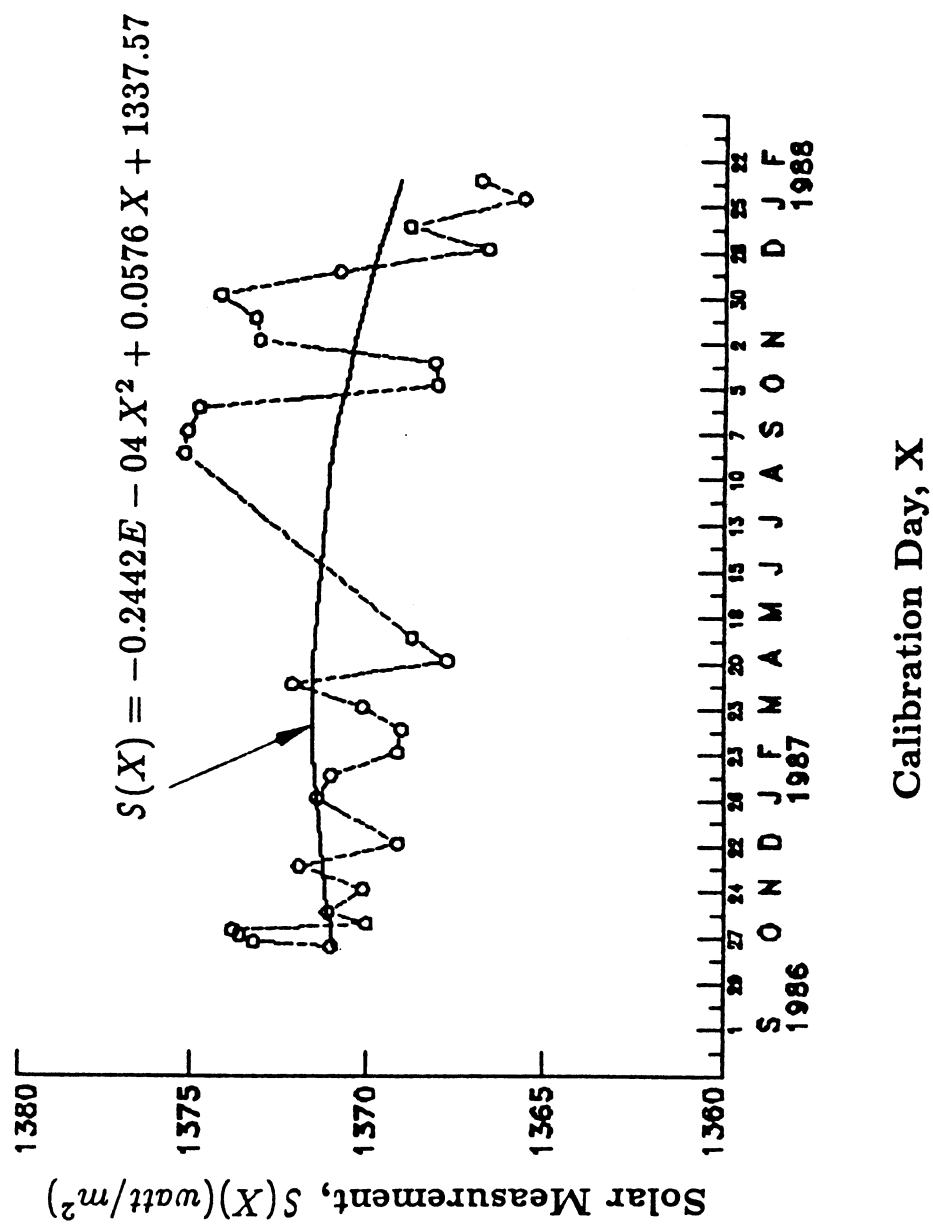


Figure 4.6 Solar Measurement vs Calibration Day
For NOAA-10 MFOVSW Sensor

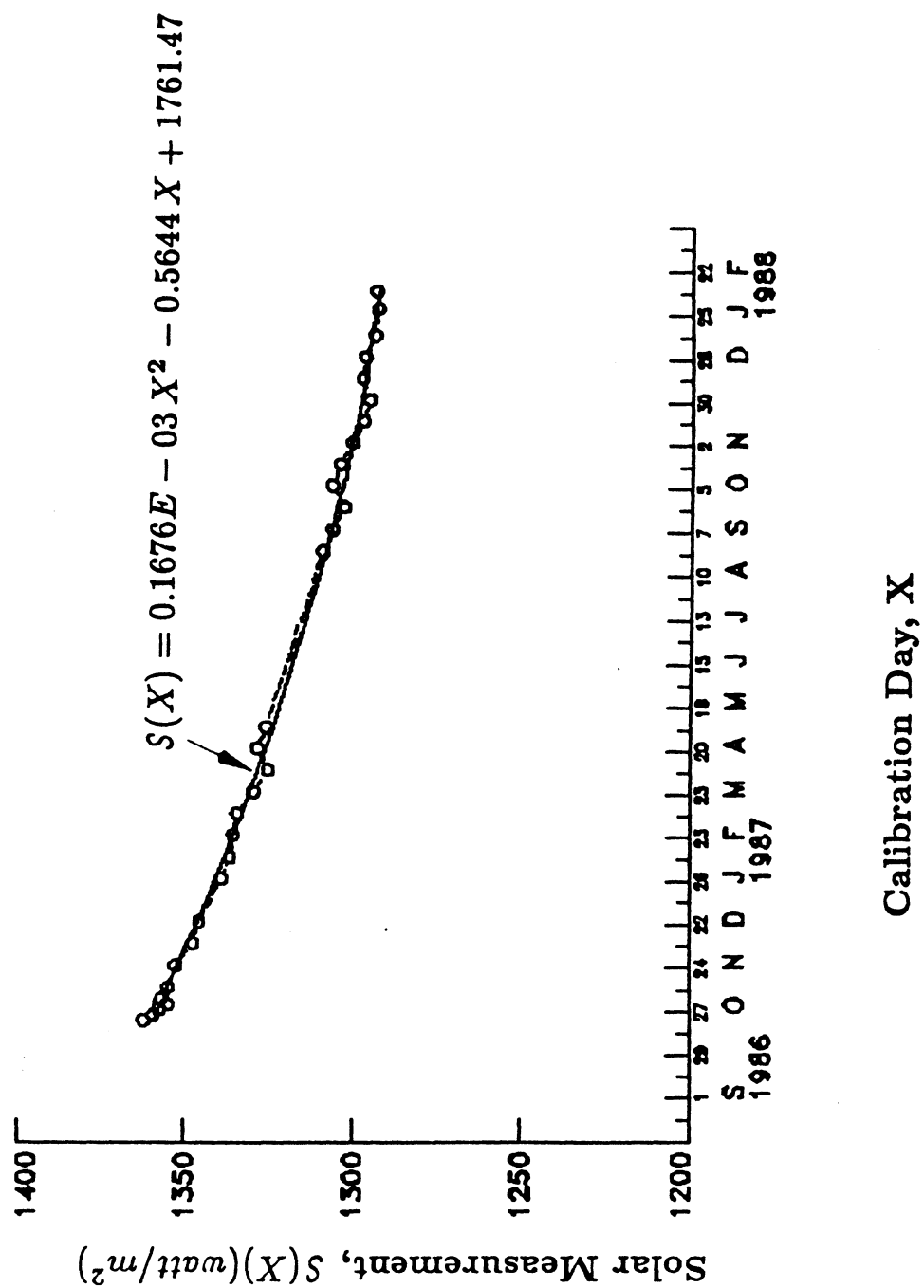


Figure 4.7 Solar Measurement vs Calibration Day
For NOAA-10 WFOVSW Sensor

values for ERBS and NOAA-9 shortwave sensors on the first day of solar calibration are found to be 2-3% higher than the a_1 values determined from the ground data.

Figures 4.2 to 4.7 show the solar measurements with curve fit equation of 2^{nd} order. Note that January 1, 1984 is considered as a reference day ($X=1$). This equation is used to compute the degradation factor. Data used in Figs. 4.2 to 4.7 are given in Appendix C.

4.2.4 A_F Term of NOAA-9 Shortwave Channels.

In analyzing the instrument validation (IVT) tapes, a strong correlation between MFOVSW (night-time) energy and FOVL temperature was found. Figure 4.7a shows this correlation for April 6, 1985. This procedure has been repeated for many days. In conclusion, the A_F term is changed from -4.8983 to 0.7092 to remove the effects of this correlation. Similar analysis was performed on the WFOVSW channel where the value of the A_F term changed from -5.1897 to -0.354.

Further, such analyses were performed on the ERBS and NOAA-10 shortwave sensors, where no strong correlations were found.

4.3 Total Channel Offsets

The offset for total channels can be estimated by using internal blackbody sources (IBB) or space-look data. It is found that IBB data is more stable than the space-look data. Therefore, the IBB source data is used to determine the offset in this study. The offset term, B_{EDMT} , can be estimated as

$$B_{EDMT} = f(B'_{ICS} - \Delta B + B_{MRBB-IBB})$$

where B'_{ICS} is the ground offset given in Tables 3.1 - 3.3. ΔB is a change in offset obtained by looking at IBB source data. ΔB can be expressed as

$$\Delta B = \epsilon \sigma T_{IBB}^4 - E'_T$$

Solar Zenith Angle, $\theta_0 > 120^\circ$

Correlation = 0.98

April 6, 1985

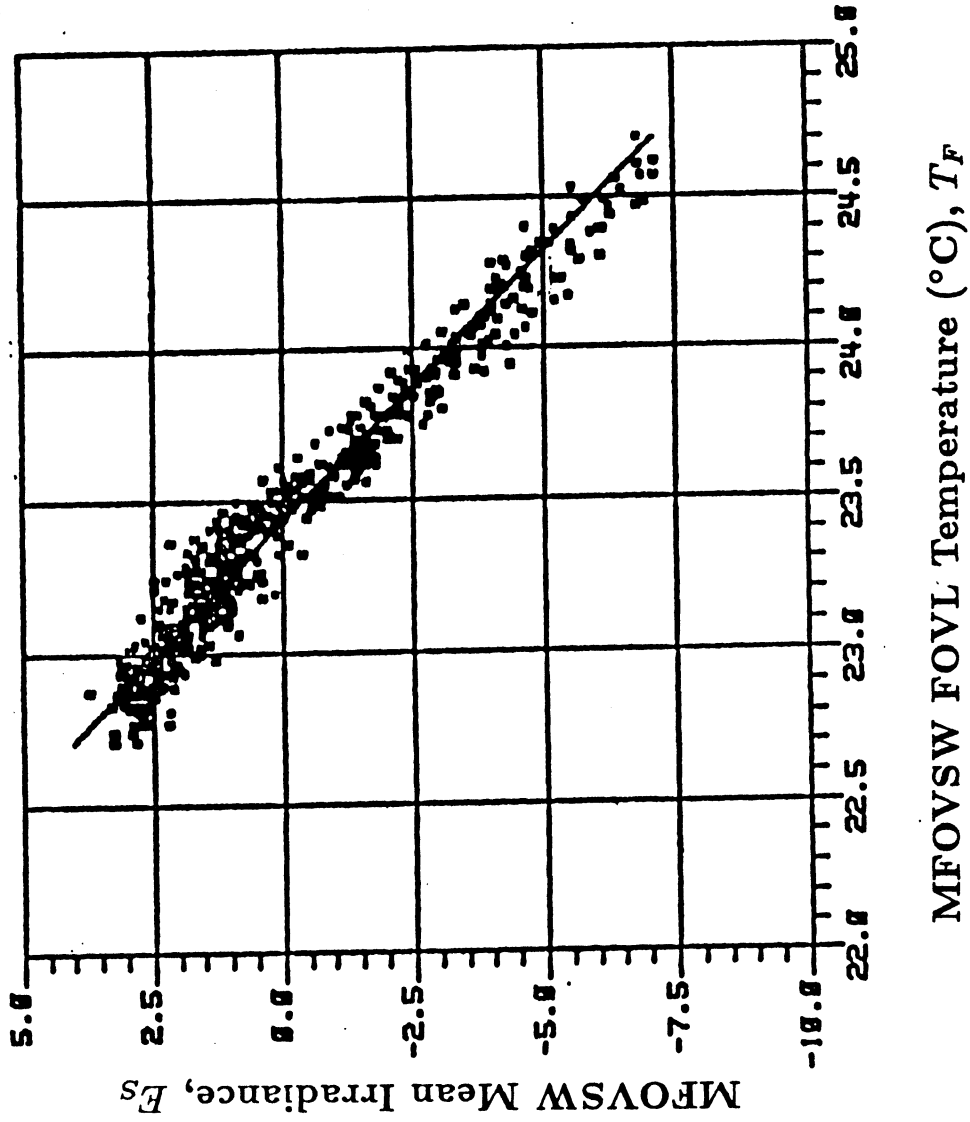


Figure 4.7a MFOVSW (Nighttime) Energy vs MFOVSW FOVL Temperature, T_F

where ϵ and T_{IBB} are the surface emissivity and temperature of the internal blackbody source. The emissivity, ϵ , is considered to be unity. E'_T is the estimated energy computed by using ground count conversion coefficients given in Tables 3.1 - 3.3. $B_{MRBB-IBB}$ is a correction factor detailed in Appendix B.

Figures 4.8 and 4.9 show offset variation, ΔB , in MFOVT and WFOVT channels of ERBS, respectively. One can note from these figures that there is a distinct jump in offset shown by a solid circle. The clear cause of this jump is not known. However, the temperature transients caused by a full-sun condition on the satellite may have been a real reason. At this point, this condition is not fully investigated and modeled. Therefore, the data points belonging to hot orbit conditions are excluded in determining the final ΔB term.

Figures 4.10 and 4.11 show the changes in offset determined by using IBB data for NOAA-9 MFOVT and WFOVT channels, respectively. Note that the MFOVT channel is drifting continuously in a quadratic form. An equation to represent the IBB data for MFOVT channel is obtained by using the least square method. This equation is displayed in Fig. 4.10 and used to compute the offset for every day. On the other hand, NOAA-9 WFOVT channel, shown in Fig. 4.11, does not depict a similar trend. Therefore, the ΔB is computed by taking an average over a small portion of data to reduce the uncertainty.

Figures 4.12 and 4.13 represent the offset variations for NOAA-10 MFOVT and WFOVT channels respectively. ΔB of both channels seems to be fluctuating and drifting. Total channels' offset terms for December 1986 and January 1987 are estimated by taking the average over small data points. Results are discussed in the next section.

4.4 Shortwave Channel Offsets

All nonscanner shortwave channels except WFOVSW of NOAA-10, observe the dark-side of the Earth. Assuming zero shortwave energy during night time, the offset term, B_{EDMT} , can be computed by using degraded in-flight count conversion coefficients as

• Hot Orbit Conditions

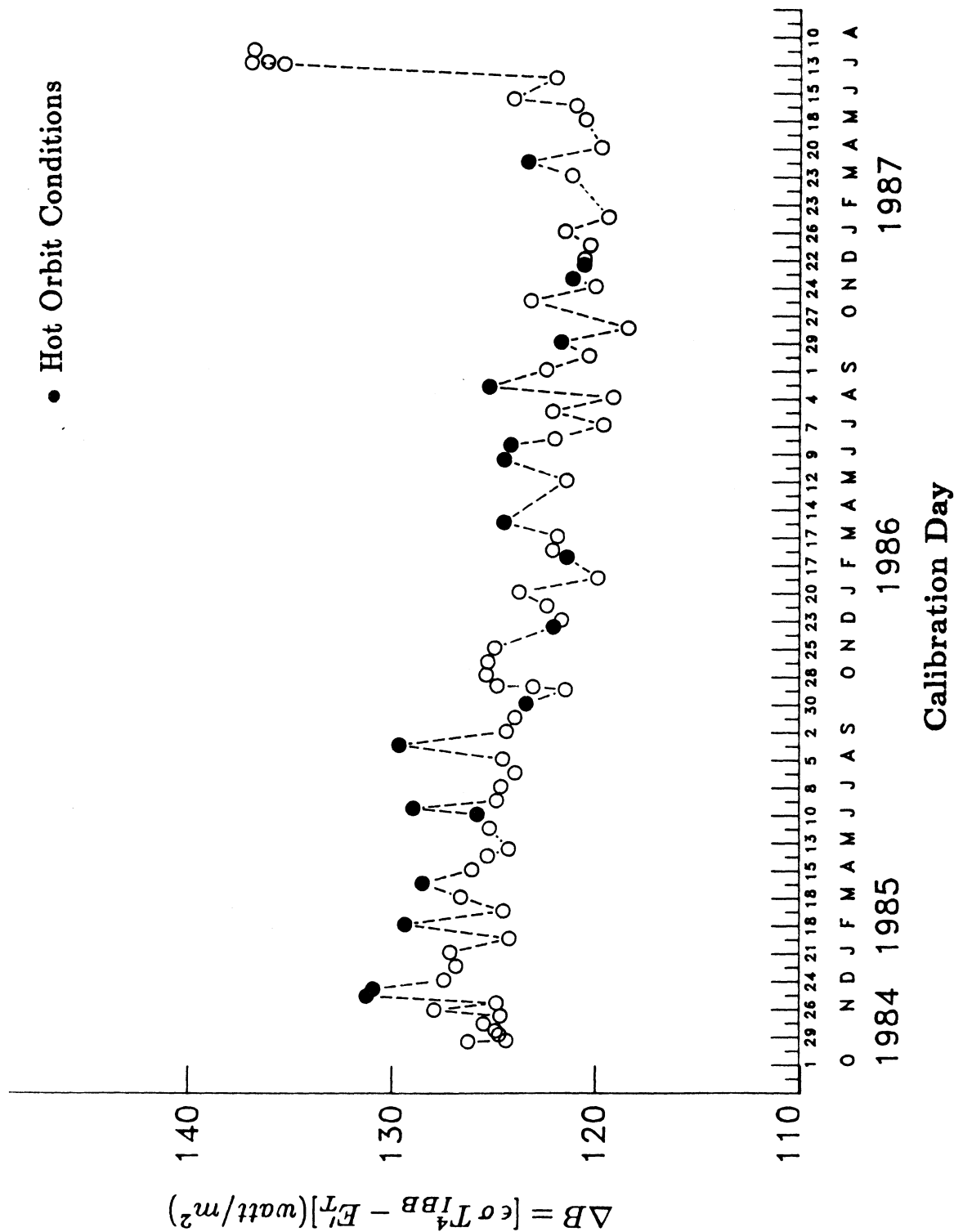


Figure 4.8 Offset Variation Obtained By Using IBB Data vs Calibration Day
For ERBS MFOVT Channel

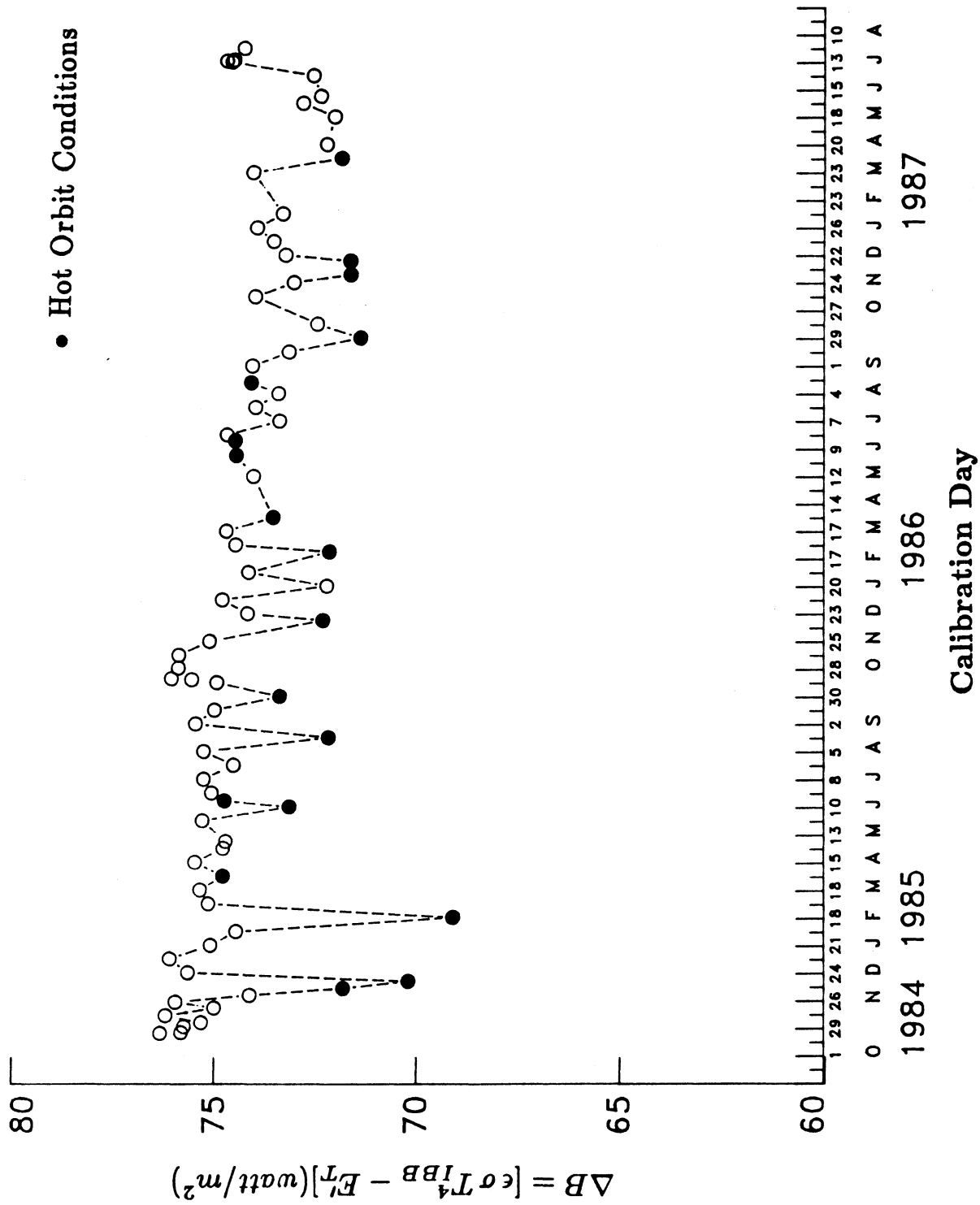
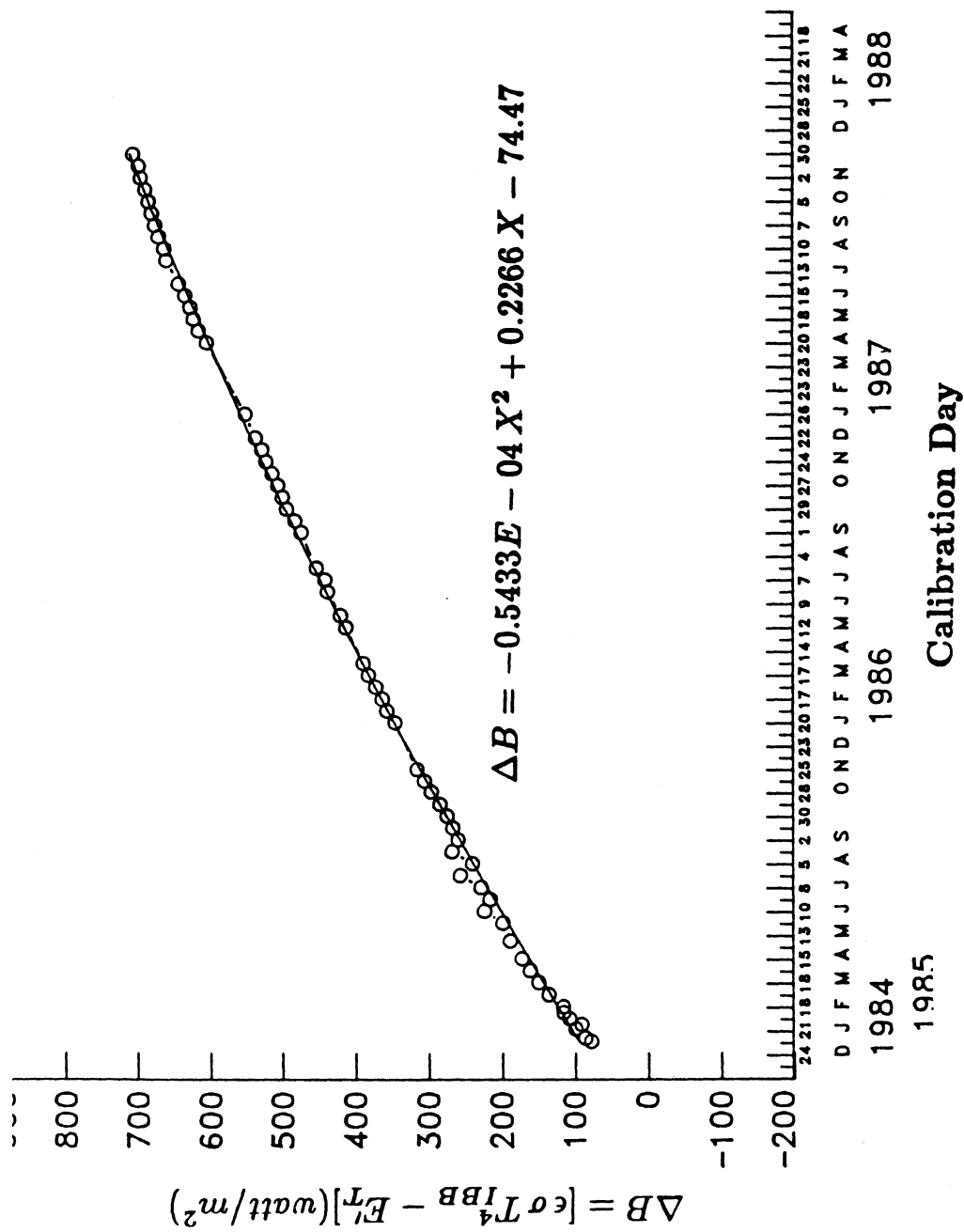


Figure 4.9 Offset Variation Obtained By Using IBB Data vs Calibration Day
For ERBS WFOVT Channel



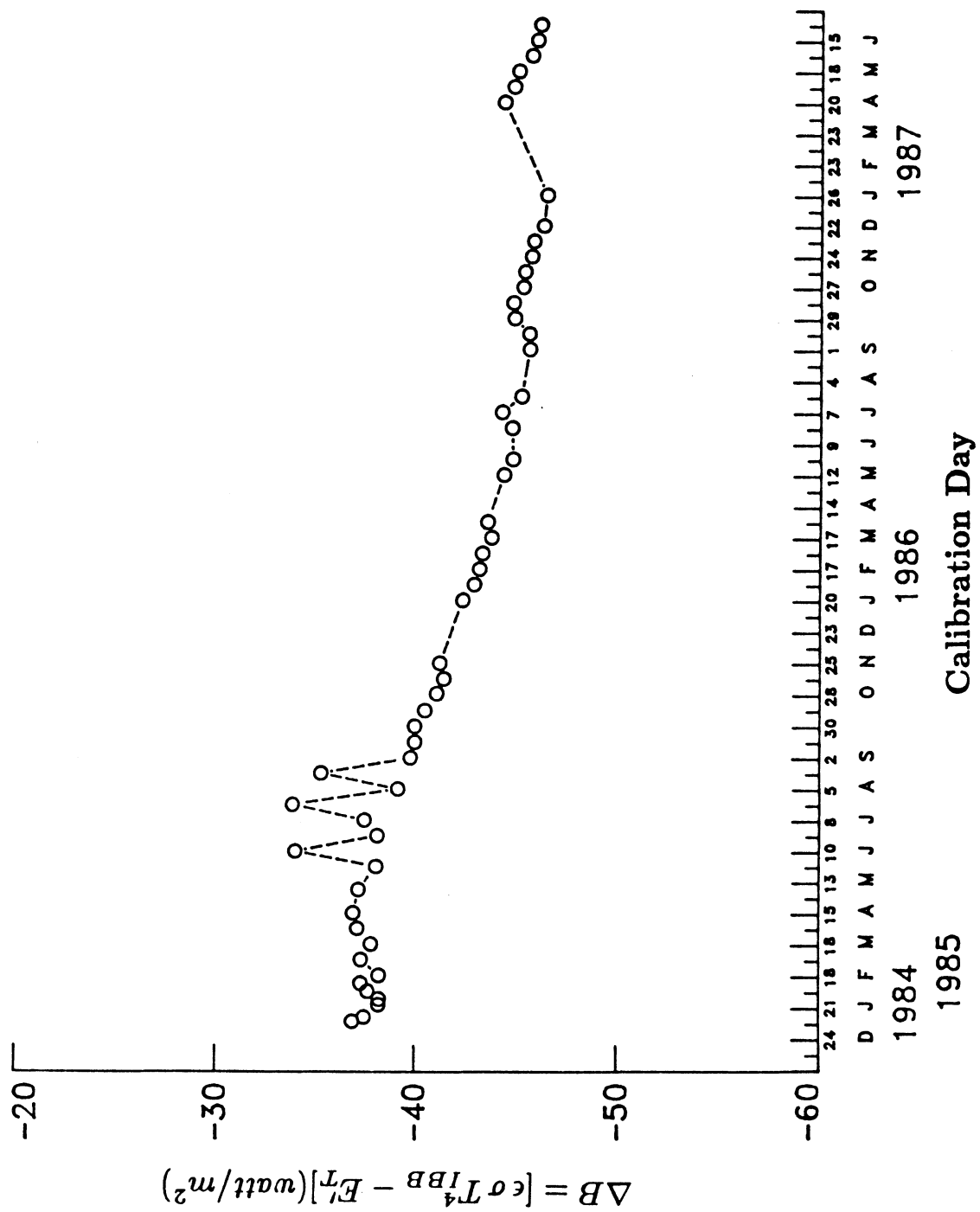


Figure 4.11 Offset Variation Obtained By Using IBB Data vs Calibration Day
For NOAA-9 WFOVT Channel

**Figure 4.12 Offset Variation Obtained By Using IBB Data vs Calibration Day
For NOAA-10 MFOVT Channel**

$$B_{EDMT} = -A_V V^2 - A_F T_F - A_R V_R^2 - A_E E_T \quad (4.3)$$

Each term of the right hand side of Eq. (4.3) is known. Darkside data are stripped from ID1 (telemetry) tapes. Sun blips data on WFOVSW are excluded in this analysis. Note that the data selected here is considered to be free from temperature transients, i.e., mid-night time data. The solar zenith angle, θ_o , is greater than 120° . Tables 4.1 and 4.2 show typical examples of April 6, 1985 darkside analysis for ERBS and NOAA-9 nonscanner shortwave sensors respectively. Figures 4.14 and 4.15 show the variation of ≈ 2 watt/m² shortwave energy for ERBS MFOVSW channel obtained from the darkside data analysis with degraded count conversion coefficients, for April 1985. Figure 4.16 shows the final offset term for ERBS MFOVSW channel obtained after subtracting the estimated shortwave energy given in Fig. 4.15 from the degraded in-flight offset. Similar analyses are performed with ERBS WFOVSW (Figs. 4.17 - 4.19) channel, which is found to be more stable than the ERBS MFOVSW channel. This procedure is employed to determine the NOAA-9 nonscanner shortwave offsets for April 1985, which are shown in Figs. 4.20 - 4.25. Note that NOAA-9 shortwave channels are more stable than ERBS shortwave channels. Further, the procedure detailed above is used to determine final in-flight shortwave offsets of ERBS and NOAA-9 nonscanner channels for other months discussed later.

4.4.1 NOAA-10 Shortwave Offsets Determination.

NOAA-10 is a terminator orbital satellite which leads WFOVSW channel to only a few days of darkside data in a whole year. To overcome this problem, the WFOVSW offsets are determined using SWICS lamps-off and space-look data. However, it is appropriate to perform similar analyses first on ERBS and NOAA-9 shortwave channels to find a correlation, if any exists, between darkside and SWICS lamps-off data. Figures 4.26 and 4.27 show the differences in offset levels obtained by analyzing the SWICS lamps-off, space-look and darkside data with the same in-flight count conversion coefficients. One can note

Table 4.1 ERBS Shortwave Offset Determination

For April 6, 1985 Using Darkside Data Analysis

DARKSIDE ANALYSIS OF ID1 TAPE EA2105

ERBE, ERBS(FM1) NONSCANNER

SHORTWAVE CHANNEL NIGHT ONLY ESTIMATES (W/(M**2))

TAPE BEGINNING DATE : 4/ 6/85 TIME : 0: 0: 0 JULIAN : 2446161.500010967255

TAPE ENDING DATE : 4/ 6/85 TIME : 23:59:28 JULIAN : 2446162.499640598893

COUNT CONVERSION COEFFICIENTS : 12/19/85

NUMBER OF RECS ON GOK2105 : 2700

THE JULIAN TIME MIDPOINT USED = 2446161.907788500190

COSINE INDICATOR FOR MFOV NIGHT = .70

COSINE INDICATOR FOR WFOV NIGHT = .70

CONSTANTS FOR MFOV-TW CHANNEL

BCNSTT = 1003.67000 AFOVUE = -.92300 AAPERT = .00000
AVOLTG = -22.70930 AHTSNK = .00000 ACALHT = 25.12760
AEHATT = .00000 TNOHNL(6) = 292.42333 TNOHNL(8) = 306.706111

DATA MANAGEMENT B CONSTANT = 1273.576736

CONSTANTS FOR WFOV-TW CHANNEL

BCNSTT = 1295.41300 AFOVUE = -1.39680 AAPERT = .00000
AVOLTG = -22.78730 AHTSNK = .00000 ACALHT = 26.11610
AEHATT = .00000 TNOHNL(6) = 292.561429 TNOHNL(8) = 306.841429

DATA MANAGEMENT B CONSTANT = 1704.062804

CONSTANTS FOR MFOV-SW CHANNEL

BCNSTT = 1377.47000 AFOVUE = 1.22410 AAPERT = .00000
AVOLTG = -25.56300 AHTSNK = .00000 ACALHT = 29.07650
AEHATT = -.03755 TNOHNL(6) = 293.655500 TNOHNL(8) = 306.703500

DATA MANAGEMENT B CONSTANT = 1010.006302

CONSTANTS FOR WFOV-SW CHANNEL

BCNSTT = 1127.32000 AFOVUE = -.64020 AAPERT = .00000
AVOLTG = -25.77500 AHTSNK = .00000 ACALHT = 26.74610
AEHATT = -.03074 TNOHNL(6) = 293.449091 TNOHNL(8) = 306.872273

DATA MANAGEMENT B CONSTANT = 1317.533701

ORBIT	MEDIUM FIELD-OF-VIEW SHORTWAVE						WIDE FIELD-OF-VIEW SHORTWAVE						ORBIT
	RECORD MEAN	RECORD STANDARD DEVIATION	SAMPLE MINIMUM	SAMPLE MAXIMUM	NO OF SAMPLES	NO OF RECORDS	RECORD MEAN	RECORD STANDARD DEVIATION	SAMPLE MINIMUM	SAMPLE MAXIMUM	NO OF SAMPLES	NO OF RECORDS	
1	.8431	.680	-3.4440	4.1347	720	36	8.2766	1.095	6.3784	18.6053	720	36	61.5048
2	-.5206	.996	-5.1740	4.6872	920	46	7.3902	.603	5.3256	9.0423	920	46	61.5719
3	-.7403	.800	-7.2237	3.5750	920	46	7.6714	.748	5.0951	9.5348	920	46	61.6389
4	.3622	.525	-6.1603	7.6393	920	46	7.9061	1.187	5.1221	9.9247	920	46	61.7043
5	.3338	.636	-5.4936	4.7130	920	46	7.8186	1.168	5.4065	9.9871	920	46	61.7733
6	-.0028	.789	-6.0509	4.3307	920	46	7.5360	.807	5.4059	9.5360	920	46	61.8408
7	-1.1843	.595	-8.1456	4.1823	900	45	7.6746	.755	5.5293	9.3295	900	45	61.9078
8	.0343	.952	-5.2021	4.9145	920	46	7.4361	.803	5.0106	9.5119	920	46	61.9748
9	.0403	.871	-4.5098	7.5093	920	46	7.3998	.862	5.1389	9.3410	920	46	62.0422
10	-.2053	.586	-4.7979	4.5653	920	46	7.3388	.856	4.9754	9.1734	920	46	62.1093
11	-2.2543	1.459	-8.0802	2.6958	920	46	7.2512	.735	5.0093	9.3774	920	46	62.1767
12	-2.2350	.960	-7.4982	2.9421	900	45	7.1039	.601	5.1122	8.8026	900	45	62.2437
13	-.0247	.742	-5.9814	3.1537	920	46	7.4572	.838	5.4156	9.5494	920	46	62.3108
14	-1.0324	.751	-6.4591	2.2256	920	46	7.5229	.721	5.4428	9.1958	920	46	62.3782
15	.4860	1.035	-9.0609	5.1782	900	45	7.0552	.981	5.4084	10.1301	900	45	62.4452
TOTALS	-.5320	1.306	-9.0609	7.6393	13540	677	7.5710	.898	4.9754	18.6053	13540	677	(RECORDS)

BEDMT MFOV SW VALUE = 1010.5303

BEDMT WFOV SW VALUE = 1309.9627

Table 4.2 NOAA-9 Shortwave Offset Determination

For April 6, 1985 Using Darkside Data Analysis

DARKSIDE ANALYSIS OF ID1 TAPE EA2381

ER&E, NOAA-9(FM2) NONSLANNER

SHORTWAVE CHANNEL NIGHT ONLY ESTIMATES (W/(H**2))

TAPE BEGINNING DATE : 4/ 6/85 TIME : 01 01 4 JULIAN : 2446161.500050276518

TAPE ENDING DATE : 4/ 6/85 TIME : 23:59:48 JULIAN : 2446162.499865114689

COUNT CONVERSION COEFFICIENTS : 11/12/37

NUMBER OF RECS ON 60K2381 : 2687

THE JULIAN TIME MIDPOINT USED = 2446161.876346498728

COSINE INDICATOR FOR MFOV NIGHT = .65

COSINE INDICATOR FOR WFOV NIGHT = .65

CONSTANTS FOR MFOV-TW CHANNEL

BCNSTT = 1056.28000 AFOVUE = -.52740 AAPERT = .00000
AVOLT6 = -22.55660 AHTSNK = .00000 ACALHT = 23.91330
AEHATT = 1 TNOHNL(6) = 292.702105 TNOHNL(8) = .000000

DATA MANAGEMENT B CONSTANT = 1210.651090

CONSTANTS FOR MFOV-TW CHANNEL

BCNSTT = 1358.75000 AFOVUE = -.39770 AAPERT = .00000
AVOLT6 = -22.86210 AHTSNK = .00000 ACALHT = 24.76350
AEHATT = 1 TNOHNL(6) = 293.387080 TNOHNL(8) = 306.447917

DATA MANAGEMENT B CONSTANT = 1475.430042

CONSTANTS FOR MFOV-SW CHANNEL

BCNSTT = 1049.00000 AFOVUE = .70920 AAPERT = .00000
AVOLT6 = -25.45990 AHTSNK = .00000 ACALHT = 28.98700
AEHATT = -.03604 TNOHNL(6) = 293.413200 TNOHNL(8) = .000000

DATA MANAGEMENT B CONSTANT = 840.911359

CONSTANTS FOR MFOV-SW CHANNEL

BCNSTT = 1260.00000 AFOVUE = -.35400 AAPERT = .00000
AVOLT6 = -25.98800 AHTSNK = .00000 ACALHT = 30.13110
AEHATT = -.03465 TNOHNL(6) = 294.316000 TNOHNL(8) = 306.872273

DATA MANAGEMENT B CONSTANT = 1364.187664

ORBIT	MEDIUM FIELD-OF-VIEW SHORTWAVE						WIDE FIELD-OF-VIEW SHORTWAVE						ORBIT
	RECORD MEAN	RECORD STANDARD DEVIATION	SAMPLE MINIMUM	SAMPLE MAXIMUM	NO OF SAMPLES	NO OF RECORDS	RECORD MEAN	RECORD STANDARD DEVIATION	SAMPLE MINIMUM	SAMPLE MAXIMUM	NO OF SAMPLES	NO OF RECORDS	
1	.3708	.690	-6.4305	5.5705	1060	53	4.2398	.600	-1.2884	9.0121	1060	53	61.5223
2	-.2104	.440	-6.1480	2.6538	1060	53	4.3137	.709	-.3204	8.3601	1060	53	61.5930
3	.0221	.388	-6.4627	5.7007	1040	52	4.4959	.556	-.8849	8.5047	1040	52	61.6638
4	.0831	.388	-5.8840	3.9466	1040	52	4.4903	.534	-.9758	9.9484	1040	52	61.7349
5	.3315	.427	-4.3702	4.3330	1040	52	4.3668	.695	-1.6360	8.6250	1040	52	61.8052
6	.1827	.372	-6.8592	3.9073	1060	53	4.6331	.624	-3.1845	9.0766	1060	53	61.8763
7	.0897	.370	-6.1202	4.5161	1040	52	4.5771	.717	-1.9189	8.8654	1040	52	61.9471
8	.0302	.447	-6.2566	3.6144	1060	53	4.6107	.765	-2.8065	9.1659	1060	53	62.0180
9	.7210	.525	-7.1235	6.3852	1060	53	4.5428	.939	-3.1489	9.4066	1060	53	62.0888
10	.3775	.532	-6.6304	4.5187	1040	52	4.5914	.821	-1.5213	9.2682	1040	52	62.1595
11	-.0906	.621	-5.7049	5.8688	1020	51	4.2800	.839	-2.6377	9.0152	1020	51	62.2302
12	.5241	.443	-5.9619	5.1994	1040	52	4.3745	.858	-2.8509	8.4025	1040	52	62.3013
13	.1079	.490	-5.5090	4.1312	1060	53	4.2077	.899	-4.3758	8.2208	1060	53	62.3721
14	-.1684	.517	-5.0276	2.9265	1060	53	4.2167	1.071	-4.7929	8.4297	1060	53	62.4428
TOTALS	.1695	.544	-7.1235	6.3852	14680	734	4.4242	.782	-4.7929	9.9484	14680	734	(RECORDS)

BEDMT MFOV SW VALUE = 840.7418

BEDMT WFOV SW VALUE = 1359.7636

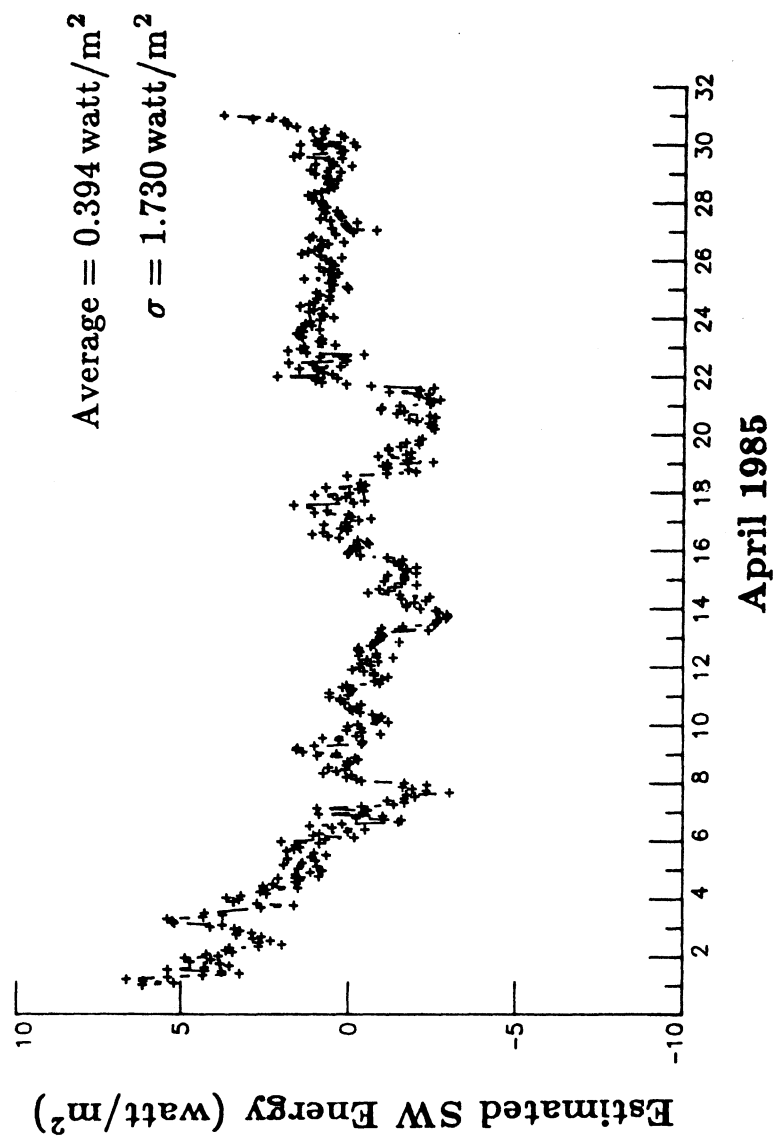


Figure 4.14 Estimated Shortwave Energy (Orbital Average)
From Darkside Data Analysis For ERBS MFOVSW Channel For April 1985

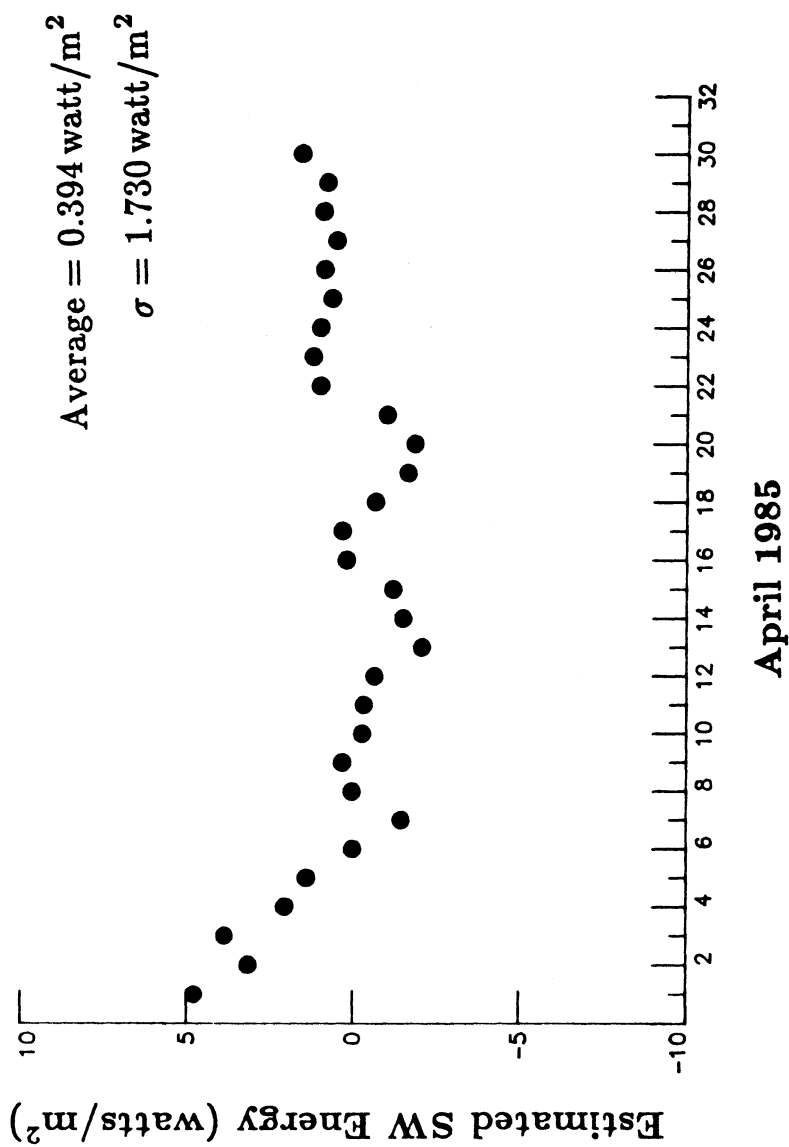


Figure 4.15 Estimated Shortwave Energy (Daily Average)
 From Darkside Data Analysis For ERBS MFOVSW Channel For April 1985

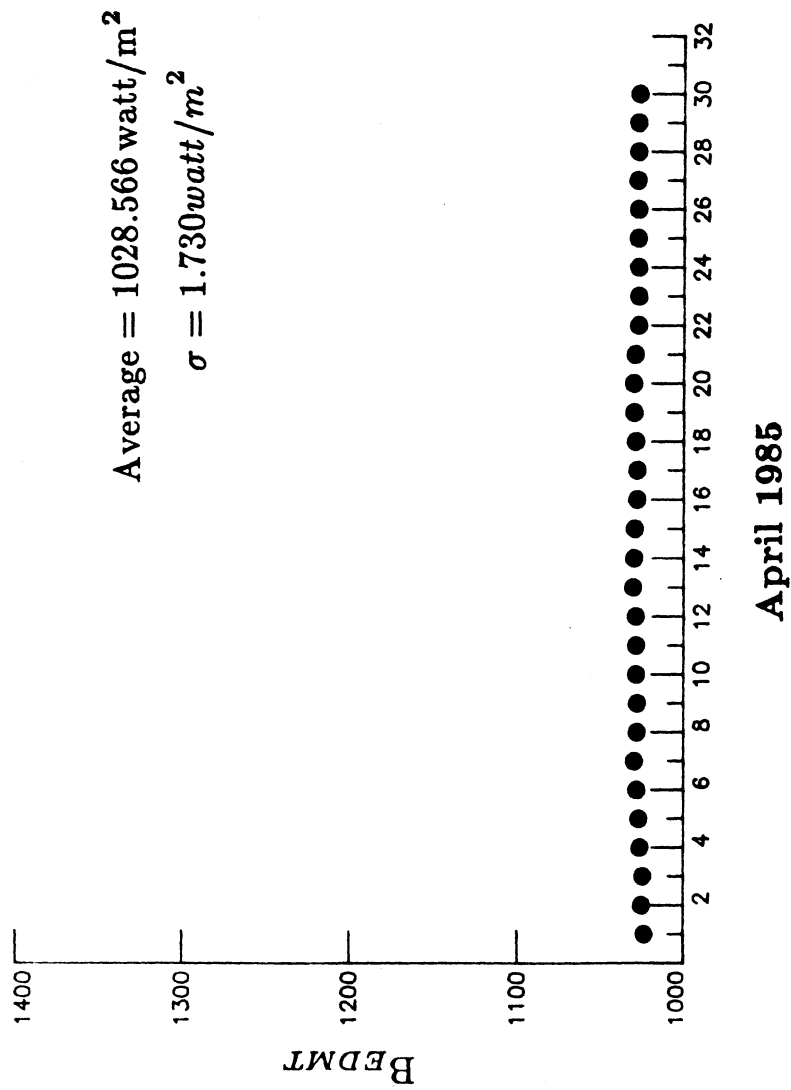


Figure 4.16 Final Offset Term For ERBS MFOVSW Channel For April 1985

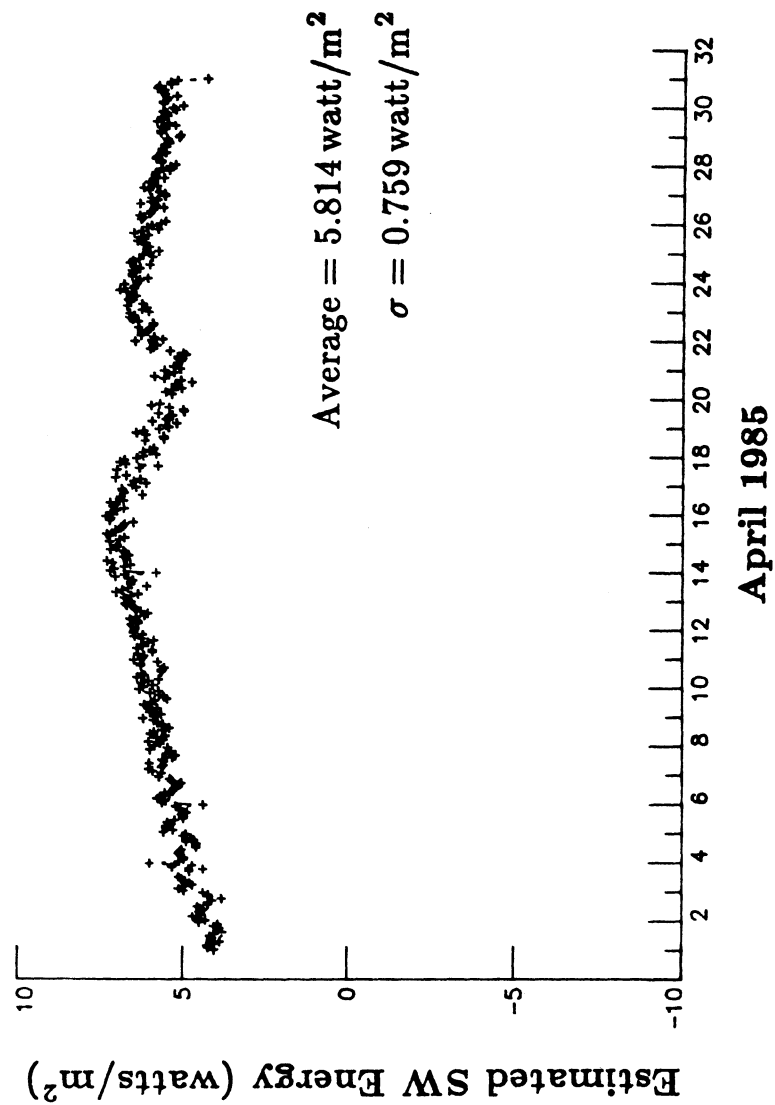


Figure 4.17 Estimated Shortwave Energy (Orbital Average)
 From Darkside Data Analysis For ERBS WFOVSW Channel For April 1985

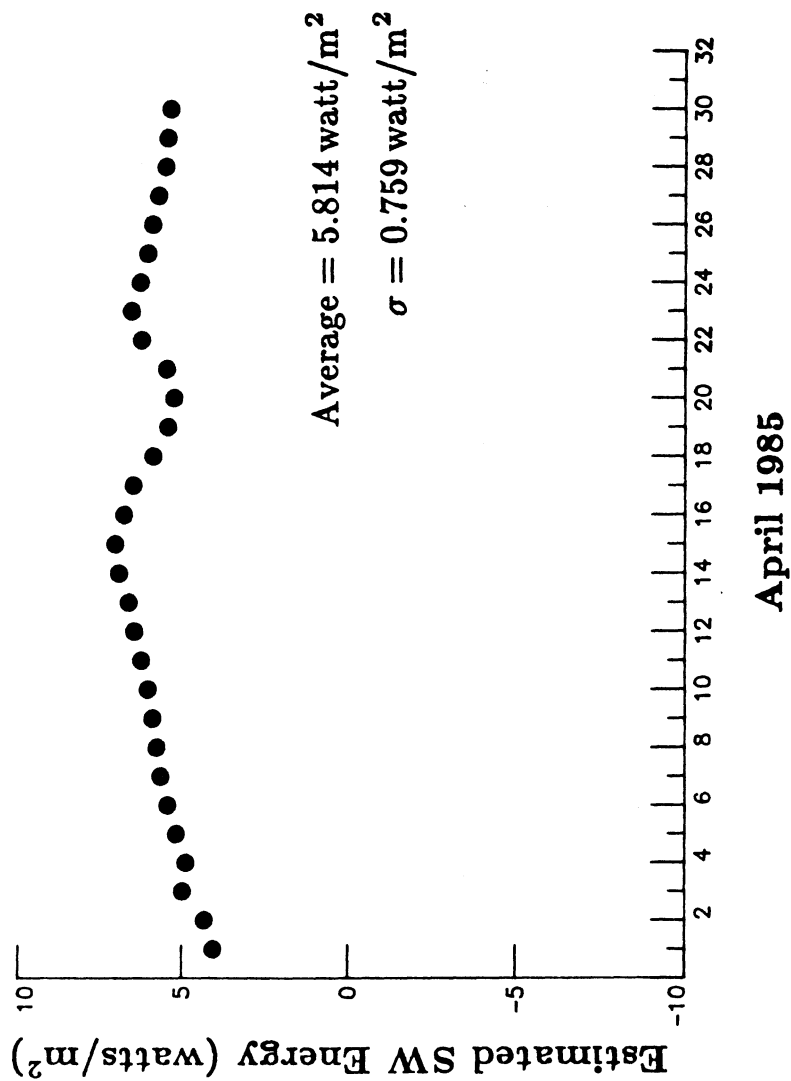


Figure 4.18 Estimated Shortwave Energy (Daily Average)
 From Darkside Data Analysis For ERBS WFOVSW Channel For April 1985

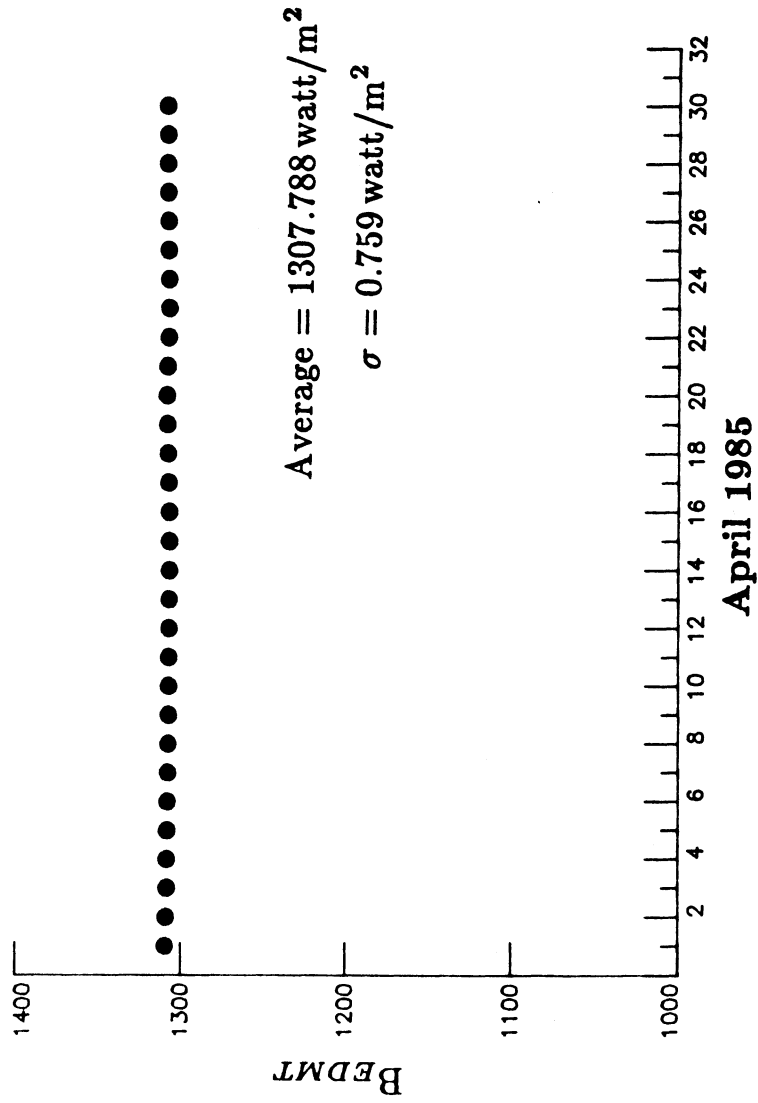


Figure 4.19 Final Offset Term For ERBS WFOVSW Channel For April 1985

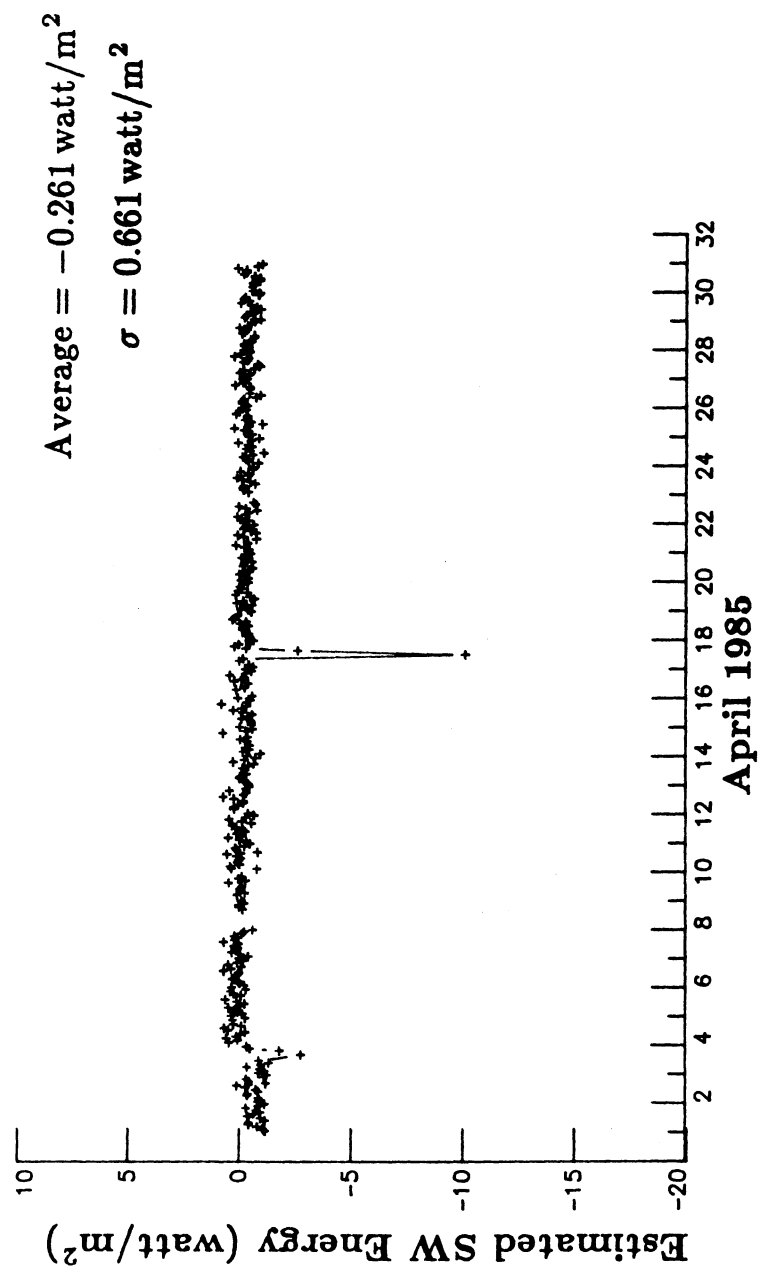


Figure 4.20 Estimated Shortwave Energy (Orbital Average)
 From Darkside Data Analysis For NOAA-9 MFOVSW Channel For April 1985

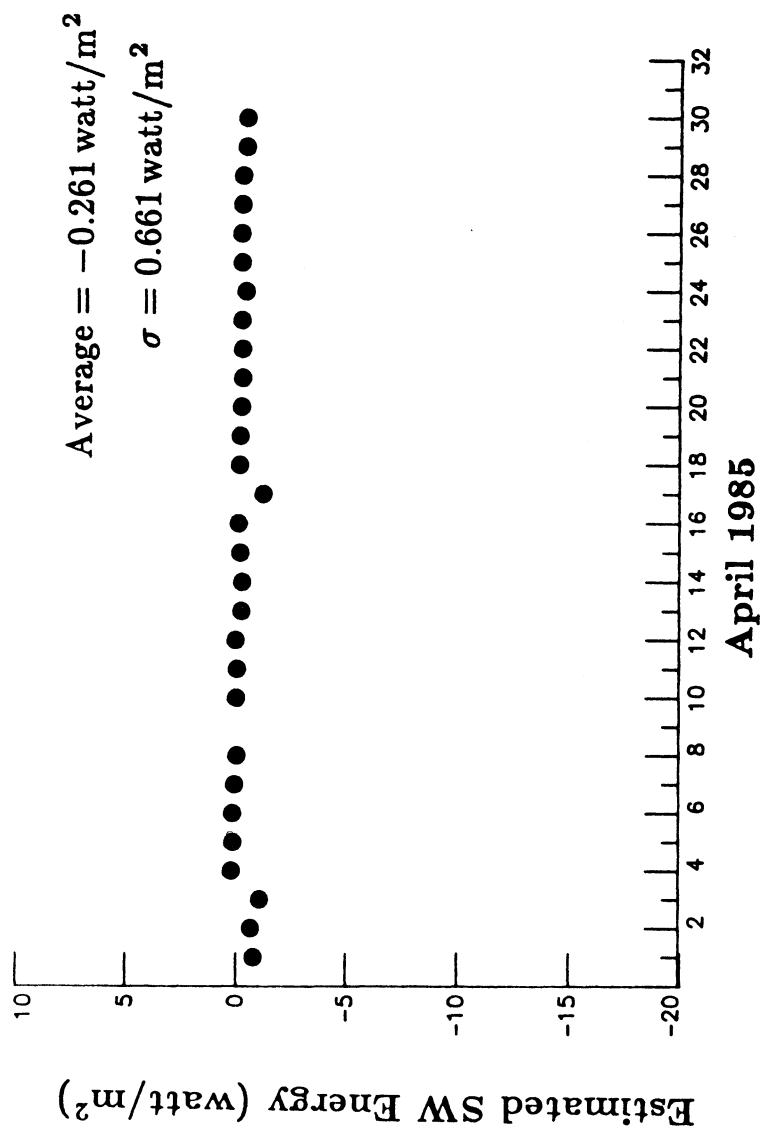


Figure 4.21 Estimated Shortwave Energy (Daily Average)
 From Darkside Data Analysis For NOAA-9 MFOVSW Channel For April 1985

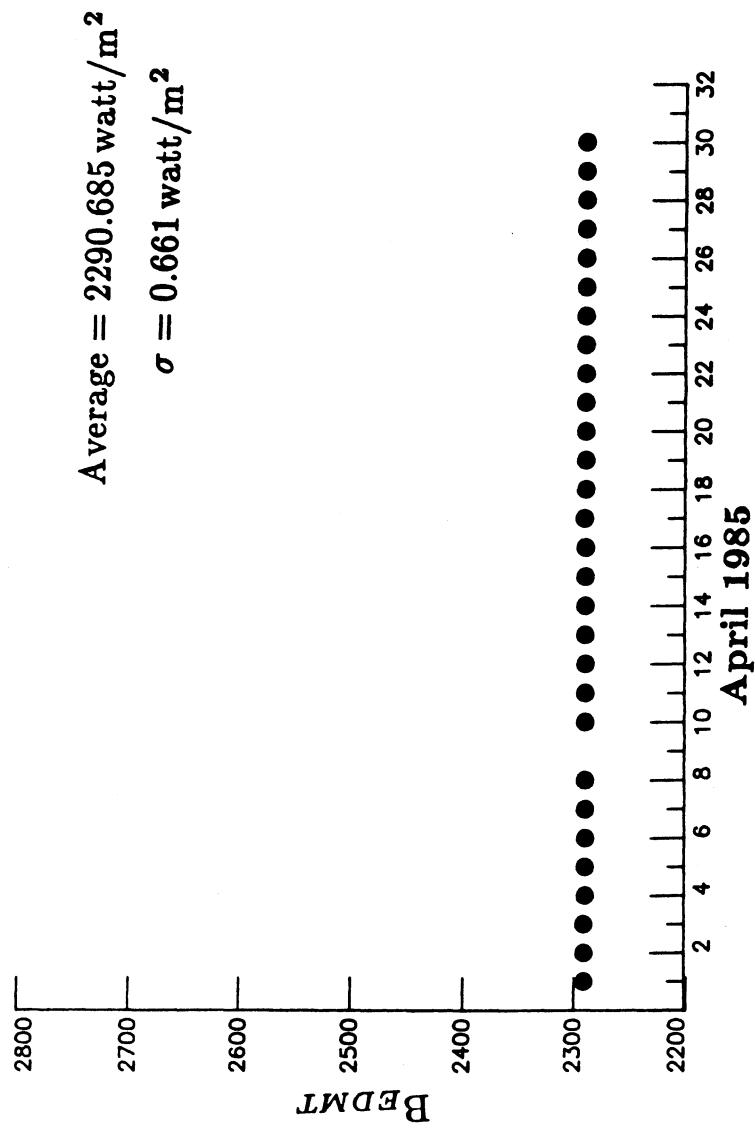


Figure 4.22 Final Offset Term For NOAA-9 MFOVSW Channel For April 1985

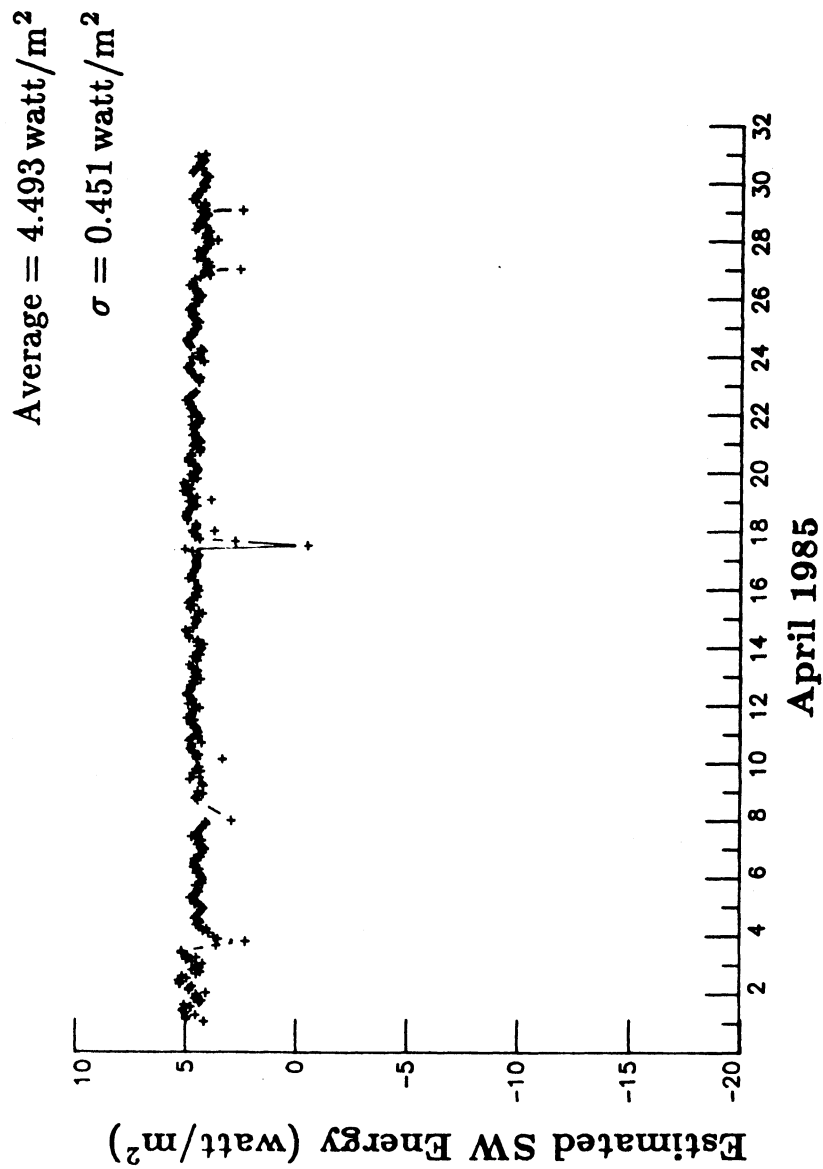


Figure 4.23 Estimated Shortwave Energy (Orbital Average)
 From Darkside Data Analysis For NOAA-9 WFOVSW Channel For April 1985

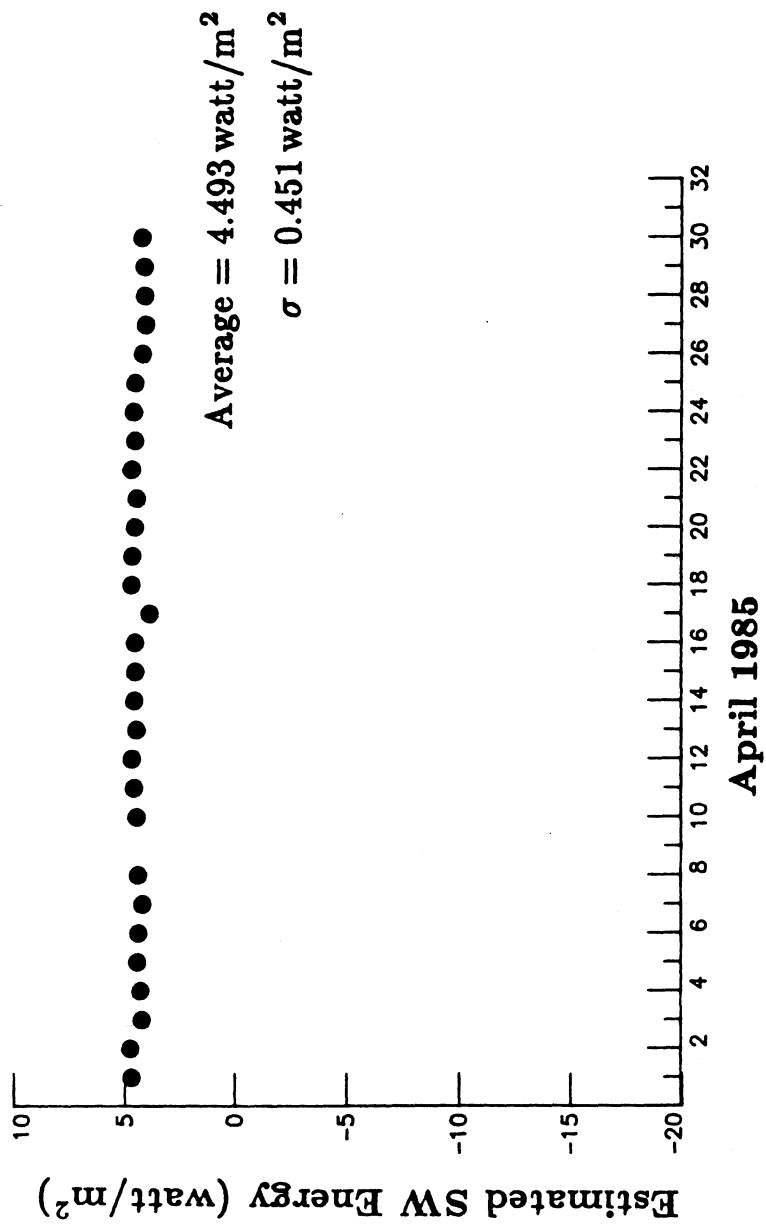


Figure 4.24 Estimated Shortwave Energy (Daily Average)
From Darkside Data Analysis For NOAA-9 WFOVSW Channel For April 1985

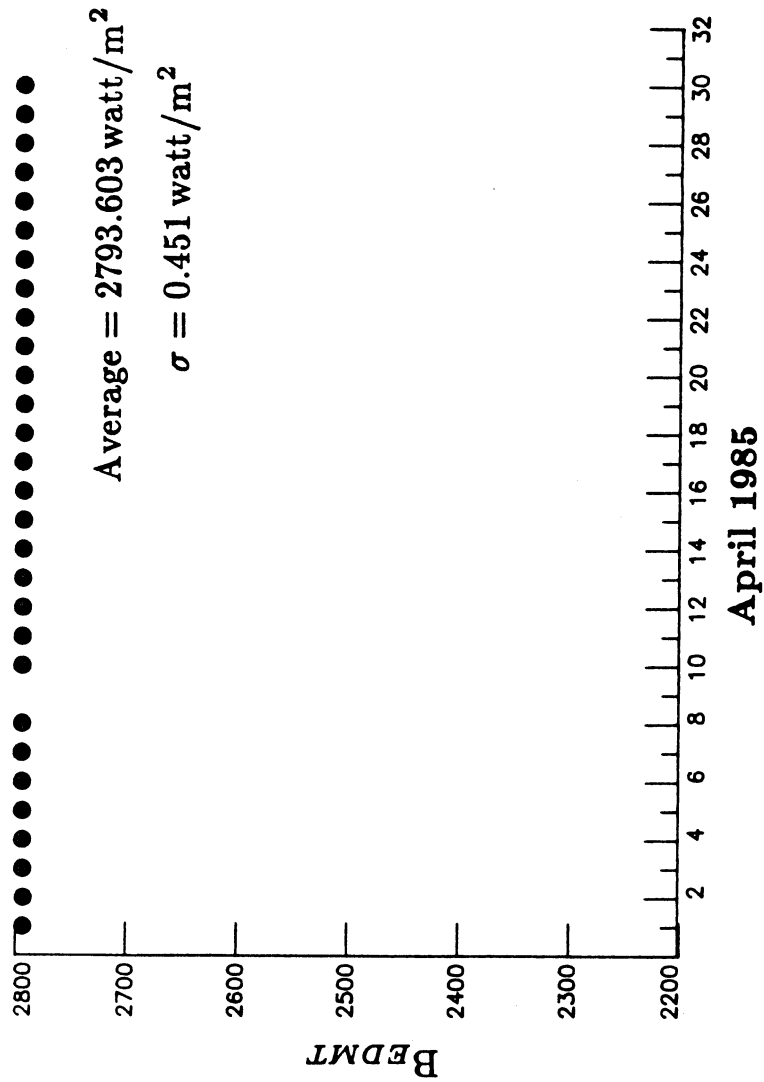


Figure 4.25 Final Offset Term For NOAA-9 WFOVSW Channel For April 1985

○ (LAMPS-OFF - DARKSIDE): MEAN = -1.6447, σ = 1.0971
 □ (SPACE-LOOK - DARKSIDE): MEAN = -5.9372, σ = 1.6041
 ◆ (LAMPS-OFF - SPACE-LOOK): MEAN = 4.2925, σ = 1.2724

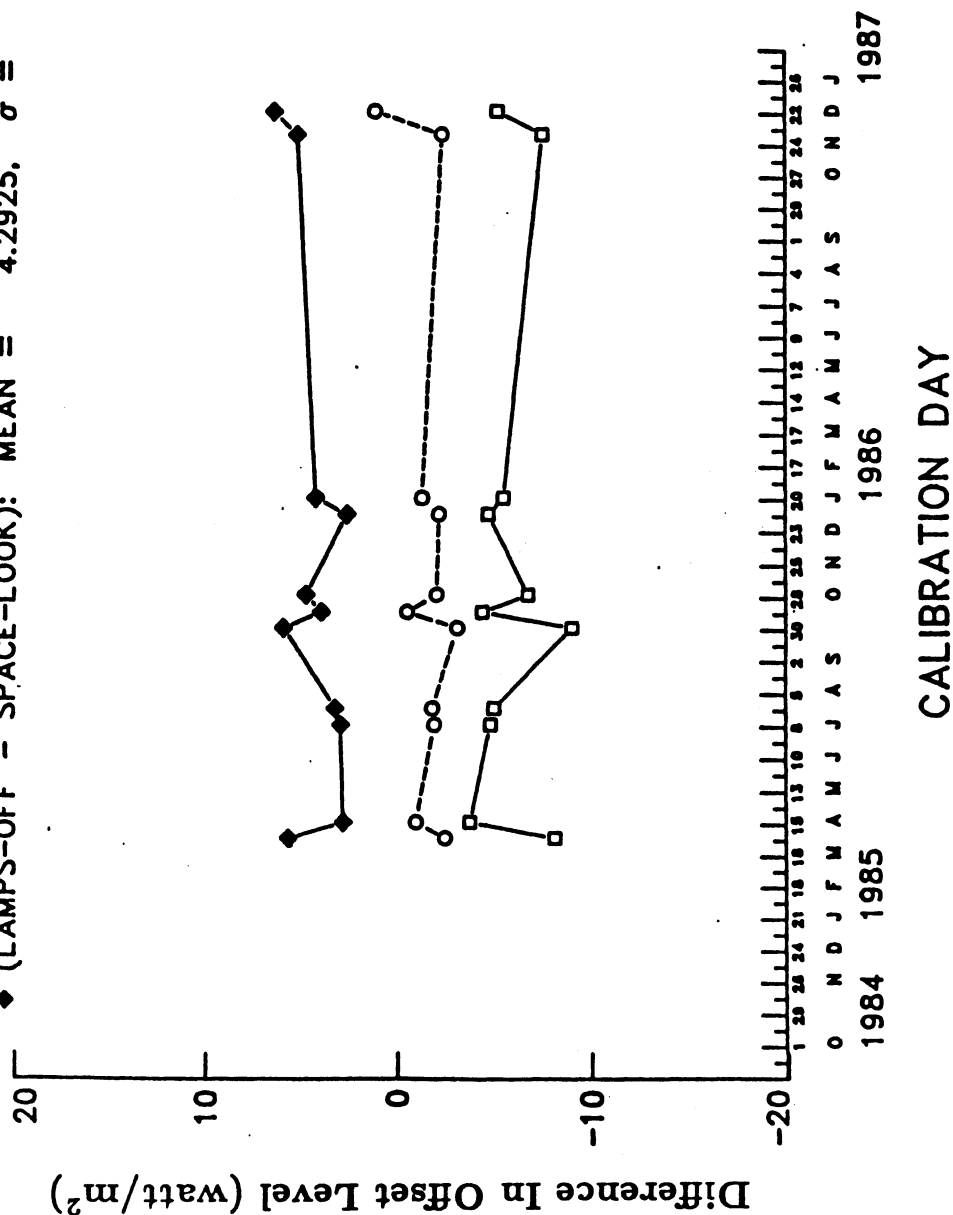


Figure 4.26 Differences In Offset Levels By Looking At Different Data Sources for ERBS WFOVSW Channel

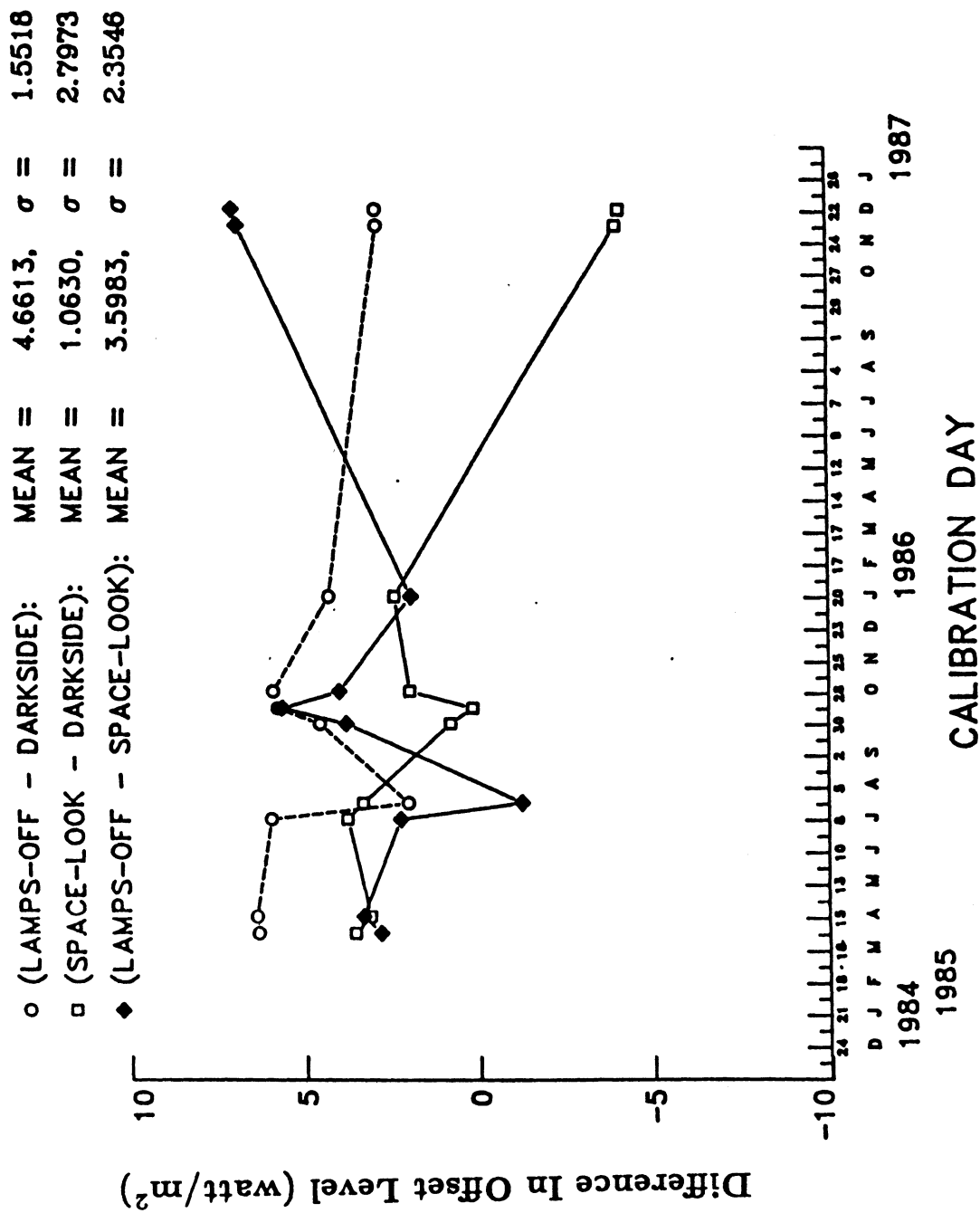


Figure 4.27 Differences In Offset Levels By Looking At
 Different Data Sources for NOAA-9 WFOVSW Channel

from these figures that the magnitude of differences are found within ± 6 watt/m² with mixed signs. However, the important point to be mentioned here is that the standard error with SWICS lamps-off - darkside is smaller than the other cases.

A similar analysis procedure is also performed on NOAA-10 WFOVSW channel. Table 4.3 details the offset terms for the NOAA-10 WFOVSW channel using SWICS lamps-off and darkside data. It is very clear from this table that the WFOVSW offset can be determined using SWICS lamps-off data within 2 watt/m². Also, note that the offset difference between SWICS lamps-off and space-look data is approximately 7 watt/m². At this juncture, it may be appropriate to use SWICS lamps-off data to determine the NOAA-10 WFOVSW offset term.

Further, the offset term for MFOVSW channel can also be determined using SWICS lamps-off data. Figs. 4.28 and 4.29 show the differences in offset terms for ERBS and NOAA-9 MFOVSW channels, respectively. Similar conclusions may be drawn as we have for WFOVSW channel. NOAA-10 MFOVSW channel sees the darkside of the Earth. Therefore one can always estimate the offset term for the MFOVSW channel from the Merge reports. However, the NOAA-10 MFOVSW channel offset can be determined by using the equation given below:

$$B_{EDMT} = B(\text{SWICS LAMPS-OFF}) - (\approx 12 \text{ watt/m}^2)$$

Final in-flight count conversion coefficients are given in the next section.

4.5 Final In-Flight Count Conversion Coefficients

This section describes the final in-flight count conversion coefficients for ERBS, NOAA-9 and NOAA-10 nonscanner channels produced using the procedures detailed earlier.

4.5.1 ERBS Nonscanner Results.

In-flight count conversion coefficients for total channel with their corresponding offset numbers are given in Tables 4.4 and 4.5. Tables 4.6 and 4.7 show the in-flight count

Table 4.3 NOAA-10 WFOVSW Offsets

CALIBRATION DAY	<i>BEDMT</i> DARKSIDE DATA	<i>BEDMT</i> SWICS LAMPS-OFF DATA	<i>BEDMT</i> SPACE-LOOK DATA
December 10, 1986	—	1420.02	1414.24
January 21, 1987	—	1427.11	1418.54
February 4, 1987	—	1430.81	1423.63
April 15, 1987	—	1441.65	1433.82
June 10, 1987	1453.30	1451.80	—
June 24, 1987	1453.30	1451.80	—
July 22, 1987	1457.60	1456.30	—
August 19, 1987	1461.20	1460.60	1452.65
September 2, 1987	—	1463.96	1456.14
December 23, 1987	—	1469.77	1462.77
January 20, 1988	—	1472.28	1465.40

ERBS MFOV-SW CHANNEL

○ (LAMPS-OFF - DARKSIDE): MEAN = 14.8098, σ = .5113
 □ (SPACE-LOOK - DARKSIDE): MEAN = .2207, σ = 2.3903
 ◆ (LAMPS-OFF - SPACE-LOOK): MEAN = 14.5891, σ = 2.3270

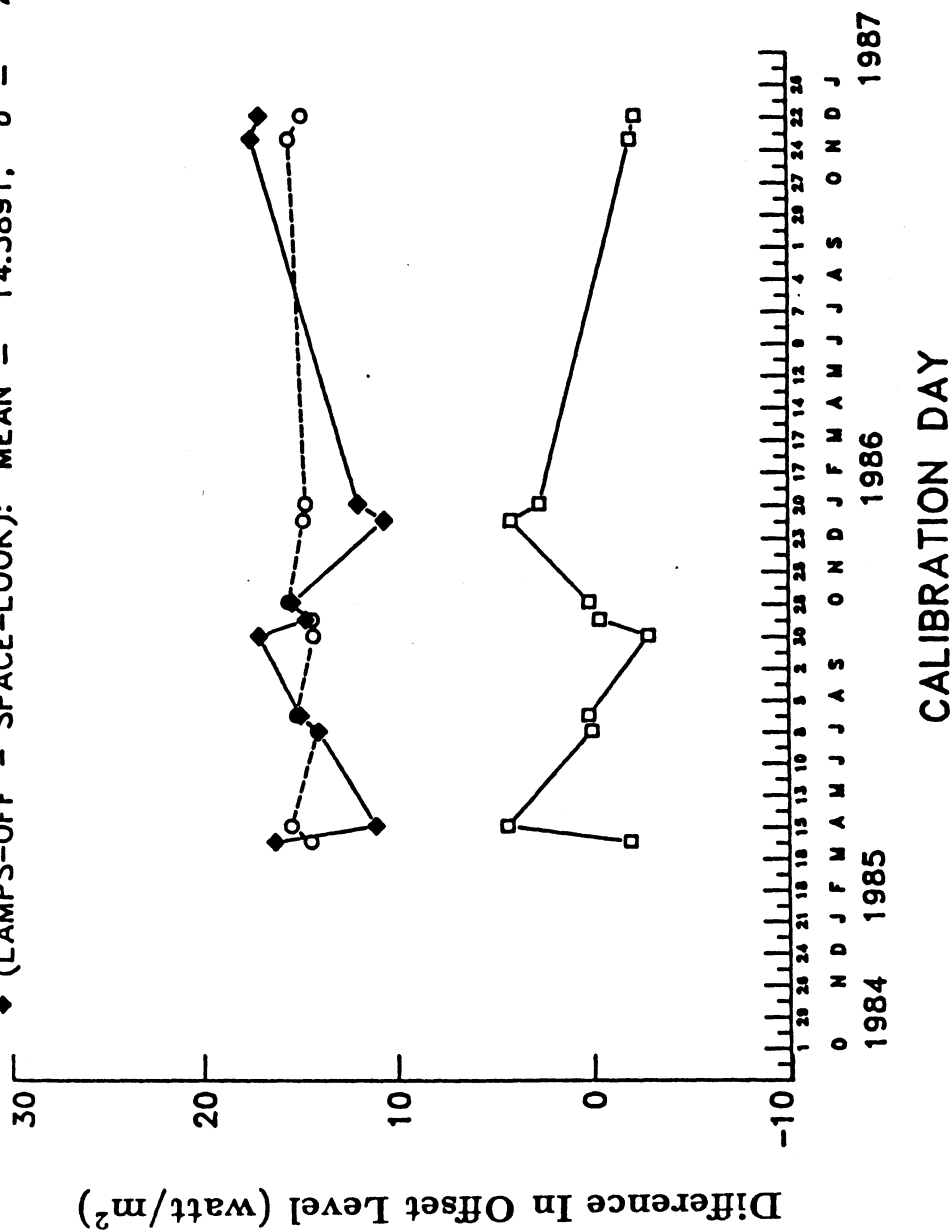
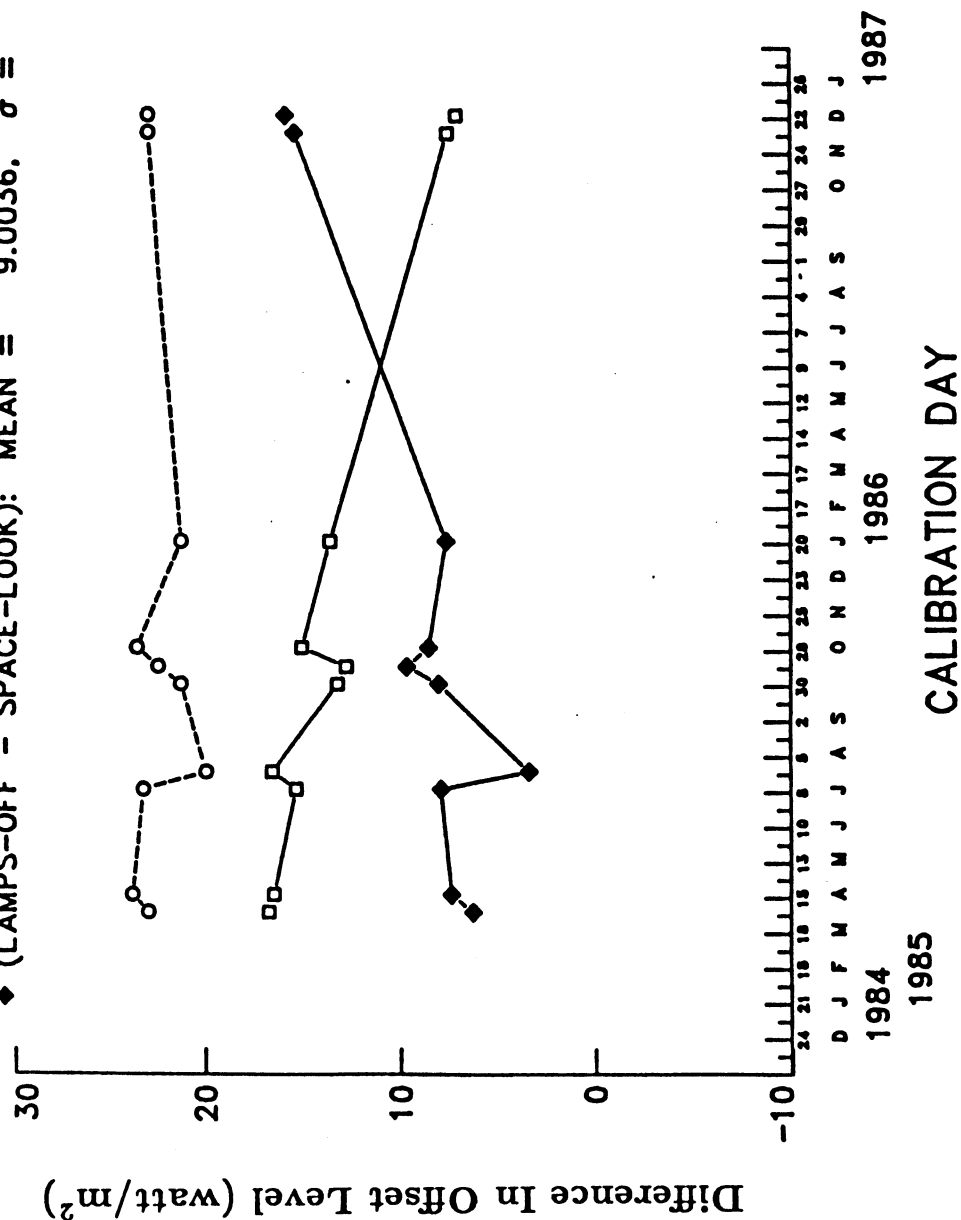


Figure 4.28 Differences In Offset Levels By Looking At Different Data Sources for ERBS MFOVSW Channel

NOAA-9 MFOV-SW CHANNEL

- (LAMPS-OFF - DARKSIDE): MEAN = 22.4196, σ = 1.1752
- (SPACE-LOOK - DARKSIDE): MEAN = 13.4160, σ = 3.3224
- ◆ (LAMPS-OFF - SPACE-LOOK): MEAN = 9.0036, σ = 3.6750



**Table 4.4 ERBS MFOV Total In-Flight
Count Conversion Coefficients**

A_V	A_F	A_R
-22.7093	-0.923	25.1276

APPLICABLE PERIOD	B_{EDMT}
11/01/84 – 11/30/84	1273.547
01/01/85 – 01/31/85	1273.577
04/01/85 – 04/30/85	1273.577
07/01/85 – 07/31/85	1274.130
08/01/85 – 08/31/85	1274.130
10/01/85 – 10/31/85	1274.130
01/01/86 – 01/31/86	1275.450
12/01/86 – 12/31/86	1275.450
01/01/87 – 01/31/87	1275.450

**Table 4.5 ERBS WFOV Total In-Flight
Count Conversion Coefficients**

A_V	A_F	A_R
-22.7873	-1.3968	26.1161

APPLICABLE PERIOD	B_{EDMT}
11/01/84 – 11/30/84	1703.070
01/01/85 – 01/31/85	1704.063
04/01/85 – 04/30/85	1704.063
07/01/85 – 07/31/85	1704.020
08/01/85 – 08/31/85	1704.020
10/01/85 – 10/31/85	1704.020
01/01/86 – 01/31/86	1705.050
12/01/86 – 12/31/86	1705.050
01/01/87 – 01/31/87	1705.050

**Table 4.6 ERBS MFOV SHORTWAVE In-Flight
Count Conversion Coefficients**

APPLICABLE PERIOD	A_V	A_E	A_F	A_R
11/01/84 – 11/30/84	–25.5337	–0.03751	1.2227	29.0431
01/01/85 – 01/31/85	–25.5458	–0.03753	1.2233	29.0570
04/01/85 – 04/30/85	–25.5630	–0.03755	1.2241	29.0765
07/01/85 – 07/31/85	–25.5791	–0.03758	1.2248	29.0948
08/01/85 – 08/31/85	–25.5843	–0.03758	1.2251	29.1007
10/01/85 – 10/31/85	–25.5942	–0.03760	1.2256	29.1120
01/01/86 – 01/31/86	–25.6082	–0.03762	1.2262	29.1279
12/01/86 – 12/31/86	–25.6490	–0.03768	1.2282	29.1744
01/01/87 – 01/31/87	–25.6520	–0.03768	1.2283	29.1778

Table 4.6 (Continued)
ERBS MFOV Shortwave In-Flight Offsets, B_{EDMT}

ATE	NOV 84	JAN 85	APRIL 85	JULY 85	AUG 85	OCT 85	JAN 86	DEC 86	JAN 87
1	1012.954	1010.674	1014.669	1018.715	1019.746	1019.061	1030.008	1029.495	1036.518
2	0000.000	1012.960	1016.341	1019.416	1021.483	1018.814	1030.288	1029.622	1036.544
3	0000.000	1014.819	1015.056	1019.621	1021.902	1019.177	1030.197	1029.003	1036.880
4	0000.000	1014.003	1016.909	1019.562	1021.779	1019.238	1028.391	1027.463	1036.799
5	1015.710	1012.919	1017.394	1019.724	1020.792	1019.875	1028.023	1025.923	1036.397
6	1010.248	1011.541	1018.602	1017.932	1018.769	1019.256	1026.633	1021.665	1036.022
7	1014.967	1011.072	1020.088	1017.316	1016.905	1018.490	1026.716	1021.427	1036.146
8	1013.115	1011.067	1018.463	1016.120	1016.131	1018.205	1026.241	1023.207	1035.343
9	1014.760	1010.279	1018.026	1015.958	1016.090	1017.859	1026.791	1024.885	1034.831
10	1013.666	1011.750	1018.389	1015.770	1016.006	1017.536	1027.021	1025.483	1034.173
11	1013.572	1012.113	1018.275	1016.442	1016.342	1017.986	1027.172	1025.279	1034.127
12	1011.629	1011.877	1018.490	1016.644	1016.981	1018.222	1027.167	1025.321	1034.197
13	1010.580	1011.877	1019.857	1016.577	1017.167	1018.088	1027.533	1024.391	1033.206
14	1010.010	1011.887	1019.065	1016.307	1016.906	1017.430	1026.397	1022.702	1033.321
15	1007.262	1012.132	1018.721	1016.558	1017.488	1017.180	1026.265	1020.854	1034.098
16	1008.794	1012.102	1017.232	1017.584	1017.689	1017.932	1025.840	1023.104	1034.223
17	1010.408	1012.217	1017.370	1016.527	1017.405	1019.620	1026.265	1027.556	1033.891
18	1014.129	1012.964	1018.667	1016.365	1014.810	1019.578	1026.673	1030.739	1033.814
19	1015.225	1012.597	1019.814	1016.899	1014.432	1020.139	1026.818	1032.437	1034.207
20	1015.357	1011.969	1020.130	1016.988	1011.831	1019.905	1025.998	1032.501	1035.025
21	1012.055	1011.810	1019.083	1016.202	1008.237	1019.336	1025.890	1031.792	1034.714
22	1006.484	1012.065	1016.483	1016.524	1001.268	1020.540	1025.601	1032.094	1034.975
23	1007.126	1012.373	1016.146	1015.872	1003.013	1018.795	1026.015	1031.806	1035.906
24	1005.381	1012.174	1016.527	1015.150	1005.929	1017.471	1026.694	1031.374	1036.457
25	1006.273	1011.539	1017.047	1015.459	1009.120	1016.403	1028.265	1033.027	1036.745
26	1008.439	1011.239	1016.946	1015.810	1012.149	1016.069	1028.593	1033.444	1037.520
27	1008.118	1011.529	1017.429	1015.964	1016.676	1015.970	1028.936	1034.936	1037.076
28	1007.739	1011.443	1017.124	1015.289	1018.798	1016.525	1030.129	1035.641	1037.049
29	1007.395	1010.649	1017.277	1015.800	1019.052	1016.468	1030.623	1035.873	1036.726
30	1008.575	1010.795	1016.729	1016.135	1018.619	1016.845	1030.082	1035.456	1036.706
31		1010.933		1017.722	1019.084	1017.036	1029.654	1035.769	1036.706

**Table 4.7 ERBS WFOV Shortwave In-Flight
Count Conversion Coefficients**

APPLICABLE PERIOD	A_V	A_E	A_F	A_R
11/01/84 – 11/30/84	–25.5824	–0.03051	–0.6434	26.5454
01/01/85 – 01/31/85	–25.6867	–0.03064	–0.6460	26.6537
04/01/85 – 04/30/85	–25.7758	–0.03074	–0.6482	26.7461
07/01/85 – 07/31/85	–25.9090	–0.03090	–0.6516	26.8844
08/01/85 – 08/31/85	–25.9663	–0.03097	–0.6530	26.9438
10/01/85 – 10/31/85	–26.0224	–0.03104	–0.6544	27.0020
01/01/86 – 01/31/86	–26.1480	–0.03119	–0.6576	27.1323
12/01/86 – 12/31/86	–26.4821	–0.03159	–0.6660	27.4790
01/01/87 – 01/31/87	–26.5086	–0.03162	–0.6666	27.5065

Table 4.7 (Continued)
ERBS WFOV Shortwave In-Flight Offsets, B_{EDMT}

DATE	NOV 84	JAN 85	APRIL 85	JULY 85	AUG 85	OCT 85	JAN 86	DEC 86	JAN 87
1	1304.592	1305.410	1311.386	1316.677	1319.660	1323.421	1330.460	1347.622	1351.197
2	0000.000	1306.281	1311.064	1317.000	1320.111	1323.458	1330.417	1347.903	1351.076
3	0000.000	1306.863	1310.654	1317.136	1320.300	1322.920	1330.477	1348.473	1351.131
4	0000.000	1306.778	1310.489	1317.259	1320.150	1322.595	1330.554	1348.516	1351.272
5	1303.967	1306.558	1310.196	1316.939	1320.029	1322.168	1330.428	1348.516	1351.094
6	1304.012	1305.943	1309.943	1316.818	1319.733	1322.028	1329.713	1348.516	1351.152
7	1303.830	1305.729	1309.733	1316.047	1318.684	1321.948	1329.405	1348.516	1351.214
8	1303.737	1305.765	1309.599	1315.959	1318.131	1321.681	1329.171	1348.516	1350.727
9	1303.592	1305.815	1309.486	1315.932	1317.955	1321.371	1329.066	1348.516	1350.725
10	1303.336	1305.931	1309.319	1315.964	1318.023	1321.287	1329.055	1348.516	1350.659
11	1303.085	1306.079	1309.129	1316.333	1318.184	1321.228	1329.153	1348.516	1350.474
12	1302.592	1306.184	1308.900	1316.409	1318.431	1320.978	1329.186	1348.516	1350.312
13	1302.952	1306.345	1308.745	1316.440	1318.617	1320.776	1329.446	1348.516	1350.313
14	1302.715	1306.486	1308.405	1316.481	1318.833	1320.591	1329.421	1348.516	1350.397
15	1302.503	1306.604	1308.297	1316.539	1318.953	1320.815	1329.645	1348.516	1350.399
16	1302.182	1306.476	1308.461	1316.681	1319.068	1321.170	1329.698	1348.516	1350.365
17	1302.025	1306.378	1308.812	1316.740	1319.332	1322.047	1329.594	1348.516	1350.286
18	1302.031	1306.277	1309.391	1316.748	1319.412	1322.435	1329.576	1348.279	1350.083
19	1302.266	1306.332	1309.924	1316.735	1319.450	1323.161	1329.249	1348.318	1350.123
20	1302.518	1306.157	1310.079	1316.624	1319.430	1322.890	1329.072	1348.051	1350.300
21	1302.393	1305.978	1309.968	1316.475	1319.439	1322.968	1328.941	1347.929	1350.251
22	1301.998	1305.638	1309.165	1316.254	1319.439	1323.116	1328.710	1347.616	1350.568
23	1301.595	1305.720	1308.830	1316.060	1319.439	1322.593	1328.702	1347.611	1350.454
24	1301.380	1305.559	1309.006	1315.835	1319.439	1322.022	1328.881	1347.636	1350.803
25	1301.326	1305.446	1309.252	1315.883	1319.439	1321.904	1329.149	1348.316	1350.885
26	1301.830	1305.071	1309.456	1315.648	1319.439	1321.475	1329.251	1348.695	1350.747
27	1301.941	1305.006	1309.601	1315.411	1319.439	1321.249	1329.559	1349.031	1350.692
28	1302.078	1304.838	1309.832	1315.276	1318.879	1321.641	1330.097	1349.164	1350.718
29	1302.208	1304.969	1309.880	1315.276	1318.755	1321.832	1330.168	1349.226	1350.715
30	1302.196	1305.019	1309.920	1315.731	1318.783	1321.932	1330.069	1349.130	1350.922
31		1305.244		1316.258	1318.568	1322.240	1330.163	1349.352	1350.727

conversion coefficients respectively. Offsets for shortwave channels are determined using the darkside data.

4.5.2 NOAA-9 Nonscanner Results.

In-flight count conversion coefficients for MFOVT channel are given in Table 4.8. This channel is found to be drifting in quadratic equation form. Therefore, the offset, B_{EDMT} , is determined for every day. However, WFOVT channel, displayed in Table 4.9, seems very constant over the month period.

Further, in-flight count conversion coefficients for MFOV and WFOV shortwave channels are tabulated in Tables 4.10 and 4.11, respectively. The dome's transmissivity of the WFOVSW channel has decreased approximately 2% in one year while, the MFOVSW channel has not degraded significantly. Offset terms of the shortwave channel are determined for everyday using the darkside data.

4.5.3 NOAA-10 Nonscanner Results.

Tables 4.12 and 4.13 display the in-flight count conversion coefficients for MFOVT and WFOVT channels, respectively. These coefficients will remain unchanged except for the offset term B_{EDMT} . The offset terms are determined using the in-flight internal calibration blackbody (IBB) data.

Further, Tables 4.14 and 4.15 detail the in-flight count conversion coefficients for the shortwave channels. These coefficients vary depending on the dome's transmissivity determined from the solar measurements data. Note that the change in the dome's transmissivity for the MFOVSW channel is negligible in comparison to the WFOVSW channel, which has degraded almost 4.5% in one year.

The MFOVSW offset term is determined by analyzing darkside data, while the WFOVSW's offset term is computed using SWICS lamps-off data. The offset term for MFOVSW for December 1986 is the average of two darkside data points, i.e., December 10, 1986 and December 24, 1986. It is important to note that there is no darkside observed by the

**Table 4.8 NOAA-9 MFOV Total In-Flight
Count Conversion Coefficients**

A_V	A_F	A_R
-22.5566	-0.5274	23.9133

NOAA-9 MFOV Total Channel In-Flight Offsets, B_{EDMT}

DATE	APRIL 85	JULY 85	OCT 85	JAN 86	DEC 86	JAN 87
1	1211.54	1195.89	1180.98	1166.99	1123.93	1120.55
2	1211.36	1195.72	1180.82	1166.84	1123.82	1120.44
3	1211.18	1195.55	1180.66	1166.69	1123.71	1120.33
4	1211.01	1195.38	1180.51	1166.55	1123.60	1120.22
5	1210.83	1195.22	1180.35	1166.40	1123.48	1120.12
6	1210.65	1195.05	1180.19	1166.25	1123.37	1120.01
7	1210.48	1194.89	1180.04	1166.11	1123.26	1119.90
8	1210.30	1194.72	1179.88	1165.96	1123.15	1119.80
9	1210.13	1194.55	1179.72	1165.81	1123.04	1119.69
10	1209.95	1194.43	1179.57	1165.67	1122.93	1119.58
11	1209.77	1194.22	1179.41	1165.52	1122.82	1119.48
12	1209.60	1194.05	1179.25	1165.37	1122.71	1119.37
13	1209.42	1193.89	1179.10	1165.23	1122.61	1119.26
14	1209.25	1193.72	1178.94	1165.08	1122.50	1119.16
15	1209.07	1193.56	1178.79	1164.94	1122.39	1119.05
16	1208.90	1193.39	1178.63	1164.79	1122.28	1118.95
17	1208.72	1193.23	1178.48	1164.65	1122.17	1118.84
18	1208.55	1193.06	1178.32	1164.50	1122.06	1118.73
19	1208.37	1192.90	1178.17	1164.36	1121.95	1118.63
20	1208.20	1192.73	1178.01	1164.21	1121.84	1118.52
21	1208.02	1192.57	1177.86	1164.07	1121.73	1118.42
22	1207.85	1192.40	1177.70	1163.92	1121.62	1118.31
23	1207.67	1192.24	1177.55	1163.78	1121.52	1118.21
24	1207.50	1192.07	1177.39	1163.63	1121.41	1118.10
25	1207.32	1191.91	1177.24	1163.49	1121.30	1118.00
26	1207.15	1191.74	1177.08	1163.34	1121.19	1117.89
27	1206.97	1191.58	1176.93	1163.20	1121.08	1117.79
28	1206.80	1191.41	1176.77	1163.05	1120.98	1117.68
29	1206.63	1191.25	1176.62	1162.91	1120.87	1117.58
30	1206.45	1191.09	1176.47	1162.77	1120.76	1117.48
31		1190.92	1176.31	1162.62	1120.65	1117.37

**Table 4.9 NOAA-9 WFOV Total In-Flight
Count Conversion Coefficients**

A_V	A_F	A_R
-22.8621	-0.3977	24.7635

APPLICABLE PERIOD	B_{EDMT}
04/01/85 – 04/30/85	1475.43
07/01/85 – 07/31/85	1475.97
10/01/85 – 10/31/85	1477.63
01/01/86 – 01/31/86	1479.35
12/01/86 – 12/31/86	1482.41
01/01/87 – 01/31/87	1482.41

**Table 4.10 NOAA-9 MFOV Shortwave In-Flight
Count Conversion Coefficients**

APPLICABLE PERIOD	A_V	A_E	A_F	A_R
04/01/85 – 04/30/85	–25.4599	–0.03604	0.7092	28.9870
07/01/85 – 07/31/85	–25.4737	–0.03606	0.7096	29.0027
10/01/85 – 10/31/85	–25.4877	–0.03608	0.7100	29.0186
01/01/86 – 01/31/86	–25.5015	–0.03610	0.7104	29.0344
12/01/86 – 12/31/86	–25.5513	–0.03617	0.7118	29.0911
01/01/87 – 01/31/87	–25.5559	–0.03618	0.7119	29.0963

Table 4.10 (Continued) NOAA-9 MFOV Shortwave In-Flight Offsets, B_{EDMT}

DATE	APRIL 85	JULY 85	OCT 85	JAN 86	DEC 86	JAN 87
1	841.703	842.784	846.971	847.169	852.443	853.044
2	841.578	842.788	847.855	847.273	852.482	853.051
3	841.985	842.598	846.868	847.408	852.529	853.223
4	840.702	842.740	846.797	847.371	852.505	853.114
5	840.763	842.768	846.728	847.440	852.564	853.109
6	840.742	842.729	846.812	847.407	852.574	853.116
7	840.845	842.805	846.880	847.432	852.578	853.116
8	840.972	842.739	846.698	847.430	852.623	853.116
9	840.907	842.857	846.857	847.433	852.468	853.116
10	840.928	842.333	847.356	847.611	853.021	853.116
11	840.951	840.883	846.964	847.690	852.929	853.116
12	840.888	840.941	846.914	847.684	852.909	853.116
13	841.147	840.970	847.124	847.696	852.902	853.116
14	841.173	841.135	847.089	847.738	853.000	853.116
15	841.092	841.038	847.076	847.797	853.028	853.116
16	841.013	841.055	847.309	847.852	852.995	853.116
17	840.963	841.104	845.880	847.878	852.996	853.116
18	841.063	841.141	846.040	847.888	853.082	853.116
19	841.078	841.177	845.963	847.848	853.069	853.116
20	841.143	841.260	846.066	847.901	853.024	852.925
21	841.195	841.338	846.179	847.921	853.104	853.347
22	841.179	841.337	846.168	848.402	853.107	853.116
23	841.160	841.405	846.228	847.873	853.097	853.116
24	841.338	843.234	846.276	847.913	853.276	853.116
25	841.155	845.545	846.209	847.845	852.787	853.116
26	841.146	845.501	846.353	847.911	852.792	853.116
27	841.179	845.540	846.330	847.682	852.850	853.116
28	841.206	845.507	846.307	847.609	852.862	853.116
29	841.370	845.590	846.803	847.616	852.837	853.116
30	841.356	845.456	847.298	847.575	852.916	853.116
31		845.366	846.279	847.555	852.883	853.116

**Table 4.11 NOAA-9 WFOV Shortwave In-Flight
Count Conversion Coefficients**

APPLICABLE PERIOD	A_V	A_E	A_F	A_R
04/01/85 – 04/30/85	–25.9880	–0.03465	–0.3540	30.1311
07/01/85 – 07/31/85	–26.1503	–0.03487	–0.3562	30.3192
10/01/85 – 10/31/85	–26.3053	–0.03507	–0.3583	30.4989
01/01/86 – 01/31/86	–26.4511	–0.03527	–0.3603	30.6680
12/01/86 – 12/31/86	–26.8980	–0.03586	–0.3664	31.1862
01/01/87 – 01/31/87	–26.9326	–0.03591	–0.3668	31.2263

Table 4.11 NOAA-9 (Continued) WFOV Shortwave In-Flight Offsets, B_{EDMT}

DATE	APRIL 85	JULY 85	OCT 85	JAN 86	DEC 86	JAN 87
1	1359.474	1367.569	1377.714	1384.154	1411.863	1414.768
2	1359.412	1367.608	1378.496	1383.891	1411.955	1414.838
3	1359.929	1367.732	1378.206	1384.099	1411.962	1414.842
4	1359.866	1367.705	1378.113	1384.285	1412.124	1414.845
5	1359.729	1367.684	1378.366	1384.401	1412.117	1414.856
6	1359.764	1367.674	1378.440	1384.290	1412.049	1414.946
7	1359.952	1367.619	1378.380	1384.293	1412.140	1414.946
8	1359.754	1367.678	1378.797	1384.203	1412.212	1414.946
9	1359.744	1367.559	1378.278	1384.347	1412.558	1414.946
10	1359.678	1366.908	1378.513	1384.555	1412.992	1414.946
11	1359.561	1366.032	1378.397	1384.380	1412.910	1414.946
12	1359.445	1366.063	1378.503	1384.261	1412.938	1414.946
13	1359.656	1366.182	1378.467	1384.332	1412.999	1414.946
14	1359.555	1366.337	1378.383	1384.426	1413.079	1414.946
15	1359.589	1366.178	1378.543	1384.550	1413.133	1414.946
16	1359.577	1366.129	1377.781	1384.658	1413.284	1414.946
17	1359.644	1366.102	1375.950	1384.565	1413.169	1414.946
18	1359.411	1366.091	1375.896	1384.537	1413.603	1414.946
19	1359.446	1366.080	1375.849	1384.395	1413.362	1414.946
20	1359.563	1366.208	1375.897	1384.415	1413.250	1415.093
21	1359.642	1365.966	1375.726	1384.555	1413.212	1415.378
22	1359.418	1366.132	1376.032	1384.866	1413.336	1414.946
23	1359.565	1366.245	1375.848	1384.443	1413.429	1414.946
24	1359.500	1367.928	1375.926	1384.338	1413.526	1414.946
25	1359.571	1370.306	1375.951	1384.342	1412.976	1414.946
26	1359.906	1370.318	1376.059	1384.407	1412.875	1414.946
27	1360.047	1370.283	1376.133	1384.411	1412.891	1414.946
28	1360.003	1370.278	1376.207	1384.347	1412.967	1414.946
29	1359.971	1370.490	1376.519	1384.337	1412.842	1414.946
30	1359.853	1370.481	1376.830	1384.470	1412.842	1414.946
31		1370.577	1376.145	1384.494	1412.850	1414.946

**Table 4.12 NOAA-10 MFOV Total In-Flight
Count Conversion Coefficients**

A_V	A_F	A_R
-23.2215	-1.9825	22.4009

APPLICABLE PERIOD	B_{EDMT}
12/01/86 – 12/31/86	1668.74
01/01/87 – 01/31/87	1669.70

**Table 4.13 NOAA-10 WFOV Total In-Flight
Count Conversion Coefficients**

A_V	A_F	A_R
-22.5230	-0.4216	23.8202

APPLICABLE PERIOD	B_{EDMT}
12/01/86 – 12/31/86	1432.85
01/01/87 – 01/31/87	1432.85

**Table 4.14 NOAA-10 MFOV Shortwave In-Flight
Count Conversion Coefficients**

APPLICABLE PERIOD	A_V	A_E	A_F	A_R	B_{EDMT}
12/01/86 – 12/31/86	-25.0633	-0.02270	-3.3751	29.1677	1942.58
01/01/87 – 01/31/87	-25.0609	-0.02270	-3.3748	29.1649	1940.10

**Table 4.15 NOAA-10 WFOV Shortwave In-Flight
Count Conversion Coefficients**

APPLICABLE PERIOD	A_V	A_E	A_F	A_R	B_{EDMT}
12/01/86 – 12/31/86	-24.3501	-0.03032	-1.3074	28.6683	1417.18
01/01/87 – 01/31/87	-24.4643	-0.03047	-1.3135	28.8028	1422.56

WFOVSW channel during December 1986 and January 1987.

REFERENCES

1. Barkstrom B. R. and J. B. Hall, Jr., "Earth Radiation Budget Experiment (ERBE): An Overview," *J. Energy*, Vol. 6, pp. 141-146, 1982.
2. Barkstrom, B. R., "The Earth Radiation Budget Experiment (ERBE)," *Bulletin of the American Meteorological Society*, Vol. 65, pp. 1170-1185, 1984.
3. Carman, S. I., "ERBE Nonscanner Instrument Operations Manual," No. D04608A, September 8, 1982.
4. Lee, R. B., III, B. R. Barkstrom and R. D. Cess, "Characteristics of the Earth Radiation Budget Experiment Solar Monitors," *App. Opt.*, Vol. 26, pp. 3090-3096, 1987.
5. Castineiras, A., "Final Calibration Report on ERBE Flight Model One Nonscanner Instrument," No. D06904, August 15, 1984.
6. Castineiras, A., "Final Calibration Report on ERBE Flight Model Two Nonscanner Instrument," No. D06906, October 19, 1984.
7. Castineiras, A., "Final Calibration Report on ERBE Protoflight Model Nonscanner Instrument," No. D06908, December 20, 1984.
8. Halyo, N., S. H. Choi, D. A. Chrisman, Jr. and R. W. Samms, "Development of Response Models for the Earth Radiation Budget Experiment (ERBE) Sensors: Part I - Dynamic Models and Computer Simulations for the ERBE Nonscanner, Scanner and Solar Monitor Sensors," NASA CR-178292, March 20, 1987.
9. Halyo, N. and S. H. Choi, "Development of Response Models for the Earth Radiation Budget Experiment (ERBE) Sensors: Part IV - Preliminary Nonscanner Models and Count Conversion Algorithms," NASA CR-178295, March 20, 1987.
10. Halyo, N. and D. B. Taylor, "Explicit Solution of the Spectral Radiance in Integrating Spheres with Application to the Earth Radiation Budget Experiment Ground Calibration," *J. Opt. Soc. Am. A*, Vol. 5, pp. 520-534, 1988.

APPENDIX A

Configuration Factor

The configuration factor, f , is required by Eq. (4.1) to obtain the in-flight count conversion coefficients. This factor depends on the geometry of the field-of-view limiter (FOVL) and the primary aperture. With known radius of FOVL and primary aperture, one can compute f using the well known equation given below.

$$f = \frac{1}{2} \left[x - \sqrt{x^2 - \frac{4 R_2^2}{R_1^2}} \right]$$

where

$$\begin{aligned} R_1 &= \frac{r_1}{h} \\ R_2 &= \frac{r_2}{h} \\ x &= 1 + \frac{1 + R_1^2}{R_2^2} \end{aligned}$$

r_1 and r_2 are radius and h is the gap between two discs as shown in Fig. A.1.

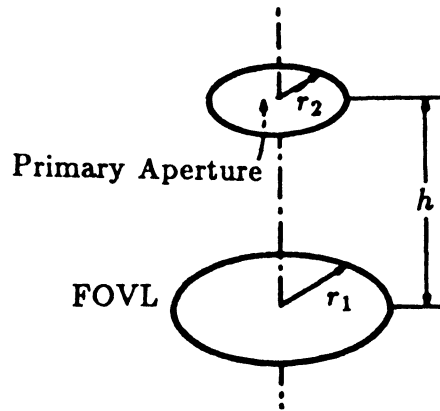


Figure A.1 Representation of Configuration

Table A.1 displays the configuration factor, f for each nonscanner sensor used in this work. ERBS nonscanner configuration factors are found in agreement with TRW's results reported in [5], except for the WFOVT channel. The configuration factor for ERBS WFOVT channel is computed by taking non-cosine response function into account. The configuration factors for NOAA-9 and NOAA-10 for nonscanner sensors, given in Table A.1 are computed using the design data given in [3]. Note that the present results are not in agreement with TRW's configuration factors reported in [6] - [7]. The author has not been able to locate the data points used by TRW for NOAA-9 and NOAA-10. Furthermore, the configuration factors for NOAA-9 and NOAA-10 given in Table A.1, were reproduced by several independent investigators.

Table A.1 Configuration Factors

SENSORS	ERBS	NOAA-9	NOAA-10
MFOVT	0.4240	0.2387	0.2387
WFOVT	0.8692	0.8288	0.8288
MFOVSW	0.4240	0.2387	0.2387
WFOVSW	0.8797	0.8288	0.8288

APPENDIX B

$B_{MRBB-IBB}$ Correction Factor

This factor is required to determine the final in-flight offset term, B_{EDMT} , for total channels. This factor is based on the assumption that the count conversion coefficients may have drifted. To determine a correct offset term for the in-flight IBB source, a $B_{MRBB-IBB}$ factor was determined using the ground IBB data with ground count conversion coefficients based on MRBB data. Table B.1 displays the $B_{MRBB-IBB}$ correction factor for each nonscanner sensor. Note that the correction factor for NOAA-9 MFOVT channel is determined after performing error budget analysis and scanner-nonscanner intercomparisons (a technique developed by the inversion group) at satellite altitude. Also note that the correction factor for NOAA-10 WFOVT is negative. At this point the actual cause of this negative value is unknown, but it is worth mentioning that the NOAA-10 WFOVT channel was replaced by another WFOVT channel prior to launch. In the future more scanner-nonscanner intercomparisons at satellite altitude may answer such questions.

Table B.1 $B_{MRBB-IBB}$ Correction Factors

SENSORS	ERBS	NOAA-9	NOAA-10
MFOVT	5.010	20.444	11.664
WFOVT	5.187	4.796	-4.349

APPENDIX C

Solar Calibration Data

Solar calibration data are used to determine the degradation factor, DF which is required to upgrade the in-flight count conversion coefficients for shortwave channels. Data for ERBS, NOAA-9 and NOAA-10 Shortwave sensors are given below.

Table C.1 ERBS MFOVSW Solar Calibration Data

SAMPLE	CALIBRATION DATE	X(DAY)	SOLAR MEASUREMENTS
1	10/25/84	299.	1363.80000
2	10/26/84	300.	1362.50000
3	10/29/84	303.	1364.60000
4	11/01/84	306.	1363.50000
5	11/05/84	310.	1364.90000
6	11/12/84	317.	1365.00000
7	11/20/84	325.	1364.70000
8	11/26/84	331.	1363.20000
9	12/03/84	338.	1365.80000
10	12/10/84	345.	1364.00000
11	12/17/84	352.	1364.40000
12	12/28/84	363.	1364.30000
13	01/23/85	389.	1361.70000
14	02/06/85	403.	1364.30000
15	02/20/85	417.	1363.20000
16	03/06/85	431.	1364.60000
17	03/20/85	445.	1361.60000
18	04/03/85	459.	1363.20000
19	04/17/85	473.	1362.60000
20	05/01/85	487.	1363.10000
21	05/08/85	494.	1360.40000
22	05/29/85	515.	1361.80000
23	06/26/85	543.	1362.10000
24	07/10/85	557.	1361.60000
25	07/24/85	571.	1362.10000
26	08/07/85	585.	1362.80000
27	08/21/85	599.	1362.90000
28	09/04/85	613.	1359.50000
29	09/18/85	627.	1360.60000
30	10/02/85	641.	1360.50000
31	10/16/85	655.	1361.00000
32	10/31/85	670.	1360.40000
33	11/13/85	683.	1360.40000
34	11/27/85	697.	1359.00000
35	12/18/85	718.	1359.90000
36	12/25/85	725.	1361.40000
37	01/07/86	738.	1360.70000
38	01/22/86	753.	1359.40000
39	02/05/86	767.	1359.50000
40	03/05/86	795.	1362.30000
41	03/19/86	809.	1361.20000
42	04/02/86	823.	1360.80000
43	04/16/86	837.	1360.70000
44	04/30/86	851.	1359.30000
45	05/14/86	865.	1358.70000
46	05/28/86	879.	1359.50000
47	06/04/86	886.	1358.50000
48	06/19/86	901.	1359.30000
49	06/25/86	907.	1359.90000
50	07/09/86	921.	1358.60000
51	07/23/86	935.	1358.60000
52	08/17/86	960.	1359.70000
53	09/03/86	977.	1358.90000
54	09/17/86	991.	1357.30000
55	10/01/86	1005.	1358.90000
56	10/15/86	1019.	1358.50000
57	10/29/86	1033.	1359.60000
58	11/12/86	1047.	1359.50000
59	11/26/86	1061.	1358.00000
60	12/24/86	1089.	1355.70000
61	01/07/87	1103.	1358.90000

Table C.2 ERBS WFOVSW Solar Calibration Data

SAMPLE	CALIBRATION DATE	X(DAY)	SOLAR MEASUREMENTS
1	10/25/84	299.	1364.30000
2	10/26/84	300.	1363.20000
3	10/29/84	303.	1363.20000
4	11/01/84	306.	1362.80000
5	11/05/84	310.	1362.20000
6	11/12/84	317.	1362.30000
7	11/20/84	325.	1361.70000
8	11/26/84	331.	1359.30000
9	12/03/84	338.	1358.90000
10	12/10/84	345.	1357.50000
11	12/17/84	352.	1356.20000
12	12/28/84	363.	1356.80000
13	01/23/85	389.	1355.20000
14	02/06/85	403.	1354.20000
15	02/20/85	417.	1351.40000
16	03/06/85	431.	1351.80000
17	03/20/85	445.	1352.10000
18	04/03/85	459.	1349.40000
19	04/17/85	473.	1350.40000
20	05/01/85	487.	1349.00000
21	05/08/85	494.	1347.90000
22	05/29/85	515.	1348.20000
23	06/26/85	543.	1345.70000
24	07/10/85	557.	1344.70000
25	07/24/85	571.	1344.50000
26	08/07/85	585.	1344.80000
27	08/21/85	599.	1343.60000
28	09/04/85	613.	1339.10000
29	09/18/85	627.	1340.20000
30	10/02/85	641.	1338.00000
31	10/16/85	655.	1338.40000
32	10/31/85	670.	1337.00000
33	11/13/85	683.	1338.30000
34	11/27/85	697.	1335.20000
35	12/18/85	718.	1333.20000
36	12/25/85	725.	1334.00000
37	01/07/86	738.	1332.80000
38	01/22/86	753.	1332.10000
39	02/05/86	767.	1331.90000
40	03/05/86	795.	1330.20000
41	03/19/86	809.	1331.30000
42	04/02/86	823.	1327.30000
43	04/16/86	837.	1329.80000
44	04/30/86	851.	1327.70000
45	05/14/86	865.	1326.70000
46	05/28/86	879.	1327.90000
47	06/04/86	886.	1326.80000
48	06/19/86	901.	1325.90000
49	06/25/86	907.	1326.20000
50	07/09/86	921.	1323.00000
51	07/23/86	935.	1323.40000
52	08/17/86	960.	1323.30000
53	09/03/86	977.	1321.40000
54	09/17/86	991.	1320.20000
55	10/01/86	1005.	1320.00000
56	10/15/86	1019.	1318.10000
57	10/29/86	1033.	1319.70000
58	11/12/86	1047.	1318.90000
59	11/26/86	1061.	1316.90000
60	12/24/86	1089.	1314.40000
61	01/07/87	1103.	1316.00000

Table C.3 NOAA-9 MFOVSW Solar Calibration Data

SAMPLE	CALIBRATION DATE	X(DAY)	SOLAR MEASUREMENTS
1	01/23/85	389.	1363.20000
2	01/25/85	391.	1365.60000
3	01/27/85	393.	1362.80000
4	01/30/85	396.	1362.40000
5	02/06/85	403.	1365.60000
6	02/13/85	410.	1365.80000
7	02/20/85	417.	1365.40000
8	03/06/85	431.	1365.40000
9	03/20/85	445.	1364.50000
10	04/03/85	459.	1364.90000
11	04/17/85	473.	1364.70000
12	05/08/85	494.	1362.50000
13	05/29/85	515.	1365.20000
14	06/12/85	529.	1361.10000
15	06/26/85	543.	1363.90000
16	07/10/85	557.	1362.20000
17	07/24/85	571.	1364.50000
18	08/07/85	585.	1362.40000
19	08/21/85	599.	1362.80000
20	09/04/85	613.	1362.10000
21	09/18/85	627.	1364.00000
22	10/02/85	641.	1364.00000
23	10/16/85	655.	1362.50000
24	10/30/85	669.	1360.70000
25	11/13/85	683.	1362.00000
26	11/27/85	697.	1361.50000
27	12/11/85	711.	1362.00000
28	01/22/86	753.	1362.10000
29	02/05/86	767.	1360.70000
30	02/19/86	781.	1360.50000
31	03/05/86	795.	1361.90000
32	03/19/86	809.	1361.20000
33	04/02/86	823.	1361.70000
34	04/30/86	851.	1362.70000
35	05/14/86	865.	1360.30000
36	05/28/86	879.	1361.90000
37	06/11/86	893.	1361.60000
38	07/09/86	921.	1360.10000
39	07/23/86	935.	1361.10000
40	08/06/86	949.	1359.00000
41	08/20/86	963.	1360.40000
42	09/03/86	977.	1360.50000
43	09/17/86	991.	1359.50000
44	10/15/86	1019.	1359.50000
45	10/29/86	1033.	1358.90000
46	11/12/86	1047.	1358.70000
47	11/26/86	1061.	1359.80000
48	01/21/87	1117.	1359.40000

Table C.4 NOAA-9 WFOVSW Solar Calibration Data

SAMPLE	CALIBRATION DATE	X(DAY)	SOLAR MEASUREMENTS
1	01/23/85	389.	1364.20000
2	01/25/85	391.	1366.10000
3	01/27/85	393.	1363.80000
4	01/30/85	396.	1362.60000
5	02/06/85	403.	1363.20000
6	02/13/85	410.	1363.10000
7	02/20/85	417.	1362.10000
8	03/06/85	431.	1361.80000
9	03/20/85	445.	1359.50000
10	04/03/85	459.	1357.60000
11	04/17/85	473.	1357.90000
12	05/08/85	494.	1350.90000
13	05/29/85	515.	1355.50000
14	06/12/85	529.	1345.90000
15	06/26/85	543.	1349.60000
16	07/10/85	557.	1344.20000
17	07/24/85	571.	1349.50000
18	08/07/85	585.	1343.30000
19	08/21/85	599.	1345.20000
20	09/04/85	613.	1343.30000
21	09/18/85	627.	1345.40000
22	10/02/85	641.	1344.80000
23	10/16/85	655.	1339.10000
24	10/30/85	669.	1335.60000
25	11/13/85	683.	1336.30000
26	11/27/85	697.	1333.90000
27	12/11/85	711.	1335.70000
28	01/22/86	753.	1333.40000
29	02/05/86	767.	1331.30000
30	02/19/86	781.	1328.30000
31	03/05/86	795.	1332.30000
32	03/19/86	809.	1329.80000
33	04/02/86	823.	1329.00000
34	04/30/86	851.	1330.40000
35	05/14/86	865.	1325.30000
36	05/28/86	879.	1325.30000
37	06/11/86	893.	1325.50000
38	07/09/86	921.	1322.70000
39	07/23/86	935.	1321.30000
40	08/06/86	949.	1319.70000
41	08/20/86	963.	1318.80000
42	09/03/86	977.	1317.90000
43	09/17/86	991.	1316.50000
44	10/15/86	1019.	1315.50000
45	10/29/86	1033.	1315.40000
46	11/12/86	1047.	1311.00000
47	11/26/86	1061.	1312.10000
48	01/21/87	1117.	1307.90000

Table C.5 NOAA-10 MFOVSW Solar Calibration Data

SAMPLE	CALIBRATION DATE	X(DAY)	SOLAR MEASUREMENTS
1	10/22/86	1026.	1371.00000
2	10/25/86	1029.	1373.20000
3	10/29/86	1033.	1373.60000
4	11/01/86	1036.	1373.80000
5	11/05/86	1040.	1370.00000
6	11/12/86	1047.	1371.10000
7	11/26/86	1061.	1370.10000
8	12/10/86	1075.	1371.90000
9	12/24/86	1089.	1369.10000
10	01/21/87	1117.	1371.40000
11	02/04/87	1131.	1371.00000
12	02/18/87	1145.	1369.10000
13	03/04/87	1159.	1369.00000
14	03/18/87	1173.	1370.10000
15	04/01/87	1187.	1372.10000
16	04/15/87	1201.	1367.70000
17	04/29/87	1215.	1368.70000
18	08/19/87	1327.	1375.20000
19	09/02/87	1341.	1375.10000
20	09/16/87	1355.	1374.80000
21	09/30/87	1369.	1368.00000
22	10/14/87	1383.	1368.10000
23	10/28/87	1397.	1373.10000
24	11/11/87	1411.	1373.20000
25	11/25/87	1425.	1374.20000
26	12/09/87	1439.	1370.80000
27	12/23/87	1453.	1366.60000
28	01/06/88	1467.	1368.80000
29	01/23/88	1484.	1365.60000
30	02/03/88	1495.	1366.80000

Table C.6 NOAA-10 WFOVSW Solar Calibration Data

SAMPLE	CALIBRATION DATE	X(DAY)	SOLAR MEASUREMENTS
1	10/22/86	1026.	1361.90000
2	10/25/86	1029.	1359.00000
3	10/29/86	1033.	1357.20000
4	11/01/86	1036.	1354.50000
5	11/05/86	1040.	1356.50000
6	11/12/86	1047.	1354.60000
7	11/26/86	1061.	1352.10000
8	12/10/86	1075.	1346.90000
9	12/24/86	1089.	1345.30000
10	01/21/87	1117.	1338.50000
11	02/04/87	1131.	1335.90000
12	02/18/87	1145.	1335.10000
13	03/04/87	1159.	1334.00000
14	03/18/87	1173.	1328.90000
15	04/01/87	1187.	1324.80000
16	04/15/87	1201.	1327.90000
17	04/29/87	1215.	1325.40000
18	08/19/87	1327.	1308.90000
19	09/02/87	1341.	1305.90000
20	09/16/87	1355.	1302.40000
21	09/30/87	1369.	1306.10000
22	10/14/87	1383.	1303.90000
23	10/28/87	1397.	1300.20000
24	11/11/87	1411.	1296.90000
25	11/25/87	1425.	1295.00000
26	12/09/87	1439.	1297.20000
27	12/23/87	1453.	1296.60000
28	01/06/88	1467.	1293.50000
29	01/23/88	1484.	1292.60000
30	02/03/88	1495.	1292.90000

PART II

MODELING AND CHARACTERIZATION OF THE EARTH RADIATION BUDGET EXPERIMENT (ERBE) SCANNER SENSORS

I. INTRODUCTION

The accurate measurement of the total radiative energy flux (radiant exitance) at the top of the atmosphere provides one the most important elements in understanding the various climatic relationships of the earth-atmosphere system. For example, top of the atmosphere measurements of the reflected solar and the emitted radiative energy with high absolute accuracy can validate the actual occurrence of the Greenhouse effect and provide quantitative relationships among increasing levels of atmospheric constituents and the earth's climate. In establishing long-term trends and relationships, the absolute accuracy and stability of the sensors and the interpretation of the sensor output are of critical importance.

This paper describes the calibration and interpretation of the Earth Radiation Budget Experiment (ERBE) scanner sensors. The Earth Radiation Budget Experiment provides measurements of the earth's outgoing radiative flux as seen from the three satellites: ERBS, NOAA-9 and NOAA-10. Each satellite contains two instruments: a narrow field-of-view scanning instrument and a wide field-of-view nonscanning instrument. Each of the NFOV scanning instruments contains three scanner sensors which measure the radiation in three wavelength bands. The shortwave scanner measures the spectral radiance within the band from $0.2\ \mu\text{m}$ to $5.0\ \mu\text{m}$, the longwave scanner the band from $5.0\ \mu\text{m}$ to $50\ \mu\text{m}$ and the total

scanner the band from $0.2\ \mu\text{m}$ to $50\ \mu\text{m}$. Figure 1 shows the ERBE scanner instrument with the contamination covers open.

The ERBS satellite was launched in near-earth-orbit during mission 41-G by the space shuttle Challenger on October 5, 1984. After the required orbital transfer maneuver, ERBS attained its orbit at an altitude near 610 km with an inclination angle 57° . The NOAA-9 and NOAA-10 satellites are both sun-synchronous satellites and have been placed in orbits with an inclination angle of 99° and an altitude near 860 km. NOAA-9 has an equatorial crossing time of 1430 LT for the ascending (northward) node, while NOAA-10 has an equatorial crossing time of 0730 LT producing a three-satellite system with high local time sampling.

The basic objectives of the ERBE are to determine: 1) the monthly average radiation budget on a global, zonal and regional scale, 2) the average diurnal variation of the radiation budget on a regional and monthly scale, and 3) the equator-to-pole transport gradient. A zone is defined to be an area covering 10° ECA, and a region is defined as an area of $250\ \text{km} \times 250\ \text{km}$. A more detailed description of the ERBE objectives can be found in [1], [2].

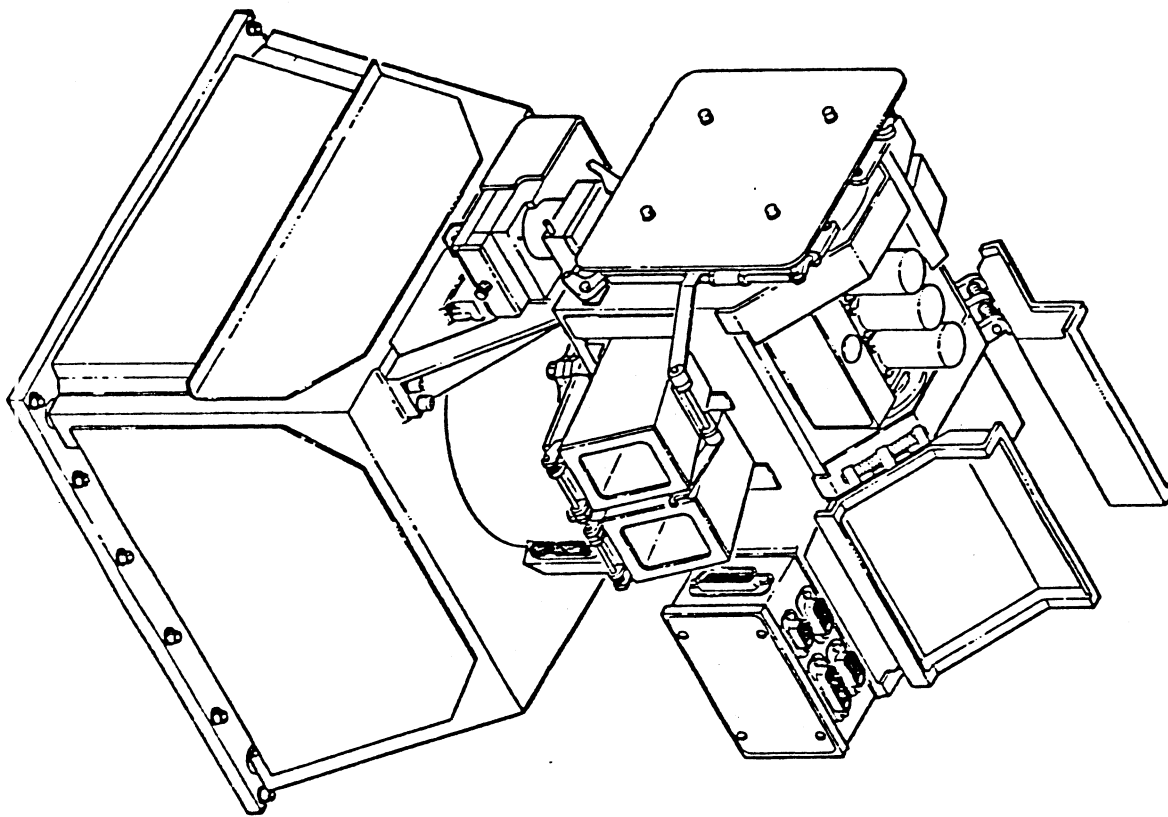


Figure 1. ERBE Scanner with Contamination Covers Open

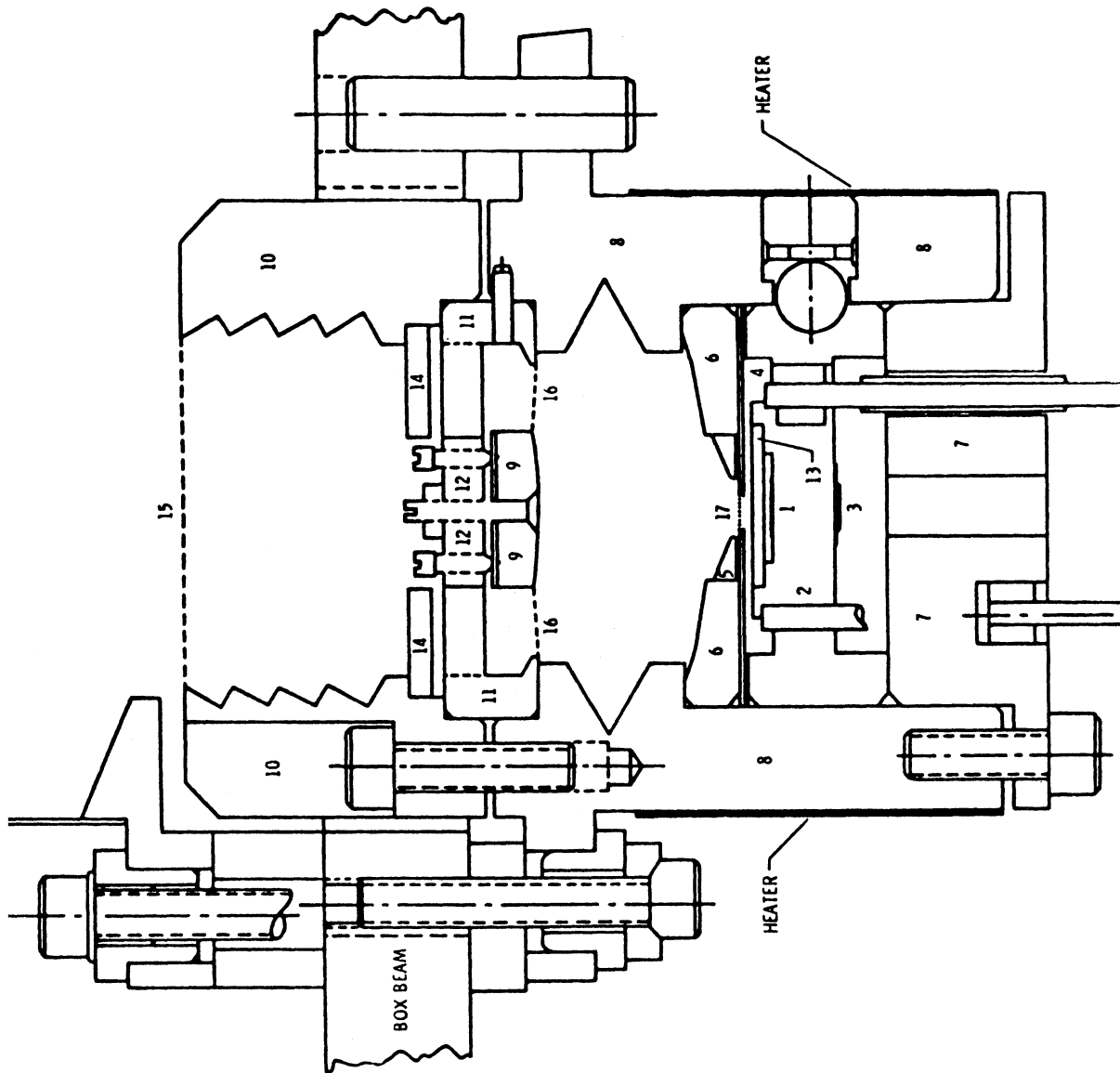
II. SCANNER DESCRIPTION AND MODELING

The ERBE scanner instrument is shown in Fig. 1 with open contamination covers. Figure 2 is a schematic diagram showing the principal components of the scanner. The scanner detectors are thermistor bolometers with an active and reference flake placed in a balanced bridge configuration for accurate detection of small signals.

The normal scanning direction is perpendicular to the satellite ground track. In this cross-track scan mode, the duration of a complete scan is 4 seconds. The scan starts with a space-look beyond the horizon and gradually scans the top-of-the-atmosphere viewing the satellite nadir point and scans past the horizon on the other side of the track, before scanning to a position where the detector sees its corresponding internal calibration source. Then a fast retrace brings the scanner back to its original position beyond the horizon, thus completing a full normal scan, as shown in Fig. 3. Throughout the scan, the A/D converter samples the scanner output voltage every 33 msec. The sampled digital voltage during the space look, when viewing the earth and the internal calibration source is telemetered down to earth and constitutes the scanner's radiometric output; for example, the retrace samples are not transmitted.

The ERBE scanner can also perform a normal scan sequence at any azimuth angle so that the scan direction is no longer in a cross-track direction. In fact, when the azimuth angle is commanded to be 90° , the scan direction is along the satellite ground track. Other scan modes are also available for specific purposes such as solar calibration through the mirror-attenuated-mosaic (MAM).

The ERBE scanners contain significant optical, thermal/radiative and electronic components. The incoming spectral radiance, L_λ , enters the scanner as shown in Fig. 2. The staircase shape of the field-of-view limiter (element 10) is designed to reflect back any radiation arriving from locations outside the desired footprint. The surface of the field-of-view



1. ACTIVE FLAKE
2. HEAT SINK & DETECTOR ASSY.
3. COMPENSATING FLAKE
4. PRECISION APERTURE
5. INSERT, PRIMARY
6. PRIMARY MIRROR
7. CAP ASSEMBLY
8. HOUSING & HEATER
9. SECONDARY MIRROR
10. FOV LIMITER
11. MOUNT, SECONDARY(A)
12. MOUNT, SECONDARY(B)
13. LW OR SW FILTER
14. SW FILTER
15. FICTITIOUS SURFACE AT FOV
16. FICTITIOUS SURFACE AT SECONDARY
17. FICTITIOUS SURFACE AT APERTURE

Figure 2. ERBE Scanner

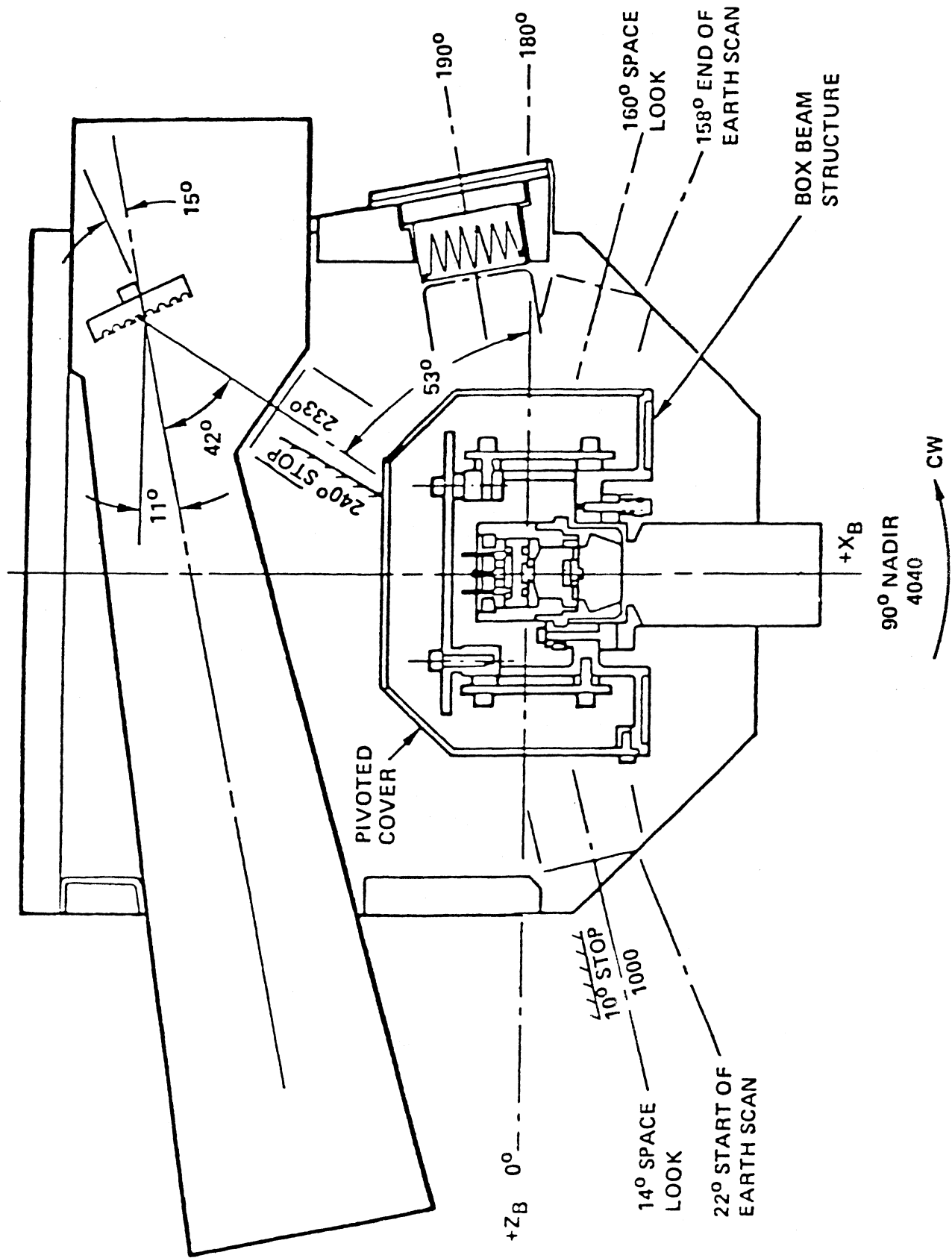


Figure 3. Scan Pattern

limiter is reflective black so that any out-of-field radiation will largely be reflected out of the scanner and some will be absorbed, thus not reach the detector. Since some of the radiation is absorbed, the temperature of the field-of-view limiter itself will vary slightly with the amount of incoming radiation.

For the shortwave sensor, the incoming radiation passes through the shortwave suprasil-W1 filter shown as element 14. A second shortwave filter (element 13) will cut-off any longwave radiation from reaching the detector. However, the first filter (element 14) cuts off longwave radiation before it reaches and heats other surfaces closer to the detector itself. Thus, the purpose of the first shortwave filter is to reduce thermal transients from unduly influencing the detector. The suprasil filter itself absorbs some of the incoming longwave and will vary in temperature. However, the impact will be smaller and will be further reduced by the shortwave filter. The longwave and total channels do not have a filter in element 14.

The remaining radiation falls on the primary mirror, shown as element 6, and is reflected to the secondary mirror, shown as element 9, which reflects the radiation through the primary insert (element 5), the precision aperture (element 4) and through corresponding filters (element 13) according to the sensor onto the active flake (element 1). The primary and secondary mirrors form a Cassegrainian optical system with its focal distance corresponding to the precision aperture. Both primary and secondary mirrors are aluminized optical glass with a protective overcoat.

The precision aperture has a hexagonal configuration as shown in Fig. 4. In the scan direction, the instantaneous field-of-view is 3° , while along the track direction it reaches 4.5° . The hexagonal shape of the aperture was selected to reduce aliasing errors and approximates a diamond aperture shape. A diamond aperture, when coupled with a low-pass electrical filter with a cut-off near the Nyquist frequency, can be shown to reduce aliasing errors in comparison to a circular aperture [3], [4].

The radiation which passes through the precision aperture falls on the active thermis-

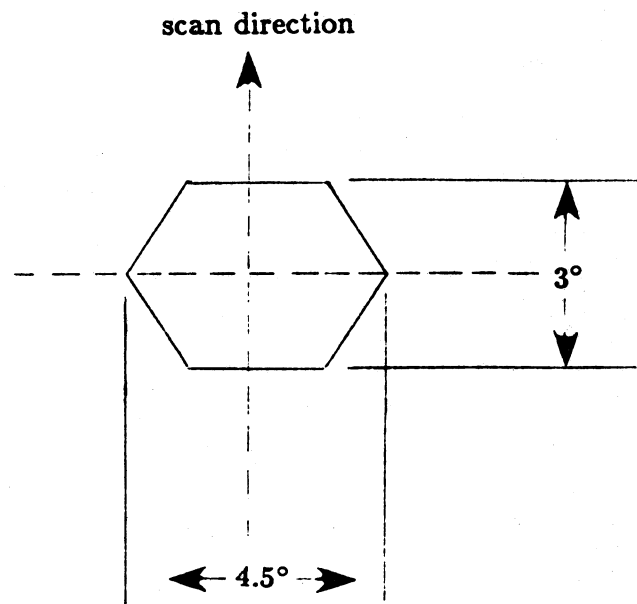


Figure 4. Precision Aperture Shape

tor flake (element 1) after passing through a filter (element 13). For the shortwave channel, the filter is suprasil-W1; the longwave channel has a diamond filter; the total channel has no filters.

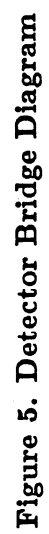
When the incoming radiation is absorbed by the active flake, its temperature rises. The change in temperature produces a corresponding change in the electrical resistivity of the flake. The active and reference flakes (elements 1 and 3) form two of the four legs of a balanced bridge, as shown in Fig. 5. When the temperature, hence resistivity, of the active flake varies, the resistance of the corresponding leg goes out of balance producing a signal proportional to the difference in the active and reference flake resistances. This signal is amplified in preamp and power amplification sections and is processed through a low-pass filter. The filter output is sampled, digitized and is telemetered to earth as the radiometric output of the sensor. Housekeeping data such as the reference flake temperature, T_3 , the detector bridge voltage, V_B , etc. are also telemetered to earth every 4 seconds.

To accommodate drifts in various thermal and electronic parameters, a drift balance mechanism is present, as shown in Fig. 6. When the average space look output voltage exceeds a specified value, the drift balance is activated in a direction to bring the space look readings within the specified margins. Otherwise, the drift balance is inactive. This mechanism maintains the dynamic range of the radiometric output in the presence of drifts.

The detector is in a housing, element 8, which is kept at a constant temperature near 38° C with the help of a heater driven by a PI controller. The heater tries to maintain all the detector components at a constant operating temperature so that the temperature variations in the active flake caused by the incoming radiation are reproduced by the sensor's radiometric output without distortion or error.

A. Spectral Considerations.

Each of the three ERBE scanners are ideally intended to measure the exact shortwave (0.2 μm - 5.0 μm), longwave (5.0 μm - 50.0 μm) or the total (0.2 μm - 50.+ μm) radiance in the incoming radiation, L_λ . However, the spectral properties of the materials used in



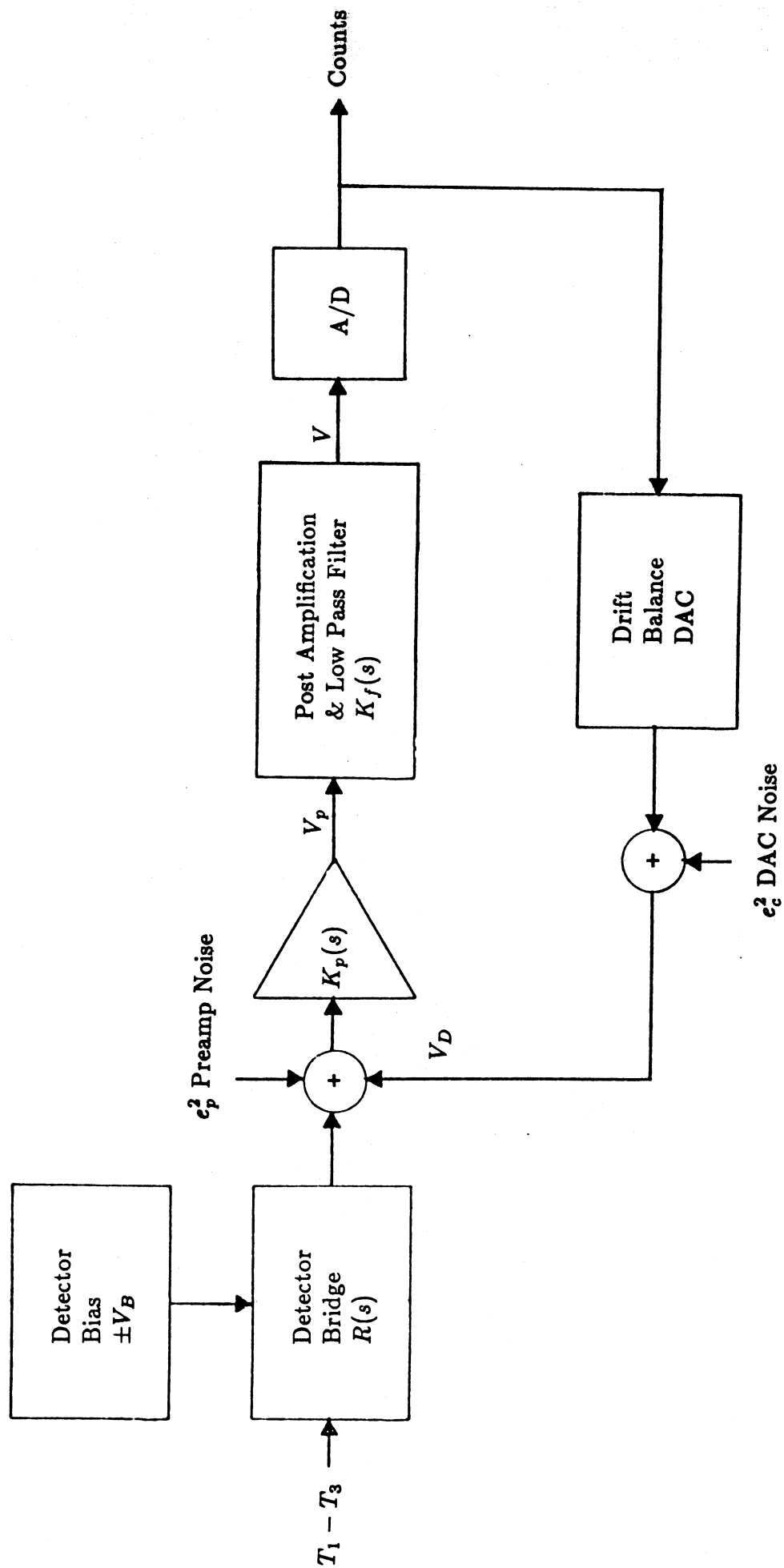


Figure 6. Scanner Electronics Block Diagram

actual sensors produce a spectral response which differs from the ideal spectral response to varying degrees. In the ERBE scanners, non-ideal spectral behavior is largely due to the spectral characteristics of the following elements.

1. Primary and secondary mirror spectral reflectivity,
2. Shortwave and longwave filter transmissivity, and
3. Active thermistor flake spectral absorptivity.

The total channel is influenced only by the first and third factors above. The shortwave channel has two additional suprasil-W1 filters, while the longwave channel has an additional diamond filter. Figures 7, 8 and 9 show plots of the spectral response of the three ERBE scanners. While the essential tendency of each sensor is to measure the spectral radiance in its corresponding spectral band, the actual spectral responses fall somewhat short of the ideal and must be accommodated.

Once absorbed by the active flake, the spectral characteristics of the incoming radiance no longer have any impact on the response of the sensor. Thus, it is useful to think of the sensor, as shown in Fig. 10, of a system with non-ideal spectral characteristics, $\tau(\lambda)$, followed by a system which is independent of spectral characteristics but depends only on thermal and electronic parameters. The input to this spectrally flat system is the portion of the incoming radiation, L_λ , which is absorbed by the active flake, say L_d .

$$L_d = \int_0^\infty \tau(\lambda) L_\lambda d\lambda \quad (1)$$

Whether in viewing calibration sources or in measuring top-of-the-atmosphere (TOA) radiances, the incoming spectral radiance L_λ , is first transformed into absorbed heat at the active flake, L_d , and then transformed into an electrical voltage output as a digital signal. On the other hand, the ideal desired measurements would have been:

$$L^{SW} = \int_{0.2}^5 L_\lambda d\lambda \quad , \quad (2a)$$

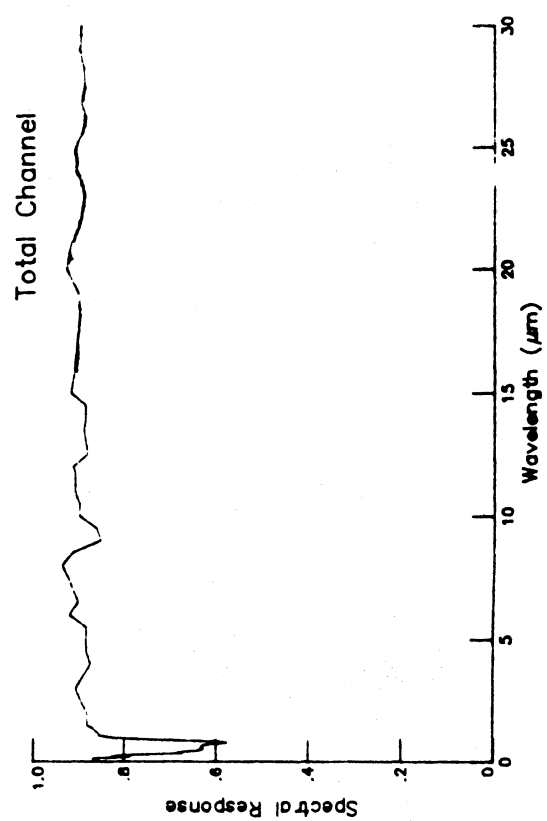


Figure 7. ERBE Scanner Spectral Response

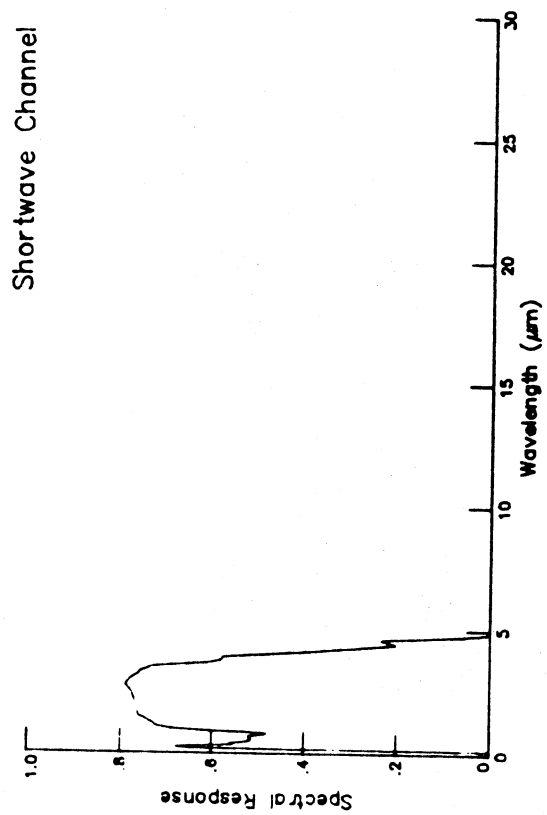


Figure 8. ERBE Scanner Spectral Response

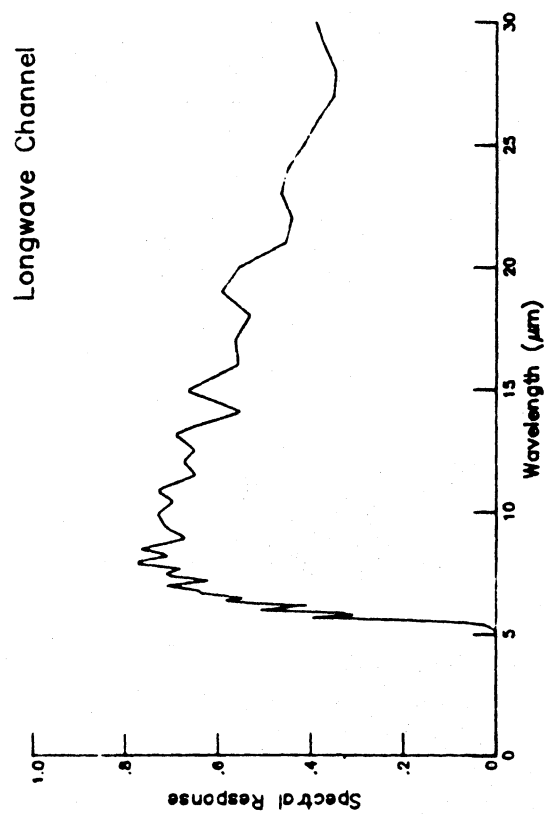
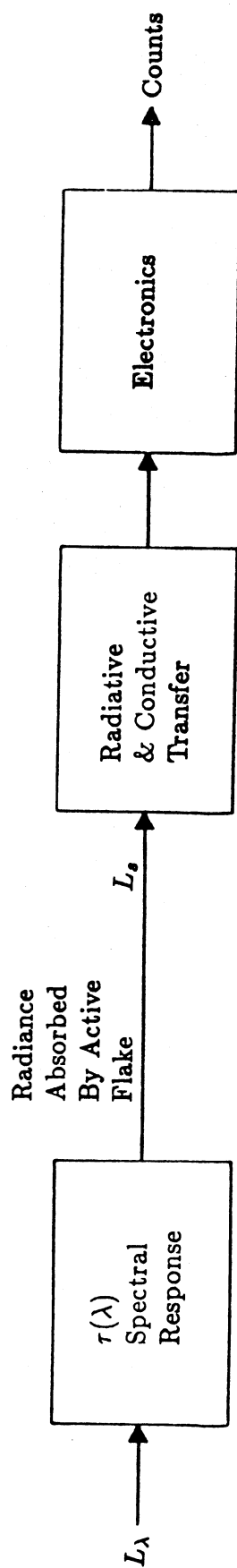


Figure 9. ERBE Scanner Spectral Response



- Spectral Response Due to
- Primary and Secondary Mirror Reflectivity
 - Filter Transmittance
 - Active Flake Absorptivity

$$L_s = \int_0^{\infty} \tau(\lambda) L_{\lambda} d\lambda$$

Figure 10. Spectral Considerations

$$L^{LW} = \int_5^{50} L_\lambda d\lambda \quad , \quad (2b)$$

$$L^T = \int_{0.2}^{50} L_\lambda d\lambda \quad , \quad (2c)$$

for the shortwave, longwave and total channels, respectively.

It is clear that, in general, the shortwave radiance L^{SW} , cannot be determined from just L_d^{SW} for arbitrary incoming radiation, L_λ . However, if L_d^{SW} , L_d^{LW} and L_d^T are known and these values are used to identify the observed scene type, then the incoming spectral radiance can be parametrized and a more accurate estimate of L^{SW} and L^{LW} in terms of L_d^{SW} , L_d^{LW} and L_d^T may be obtained using say a least-squares method. This approach is used in processing the ERBE data.

Thus, the sensor interpretation algorithms produce an estimate of L_d^{SW} , L_d^{LW} and L_d^T from the corresponding sensor radiometric outputs. Then, the "unfiltered" radiances L^{SW} , L^{LW} are estimated by jointly processing these three measurements. In this paper, we will consider the algorithm which produce the estimates of L_d^{SW} , L_d^{LW} and L_d^T . The algorithms used to estimate L^{SW} and L^{LW} will be given in a future paper on the inversion algorithm.

B. Scanner Dynamic Model.

As the radiation entering the scanner makes its way to the active flake, it is reflected from and absorbed by the various surfaces shown in Fig. 2. The absorbed energy raises the temperature of the elements and forms gradients and transients among the various scanner components. For example, as the active thermistor flake absorbs the incoming radiative energy, L_d , its temperature rises and the temperature (hence resistance) differential between the active and reference flakes is detected by a balanced bridge. The expected behavior is that the reference flake temperature remains constant, as it does not see the incoming radiation and is placed in a cavity where the temperature is maintained at a

set constant temperature. However, the reference flake temperature cannot be directly measured. Thus, its actual behavior can only be determined by modeling and simulation.

In conjunction with the thermal and radiative effects, the electrical signal processing also has significant impact on the scanner output. The heater electronics controlling the heat sink temperature has a direct thermal input. Figure 11 shows the transfer function of the heater controller. The heater controller dynamics can then be modeled as

$$\dot{x}_7 = -\frac{1}{\tau_{H1}} x_7 - \frac{K_{H1}}{\tau_{H1}} T_7 + \frac{K_{H1}}{\tau_{H1}} T_s \quad , \quad (3a)$$

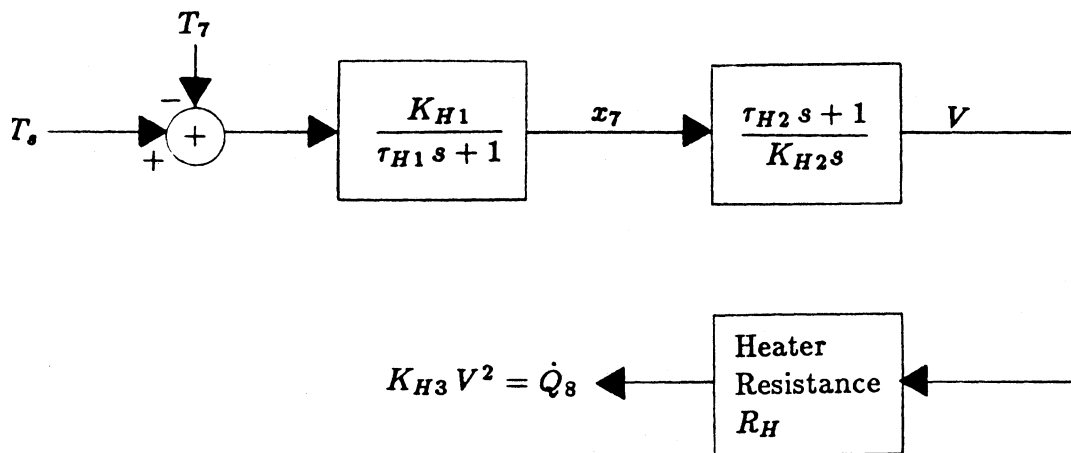
$$\dot{x}_8 = \left(\frac{1}{K_{H2}} - \frac{\tau_{H2}}{K_{H2} \tau_{H1}} \right) x_7 - \frac{K_{H1}}{K_{H2}} \frac{\tau_{H2}}{\tau_{H1}} T_7 + \frac{K_{H1}}{K_{H2}} \frac{\tau_{H2}}{\tau_{H1}} T_s \quad , \quad (3b)$$

$$\dot{Q}_8(x_8) = K_H x_8^2 \quad , \quad (3c)$$

where T_s is the set temperature at which the scanner heat sink is to operate, $\dot{Q}_8(x_8)$ is the Joule heating added to the heat sink to maintain the set temperature.

The signal processing performed by the ERBE scanner electronics is shown in Fig. 6. The bridge, the preamp and the power amplifiers have rather small dynamic effects on the signal, as their cut-off frequencies tend to be much higher than the frequency content of the incoming radiation, L_d . However, the low-pass filter, a four-pole Bessel filter, has a significant effect on the signal as it has a lower cut-off frequency. In fact, the cut-off frequency is much lower than the Nyquist frequency, presumably to reduce noise rather than aliasing. However, this practice introduces some blurring effects and will be discussed in the following section.

The electronics model for the detector bridge, preamp, power amp and the Bessel filter is detailed in Table 1 which also shows the parameter values for the electronic system. Augmenting the electronic model in Table 1 with the heat sink controller in (3), the complete electronic model can be expressed as



$$\begin{array}{lll}
 K_{H1} = 0.004425 & \tau_{H1} = 5 & R_H = 157 \, \Omega \\
 K_{H2} = 0.0453 & \tau_{H2} = 44 &
 \end{array}$$

Figure 11. Scanner Heater Controller Model

Table 1. Scanner Electronics

BRIDGE:

Constants/Parameters	SW	LW	Total
K	3.4067	6.2067	2.32
K_B	0.0002623	0.0002652	0.0002583
$\tau_1(\text{sec})$	1.4388×10^{-5}	1.52698×10^{-5}	1.35745×10^{-5}
$R_0 (= R_{10} = R_{30} \text{ at } 38^\circ \text{C})$	1.5×10^5	1.5×10^5	1.5×10^5
$T_0(^{\circ}\text{K})$	311.16 $^{\circ}\text{K}$	311.16 $^{\circ}\text{K}$	311.16 $^{\circ}\text{K}$

$$\beta_i = 4 * (T_i - 293.16) + 3330 \text{ } (^{\circ}\text{K})$$

PREAMP:

Constants/Parameters	SW	LW	Total
$E_{os} \text{ (volt)}$	25×10^{-6}	25×10^{-6}	25×10^{-6}
$C_B \text{ (Amp)}$	$\pm 2 \times 10^{-9}$	$\pm 2 \times 10^{-9}$	$\pm 2 \times 10^{-9}$
K_c	-----	-----	-----
$\tau_2 \text{ (sec)}$	1.7578×10^{-3}	1.7578×10^{-3}	1.7578×10^{-3}
$\tau_3 \text{ (sec)}$	1.53743×10^{-5}	1.63298×10^{-5}	1.45612×10^{-5}

AMP & FILTER:

Constants/Parameters	SW	LW	Total
K_{fo}	20.83	61.62	13.03
τ_{n1}	9.4575×10^{-3}	9.4575×10^{-3}	9.4575×10^{-3}
τ_{n2}	8.51172×10^{-3}	8.51172×10^{-3}	8.51172×10^{-3}
ω_{n1}	1.05736×10^2	1.05736×10^2	1.05736×10^2
ω_{n2}	1.17485×10^2	1.17485×10^2	1.17485×10^2
ζ_1	1.0	1.0	1.0
ζ_2	0.62678	0.62678	0.62678

Table 1. (Continued) Scanner Electronics

ELECTRICAL SIGNAL PROCESSING MODEL

$$\dot{x}_1 = -\frac{1}{\tau_1} x_1 - \frac{K_B R_{10} \beta_1}{\tau_1 T_0^2} T_1 + \frac{K_B R_{30} \beta_3}{\tau_1 T_0^2} T_3 + \frac{K_B (R_{10} \beta_1 - R_{30} \beta_3)}{\tau_1 T_0}$$

$$\dot{x}_2 = -\frac{1}{\tau_2} x_2 + \frac{1}{\tau_2} x_1 + \frac{\tau_3}{\tau_2} \dot{x}_1 - \frac{K_c}{\tau_2} C_B + \frac{1}{\tau_2} (E_{os} + n) + \frac{\tau_3}{\tau_2} (\dot{E}_{os} + \dot{n})$$

$$\dot{x}_3 = -2\zeta_1 \omega_{n1} x_3 - \omega_{n1}^2 x_4 + K_{fo} \omega_{n1}^2 x_2$$

$$\dot{x}_4 = x_3$$

$$\dot{x}_5 = -2\zeta_1 \omega_{n2} x_5 - \omega_{n2}^2 x_6 + \omega_{n2}^2 x_4$$

$$\dot{x}_6 = x_5$$

where x_6 is going to be signals.

$$\dot{x} = A_x x + B_x T + B_{os}(E_{os} + n) + B_s T_s + b \quad (4)$$

where x is an 8-component state vector of electrical system variables, T is a 14-component vector of the thermal node element temperatures, E_{os} is an operating voltage, n is the total noise viewed at the preamp input and T_s is the set temperature for the heat sink controller. A_x , B_x , B_{os} and B_s are appropriately dimensioned matrices.

Using a lumped-parameter approach, the thermal conductive and radiative transfer among the elements shown in Fig. 2 can be expressed in terms of the node element temperatures, T_i , forming the vector T .

$$\dot{T} = AT + DT^4 + B_Q \dot{Q}_8(x_8) + BL \quad , \quad (5)$$

where T^4 represents the vector whose i^{th} component is T_i^4 , $\dot{Q}_8(x_8)$ is the Joule heating power produced by the heat sink controller and L is the incoming radiation.

Figure 12 shows the simulation results obtained using the dynamic model described by (4) and (5). The input radiance is a square wave with a 4 second period, one full scan of the ERBE scanner. During the first 2 seconds, no incoming radiation is present; e.g., a space look condition; during the last 2 seconds, the sensor sees a radiance of 175 W/m²-sr, before the cycle repeats.

As seen in the plots in Fig. 12, the analog output (before sampling) produces a good replica of the incoming radiation. A more careful look shows that the output has a trapezoidal shape which is caused by the temporal processing due to the thermal and electrical transients. In other words, the scanner output lags its input largely due to the low-pass filter.

The active flake temperature, T_1 , rises sharply in response to the leading edge of the square wave and then continues to rise at a slower rate, thus displaying the presence of multiple modes in the system. The response of the active thermistor flake clearly is not a

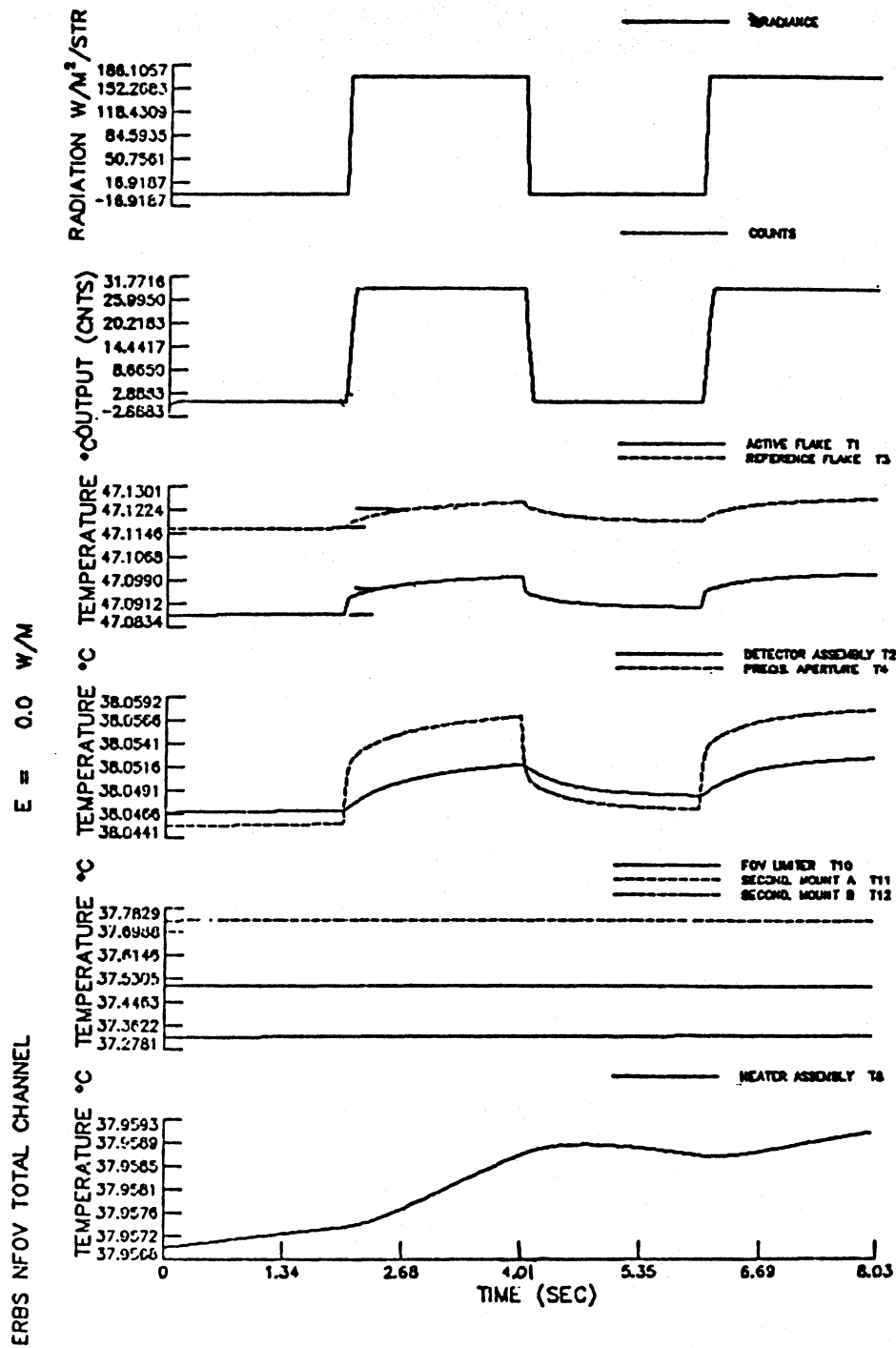


Figure 12. Simulation of ERBE Total Scanner Thermal and Electrical Variables

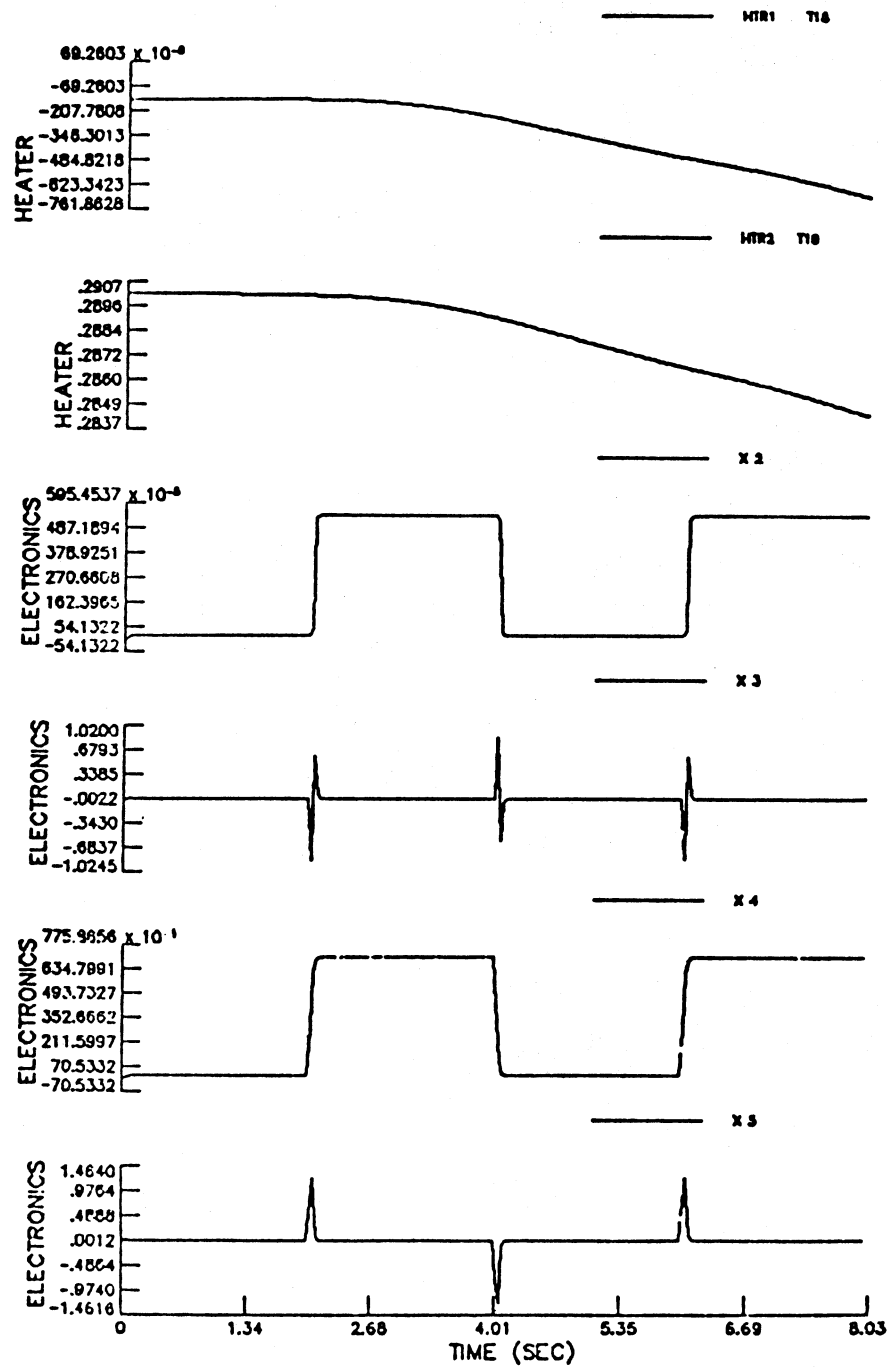


Figure 12. (Continued) Simulation of ERBE Total Scanner Thermal and Electrical Variables

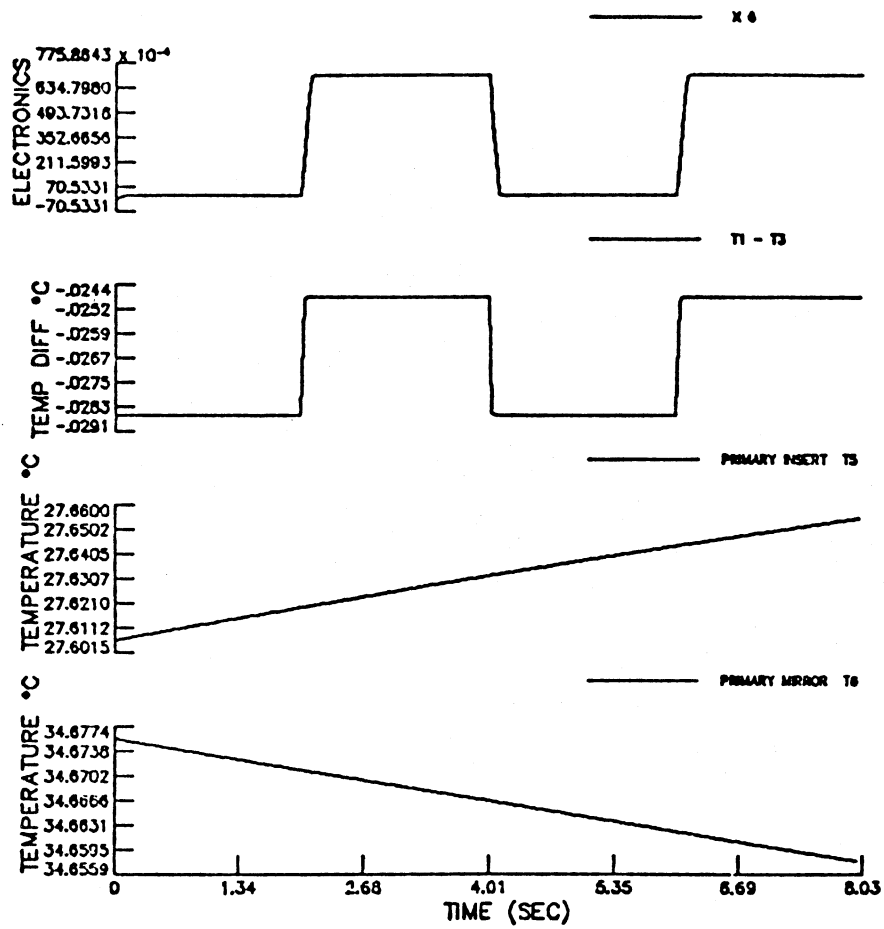


Figure 12. (Concluded) Simulation of ERBE Total Scanner Thermal and Electrical Variables

replica of the incoming radiation as it continues to increase while the input is flat. However, the active flake conducts its heat to the detector assembly, T_2 , which then conducts to the reference flake, T_3 .

As the simulation shows, the reference flake temperature does remain constant during this period of time; rather it increases at about the same rate as the active flake temperature. As a result, the temperature difference between the active and reference flakes produce an excellent replica of the incoming radiation. The plot of this temperature difference, $T_1 - T_3$, is seen to respond almost simultaneously to the leading edge of the square wave. On the other hand, x_6 which is the analog output voltage is slightly delayed. This behavior indicates that the thermal response of the flakes is quite fast, having a time constant of about 12 msec.

Therefore, the lag in the scanner output is largely due to the low-pass filtering. Another conclusion is that the balancing role of the reference is quite important to the proper operation of the scanner. Other simulations not presented here show a natural frequency of the combined radiative-thermal-electronic system with a period of about 24 sec., or a 4 scan duration. Further, slower modes are also present although of less significance to the radiometric signal. Further simulation details can be found in [5].

C. Effective Point Spread Function.

The instantaneous field-of-view (IFOV) of the scanner is largely determined by the precision aperture and the optic system. For the ERBE scanners, the precision aperture has a hexagonal shape with a 3° aperture in scan direction and up to 4.5° in the satellite track direction, as shown in Fig. 4. When the sensor input is not changing and the scanner sees the same footprint, the IFOV describes the point spread function (PSF). A discrete step scanner which can stay at a given scan angle long enough for transients to die down would fall in this category, although it may have other disadvantages.

As the simulation described in the last section shows, the scanner output is influenced by temporal processing (thermal, electronic) as well as spatial processing (IFOV). For

continuous scanners which have a low-pass filter, the sensor output will be a weighted average of the radiation arriving from the current and past locations of the footprint. To avoid excessive blurring and aliasing errors, it is desirable to use a low-pass filter with a cut-off near the Nyquist frequency [3].

It is possible to combine both spatial and temporal processing into an effective point-spread function which explicitly shows the weighting of each point in the scene in a given measurement by means of a convolution. This, however, turns out to correspond to an optical transfer function (OTF) which has non-zero phase characteristics, unlike most optical systems which have zero phase. In this case, the non-zero phase (or alternately complex-valued OTF) is being introduced by the causal nature of temporal processing, as can be seen from the following.

Effective Spatial Response

To model the effects of electrical filtering (or processing) on the overall electro-optical system, we will consider a scanner where the scanning axis, say y , is perpendicular to the x -axis in which the relative motion of the scanner center of mass and the scene occurs. Other types of scanning strategies can be analyzed and modeled in a similar fashion, but will not be treated here. The electrical filtering is actually performed on the analog signal which is obtained by the optical system. Thus, the scanning axis, y , runs along the time axis. We will assume that the scanner's relative motion along the x -axis is much slower in comparison to the scanning motion of the optical axis, or alternately, the scanning speed is assumed to be much faster than the relative motion of the device.

Let $h_e(t)$ be the impulse response of the electrical filter processing the signal obtained by the Optical Transfer Function (OTF), $\hat{r}_o(\nu, \omega)$. Thus, the Electrical Transfer Function (ETF), $\hat{h}_e(\omega')$, is given by the one-dimensional Fourier transform

$$\hat{h}_e(\omega') = \int_{-\infty}^{\infty} h_e(t) e^{-2\pi i \omega' t} dt \quad , \quad (6)$$

where ω' is the temporal frequency variable in units of cycles per sec. In most continuous scan systems, the electrical processing used is low-pass filtering with the ETF corresponding to standard low-pass filters such as the Butterworth, Tchebycheff, Bessel filters.

The input-output relationship of the electrical filter is given by the one-dimensional convolution

$$o(t) = \int_{-\infty}^{\infty} h_e(t') i(t - t') dt' \quad , \quad (7)$$

where $i(t)$ and $o(t)$ are the input and output signals, respectively. It is assumed here that transient effects due to initial conditions have died down to negligible levels.

On the other hand, when the optical axis points along (x, y) , the optical system input-output relationship is given by the two-dimensional convolution

$$g(x, y) = \int_{-\infty}^{\infty} \int_{-\infty}^{\infty} \tau_o(x', y') L(x - x', y - y') dx' dy' \quad (8)$$

where $L(x, y)$ is the scene radiance input to the sensor and $g(x, y)$ is the output, and $\tau_o(x, y)$ is the optical Point Spread Function (PSF) corresponding to the OTF, $\hat{\tau}_o(\nu, \omega)$.

Now suppose that, at time t , the optical axis points along $(x(t), y(t))$ producing the signal $g(x(t), y(t))$. Then, the analog output of the electrical filter is given by

$$s(x(t), y(t)) = \int_{-\infty}^{\infty} h_e(t') g(x(t - t'), y(t - t')) dt' \quad , \quad (9)$$

where the output of the electronics, $s(x(t), y(t))$, has been associated with the optical axis direction $(x(t), y(t))$ rather than simply time, t .

As mentioned earlier, the scanning motion along y is much faster than the motion along x . Thus, we assume that $y(t - t')$ varies along the scan direction, while $x(t - t')$ remains essentially unchanged over the period of a scan; i.e.,

$$x(t - t') \approx x(t) \quad , \quad (10)$$

$$y(t - t') = \dot{y}(t - t') = \dot{y}t - \dot{y}t' \quad , \quad (11)$$

when $t - t'$ is of the order of a scan period, but is much larger than the electrical filter time constants, and where \dot{y} is the linear scan rate. Substituting (10) and (11) into (9) and manipulating,

$$\begin{aligned} s(x(t), y(t)) &= \int_{-\infty}^{\infty} h_e(t') g(x(t), \dot{y}t - \dot{y}t') dt' \\ &= \frac{1}{\dot{y}} \int_{-\infty}^{\infty} h_e\left(\frac{y'}{\dot{y}}\right) g(x(t), y(t) - y') dy' \end{aligned} \quad (12)$$

$$= \int_{-\infty}^{\infty} \int_{-\infty}^{\infty} \tau_e(x', y') g(x(t) - x', y(t) - y') dx' dy' \quad (13)$$

where

$$y' = \dot{y}t' \quad , \quad (14)$$

$$\tau_e(x', y') = \frac{1}{\dot{y}} h_e\left(\frac{y'}{\dot{y}}\right) \delta(x') \quad , \quad (15)$$

and $\delta(x')$ is the Dirac delta function.

It is seen that the effect of the electrical filter in the spatial domain can be expressed by the PSF $\tau_e(x', y')$ and a two dimensional convolution, as shown in (13).

Taking the 2-D Fourier transform of (13), and using (8),

$$\hat{s}(\nu, \omega) = \hat{\tau}_e(\nu, \omega) \hat{g}(\nu, \omega) = \hat{\tau}_e(\nu, \omega) \hat{\tau}_o(\nu, \omega) \hat{L}(\nu, \omega) \quad . \quad (16)$$

Taking the Fourier transform of (15), and manipulating,

$$\hat{\tau}_e(\nu, \omega) = \hat{h}_e(\dot{y}\omega) = \hat{\tau}_e(\omega) \quad , \quad (17)$$

where ω is the spatial frequency variable corresponding to the scan direction; i.e., the y-axis. It should be noted that since $\hat{\tau}_e$ varies only with ω and is independent of ν , we will treat it as a function of ω alone to emphasize this fact.

From (16) and (17), it is seen that the effective OTF for the combined electro-optical system is given by

$$\hat{\tau}(\nu, \omega) = \hat{\tau}_e(\omega) \hat{\tau}_o(\nu, \omega) = \hat{h}_e(\dot{y}\omega) \hat{\tau}_o(\nu, \omega) \quad , \quad (18)$$

where \hat{h}_e is the temporal transfer function of the electrical filter, and \dot{y} is the scan rate. Thus, given $\hat{h}_e(\omega')$ and the scan rate, it is a simple matter to obtain the effective spatial OTF.

Similarly, it can be shown that the effective system PSF, $\tau(x, y)$, can be obtained as a one-dimensional convolution.

$$\tau(x, y) = \int_{-\infty}^{\infty} \frac{1}{\dot{y}} h_e\left(\frac{y'}{\dot{y}}\right) \tau_o(x, y - y') dy' \quad , \quad (19)$$

which is the inverse Fourier transform of the effective system OTF, $\hat{\tau}(\nu, \omega)$.

It is important to note that any temporal effects which can be expressed in terms of a convolution can be analyzed in this manner. For example, thermal dynamics which may be present in the sensors can be included in the term $\hat{h}_e(\omega')$ and analyzed in the same way as electrical processing.

The most significant aspect of (18) is the fact that the effective OTF, $\hat{\tau}(\nu, \omega)$, is now a complex-valued function. Whereas the optical transfer function, $\hat{\tau}_o(\nu, \omega)$, is usually a real-valued function, the electrical transfer function, $\hat{h}_e(\omega')$, is rarely, if at all, real-valued. Thus, in general, $\hat{\tau}_e(\omega)$ and $\hat{\tau}(\nu, \omega)$ now have magnitude as well as phase characteristics due to a non-zero imaginary part.

The existence of non-zero and non-linear phase characteristics in the image-gathering system essentially produces a "blurring" effect which adds to the blurring due to the

magnitude characteristics. Any known optical phase aberrations can also be included in $\hat{\tau}_o(\nu, \omega)$.

The transfer functions involved can be expressed in terms of their magnitude and phase in the form:

$$\hat{h}_e(\omega') = |\hat{h}_e(\omega')| e^{i\varphi_e(\omega')} \quad , \quad \hat{\tau}_o(\nu, \omega) = |\hat{\tau}_o(\nu, \omega)| e^{i\varphi_o(\nu, \omega)} \quad . \quad (20)$$

The effective system OTF can now be written as

$$\hat{\tau}(\nu, \omega) = |\hat{h}_e(\dot{y}\omega')| |\hat{\tau}_o(\nu, \omega)| e^{i[\varphi_e(\dot{y}\omega) + \varphi_o(\nu, \omega)]} \quad (21)$$

From (20), it is seen that, when the optical system has no phase aberrations, the effective system OTF phase is precisely the electronic phase, while the magnitude effects are multiplicative and depend on both optical and electrical system characteristics.

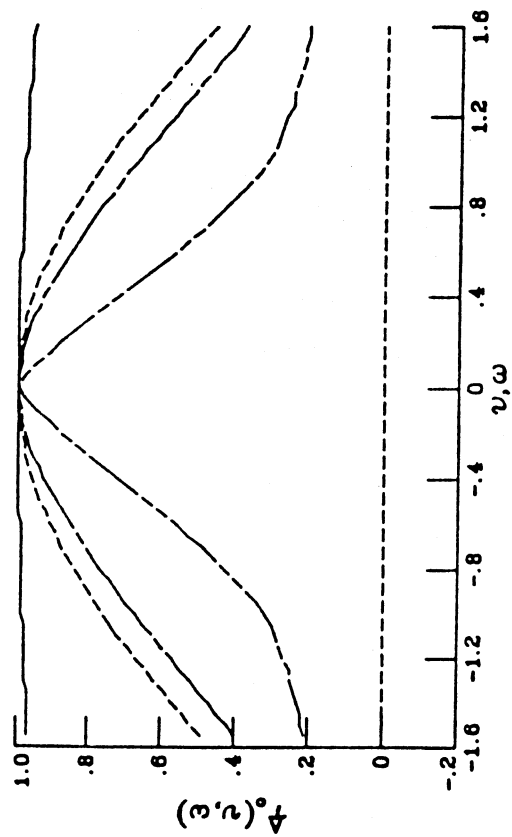
It should be noted that for causal, or non-anticipating, electrical filters, the impulse response is constrained by

$$h_e(t) = 0 \quad , \quad t < 0 \quad (22a)$$

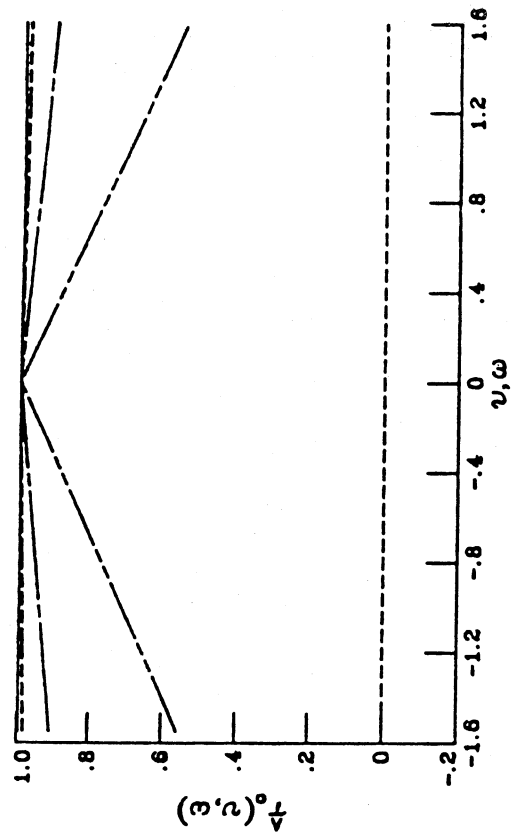
so that the filter can be implemented in real time. This causality condition simply requires that the output at time t depend only on the input till time t so that the current output of the filter does not depend on the future input. From (15), this causality condition requires that the effective PSF of the electrical filter satisfy the condition

$$\tau_e(x, y) = 0 \quad , \quad y < 0 \quad . \quad (22b)$$

Now we can use (18) to obtain the effective spatial response of the ERBE scanners. The OTF of the ERBE scanner is determined by the combined effects of the Cassegrain optics and the aperture shape. Figure 13 shows the spatial frequency response of the Cassegrain optics at various wavelengths ranging from shortwave to longwave. For the



(a) Cassegranian system.



(b) Diffraction limited lens.

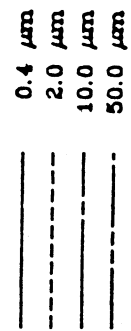


Figure 13. Spatial Frequency Response of the Optics

wavelengths of most interest, the OTF frequency response is quite flat and is not a limiting factor in the frequency domain.

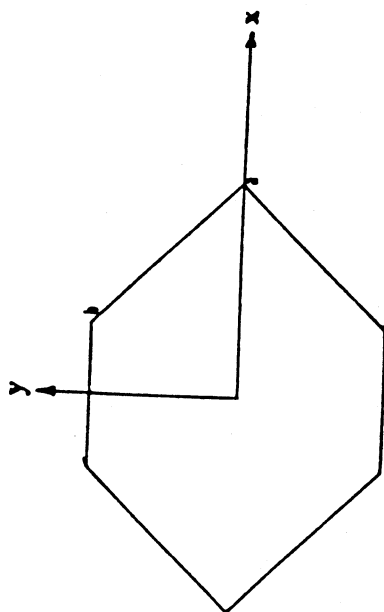
Figure 14 shows the frequency response of the hexagonal aperture used in the ERBE scanners. In comparison to the optics, it is clear that the combined optical transfer function will be dominated by the precision aperture OTF.

The various electronic subsystem frequency response are shown in Fig. 15. Note that these are shown as spatial frequency responses according to (17). For this purpose, the detector bridge frequency response includes the thermal processing which occurs in the conductive paths between the active and reference flakes. As noted earlier, (18) is valid for any temporal processing whether it is electrical or thermal. The detector bridge effects, while not being completely negligible, are dominated by the frequency response of the 4-pole Bessel filter. Further note that the imaginary parts of these OTF's are non-zero.

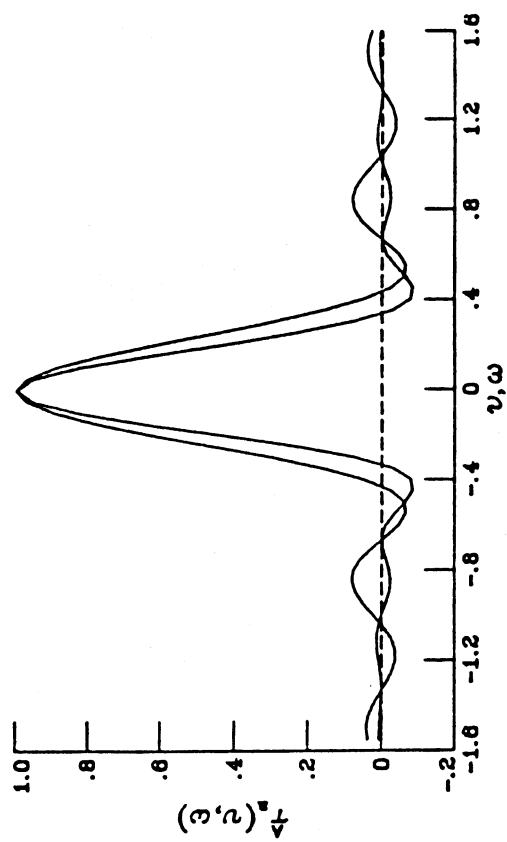
Combining the optical, thermal and electrical transfer functions into an overall effective OTF results in the frequency responses shown in Fig. 16. In the scan direction, the response is dominated by the temporal response, rather than the aperture of the scanner. This is an indication that the filter cut-off is too low. For the ERBE scanner, the Nyquist frequency is 15 Hz or 0.225 cycles/° in the spatial domain. Thus, a desirable level for the temporal frequency response would be e^{-1} at $\omega = 0.225$ cycles/°. Note that at this level, the aperture and electrical systems would roughly contribute equally to the effective PSF.

Figure 17 shows the effective spatial response of the ERBE scanners. While the response along track is not changed much, the response in the scan direction has been significantly altered. The most significant effects are that the effective PSF 1) is shifted in the scan axis, 2) is not symmetrical and displays a "tail" and 3) has a wider "effective footprint" than the aperture in the scan direction.

While these effects can be reduced significantly by dynamic processing, zero-memory type solutions are limited.

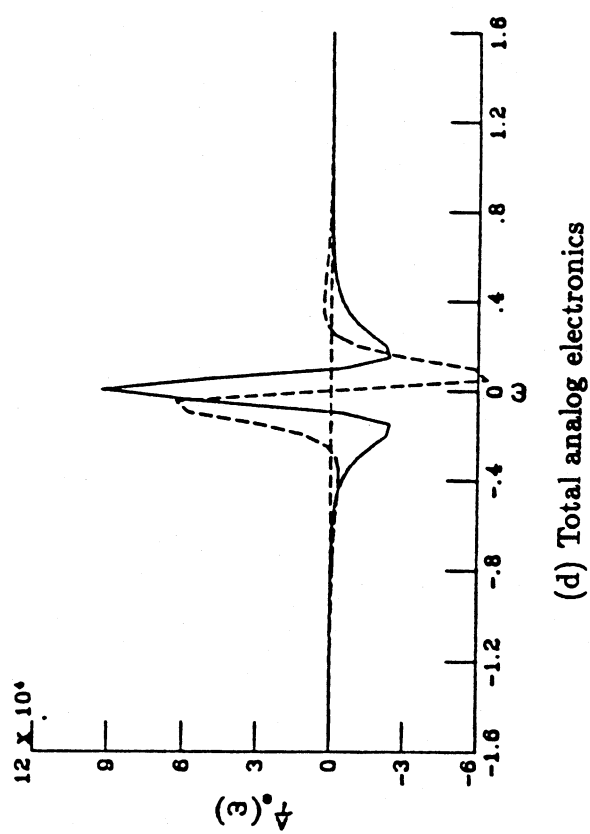
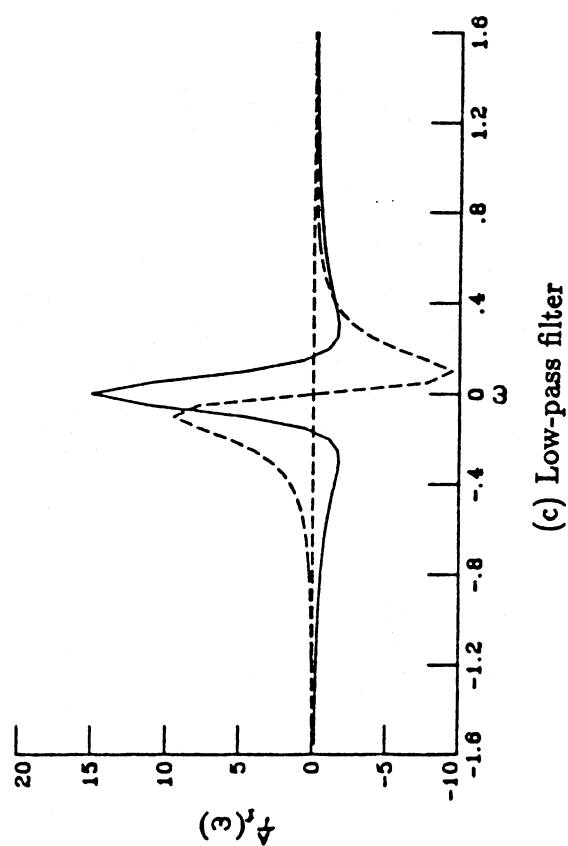
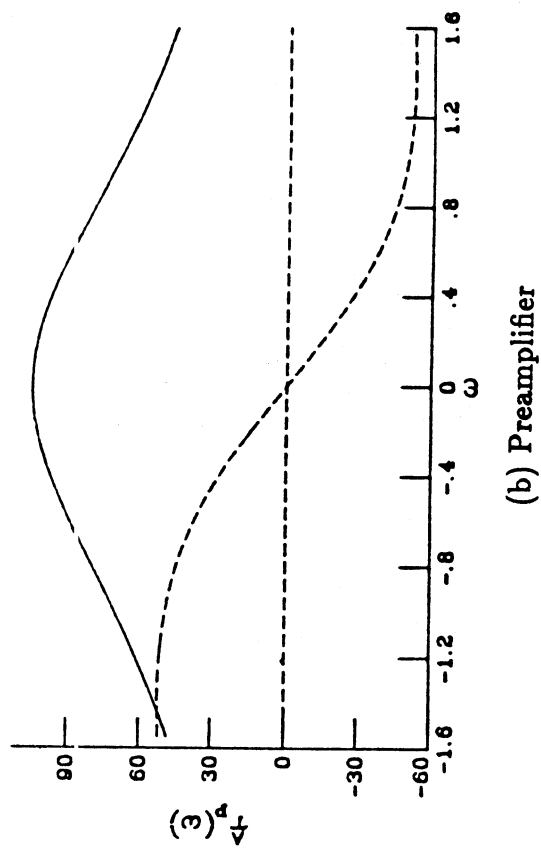
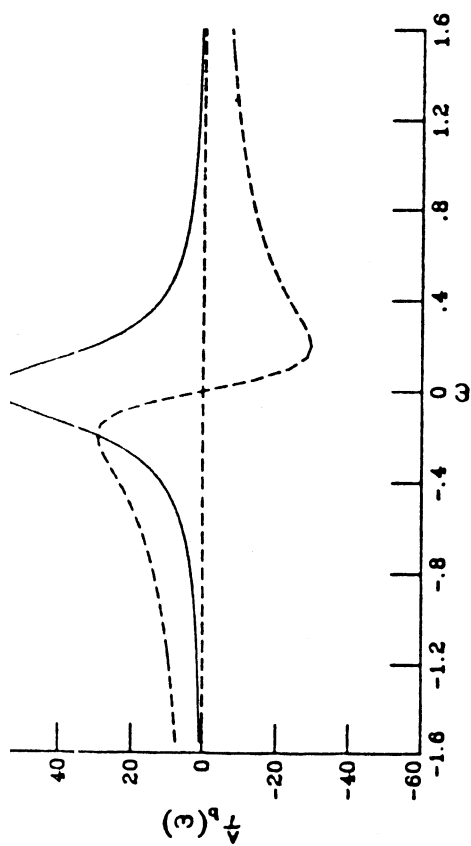


(a) Aperture shape in degrees.



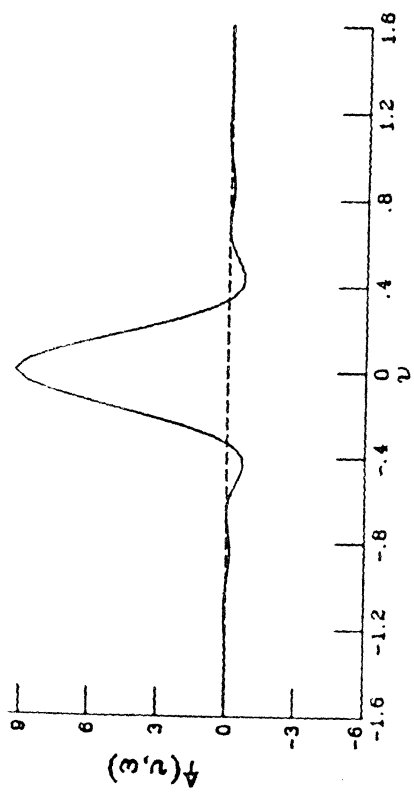
(b) Frequency response of the aperture.

Figure 14. Shape and Spatial Frequency Response of the Detector Aperture

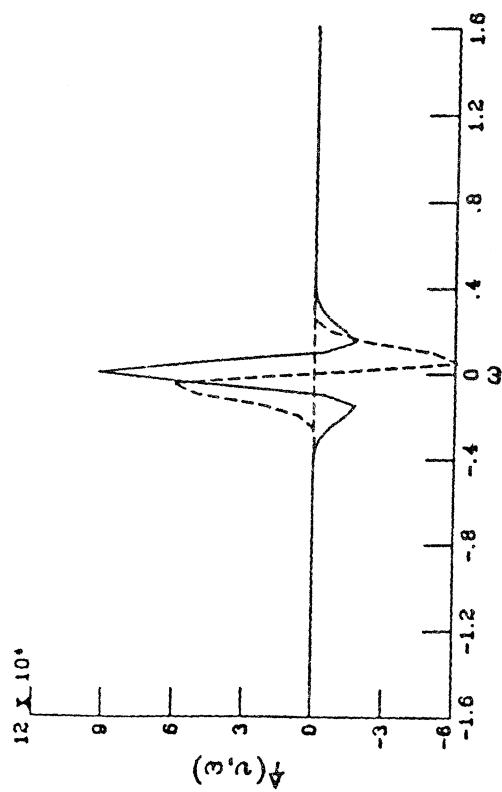


— Real Value
 --- Imaginary Value

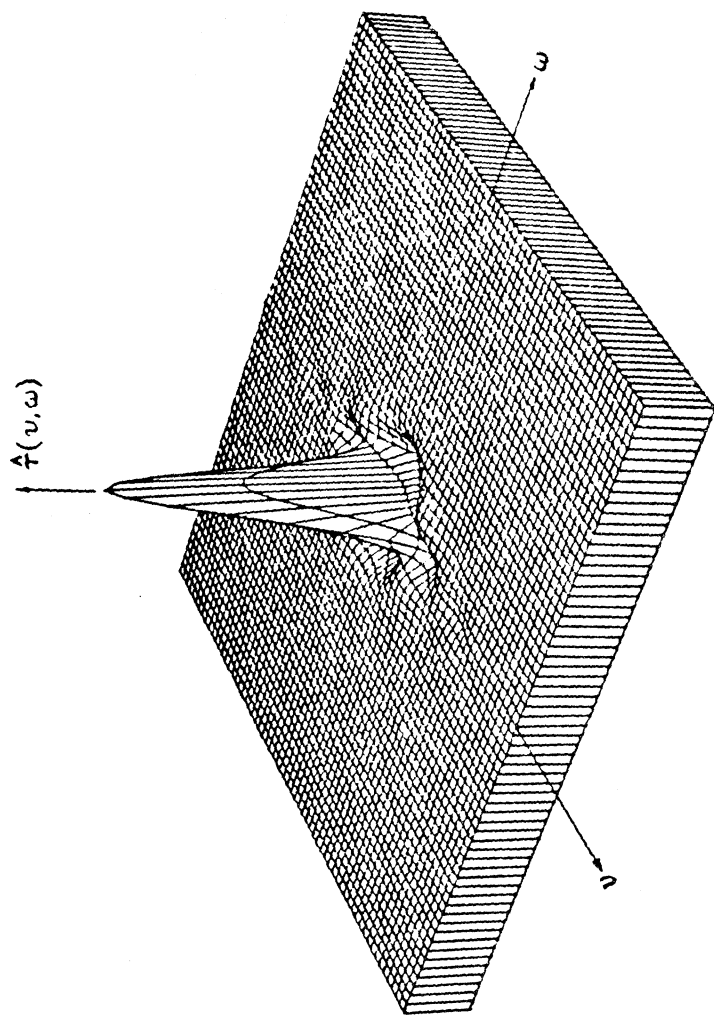
Figure 15. Frequency Response of the Electronics as a Function of Cycles/Degree



(a) Normal to the line-scan direction.

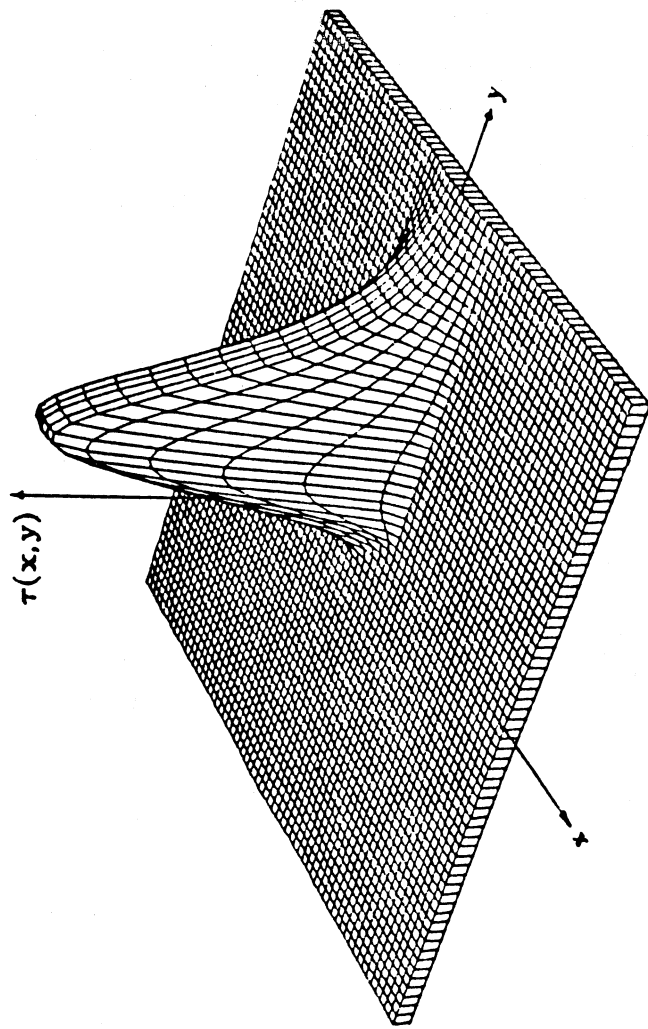


(b) Along the line-scan direction.

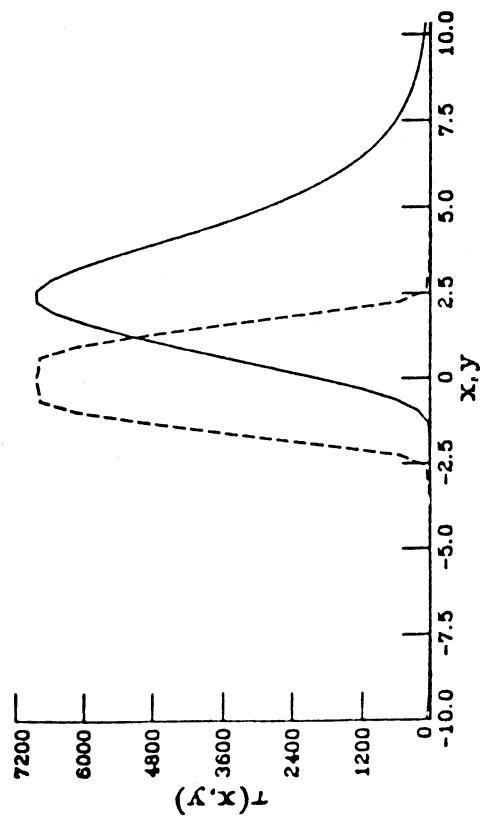


(c) Perspective of the real component.

Figure 16. Effective Spatial Frequency Response Function of ERBE Scanners



(b) Perspective.



(a) Along line-scan direction, and normal

Figure 17. Effective Spatial Response of ERBE Scanners

D. Interpretation Algorithms (Count Conversion).

In the previous sections, we have described the main characteristics of the ERBE scanners as combined optical-thermal-electrical systems. However, for calibration and data reduction purposes, what is desired is an algorithm which produces the scanner input (i.e., the incoming radiation) when the system output is known. In other words, the processing performed by the optical, thermal and electrical systems must be inverted; i.e., the inverse operator of the scanner system is derived.

On the other hand, from the standpoint of computational time, it is desired to have as simple an algorithm as possible, since the huge amount of data to be processed places a soft limit on the complexity of data reduction algorithms. A gain/offset type equation was typical.

With the basic constraints mentioned above, dynamic processing in the algorithm was not considered desirable, so that a steady-state view was taken. The following algorithm was selected to interpret the sensor's radiometric output voltage, $v(t)$.

$$\begin{aligned}\hat{L}_d(t - \tau) = & A_v [v(t) - \bar{v}(t_k) - \sigma(t)] + \frac{t - t_k}{\Delta t} [A_s(\bar{v}(t_{k+1}) - \bar{v}(t_k)) \\ & + A_H(T_H(t_{k+1}) - T_H(t_k)) + A_D(V_D(t_{k+1}) - V_D(t_k))] \quad (23)\end{aligned}$$

where $\bar{v}(t_k)$ is the average value of the eight output samples during the space look at the beginning of the scan starting at time t_k , Δt is the scan duration of 4 sec., $\sigma(t)$ is an offset dependent on the sample during the scan and will be discussed in more detail later. The housekeeping data $T_H(t_k)$ and $V_D(t_k)$ are transmitted to earth once every scan and are not available during the scan. $T_H(t)$ is the heatsink temperature (more precisely, T_7) which is used to drive the heatsink controller, and $V_D(t)$ is the DAC drift voltage.

An additive term in the detector bridge voltage $V_B(t)$ was considered then dropped as the calibration data showed practically no variation in $V_B(t)$ during the ground calibration. From the analysis of the electronic system, however, it is seen that the effect of variations

in V_B is multiplicative rather than additive. Thus, the coefficients, A_v , A_s , A_H and A_D are implemented according to:

$$A_v = \frac{AV}{c V_B(t)} \quad , \quad (24a)$$

$$A_s = \frac{AVA}{c V_B(t)} \quad , \quad (24b)$$

$$A_H = \frac{AHA}{c V_B(t)} \quad , \quad (24c)$$

$$A_D = \frac{AD}{c V_B(t)} \quad , \quad (24d)$$

where AV , AVA , AHA and AD are constants determined during ground calibration, and c is the digital to analog conversion factor.

$$c = 409.5 \text{ counts/volt} \quad (25)$$

The first term in (23) is the most important term, with the remaining terms playing a relatively smaller role. The input of the second term in (23) is to allow for small but systematic effects not included in the first term. Note that the space clamp difference and heatsink temperature difference are correlated. Thus, the coefficients for these terms are determined from ground calibration data to allow for unexpected effects which may not be constant during the scan, but occur in a systematic manner every scan.

Finally, the effect of the temporal processing discussed in the last section is approximately accounted for by the delay τ in (23). As mentioned, a dynamic algorithm would be required to reduce the distortion or blurring introduced. However, the delay at least recognizes that the scanner voltage output at time t is more representative of the IFOV at $t - \tau$ than it is of the current IFOV. The value used is 46 msec. which corresponds to the most significant time constant of the temporal processing. Using some flight data, this delay was validated to within 10% and the value modified.

III. CALIBRATION

A. Calibration Sources.

The ERBE ground calibration was performed in a calibration chamber especially designed for obtaining the required measurements. The calibration chamber is shown in Fig. 18. To achieve high accuracy, the ground calibration is performed in vacuum. The calibration sources are the Master Reference Blackbody (MRBB), shown in Fig. 19, and the ERBE Integrating Sphere, shown in Fig. 20, placed at opposite ends of the ERBE calibration chamber. A Solar Simulator is also available to produce a radiation source similar to the solar spectrum and intensity. The MRBB provides a highly accurate longwave calibration source, while the integrating sphere provides a calibration with both shortwave and longwave radiation [6] - [9].

The MRBB has six calibrated platinum resistance thermometers (PRT) mounted at selected points which verify the uniformity of its surface temperature and is traceable to the IPTS68.

The ERBE integrating sphere provides a calibration source containing both short-wave and longwave radiation, thus producing a spectral content similar to earth's. The shortwave radiation is obtained from four 250 W tungsten lamps through a projection optics system that reflects the light off a mirror before entering the sphere through four entrance ports made of flashed opal glass. The flashed opal glass are intended to diffuse the light uniformly onto the sphere wall thus producing an uniform sphere wall radiance. The sphere wall is coated by 3M White Velvet and then Barium Sulfate thus producing a uniform and diffuse reflectivity over the sphere wall. The sphere wall radiance is monitored by two silicon photodiodes (SiPD) with wide fields-of-view. For an uniform wall radiance, the intensity at an arbitrary point of the sphere can be thus monitored.

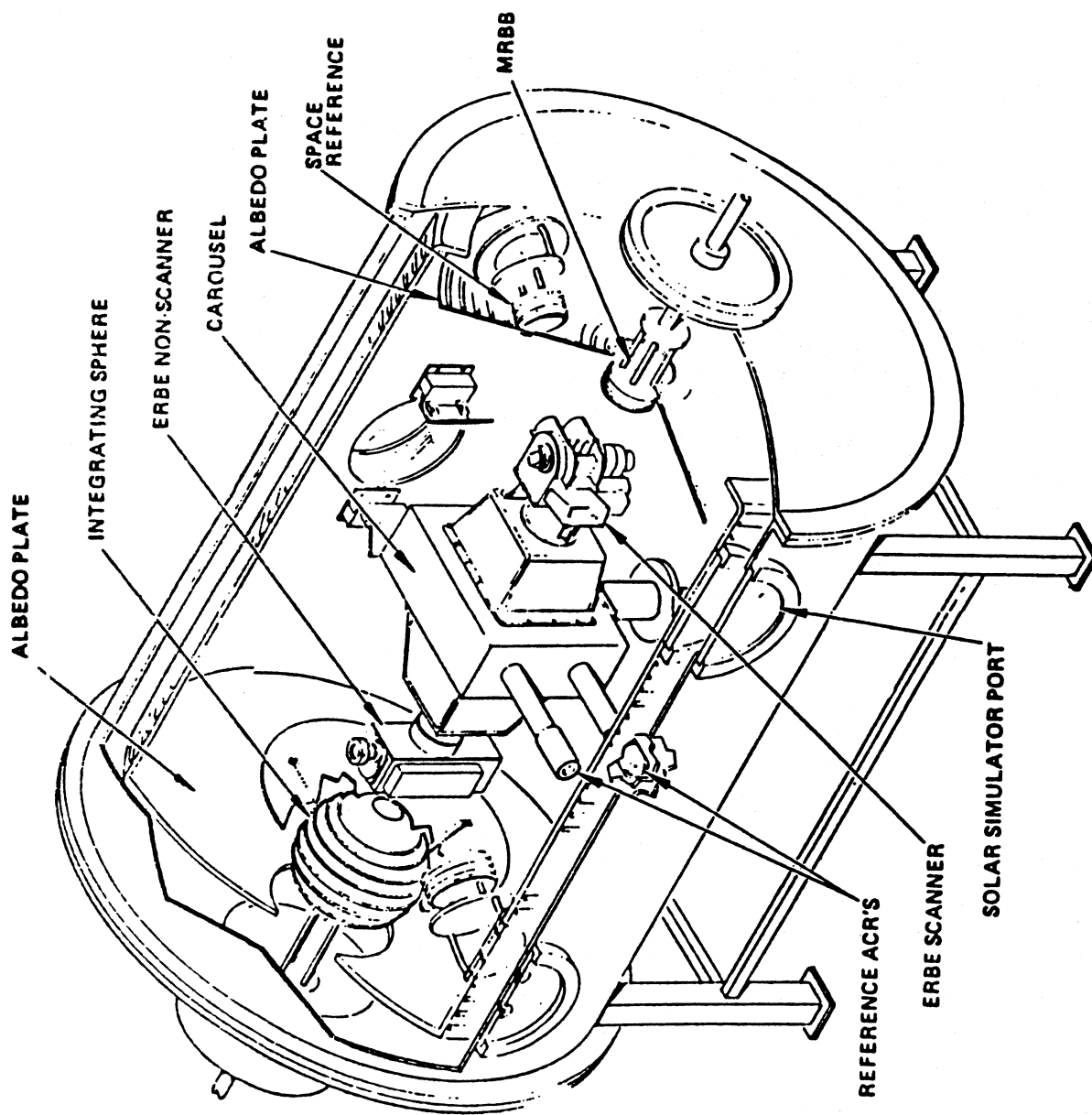


Figure 18. ERBE Calibration Chamber

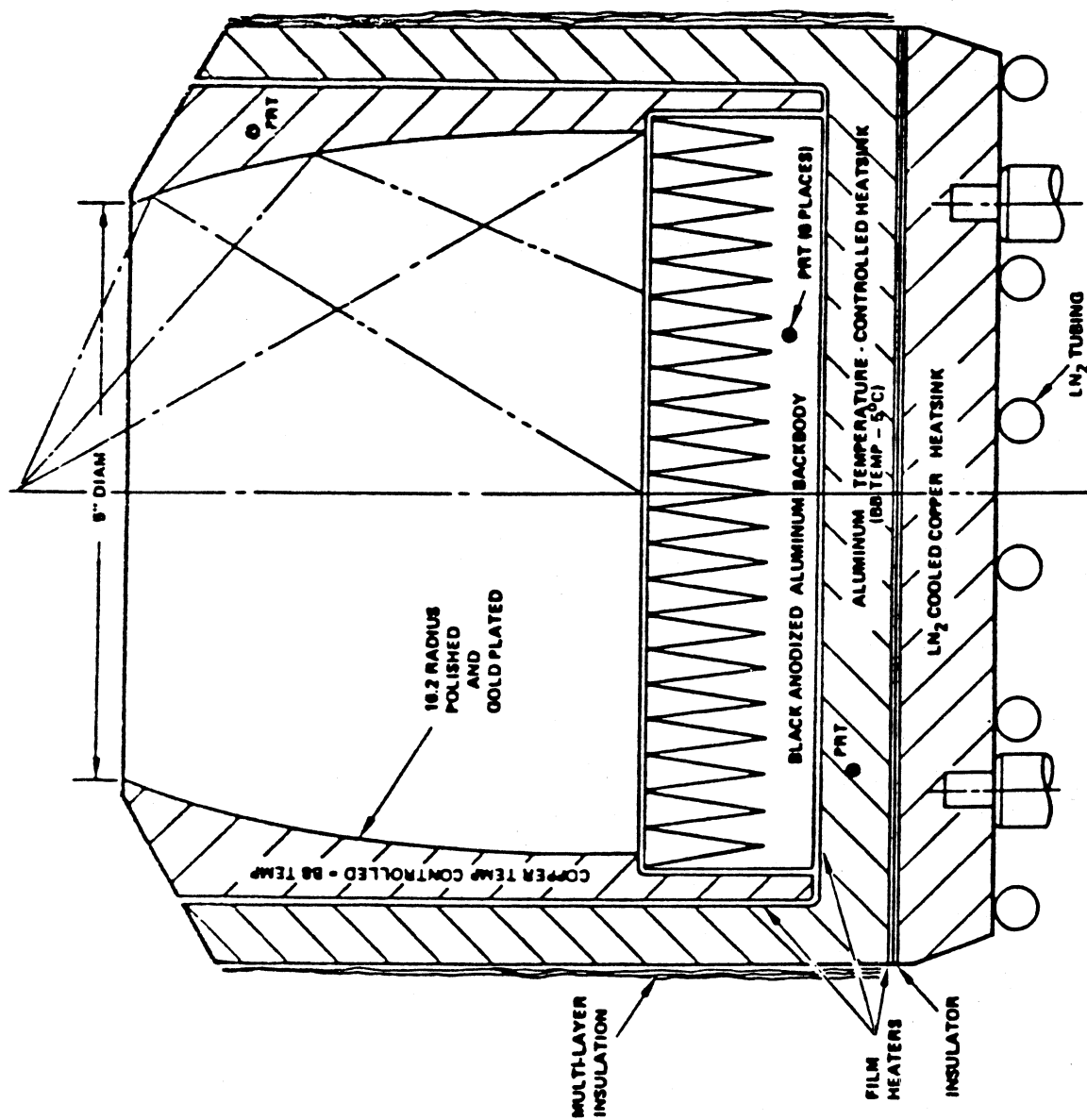


Figure 19. Cross Section of Master Reference Blackbody (MRBB)

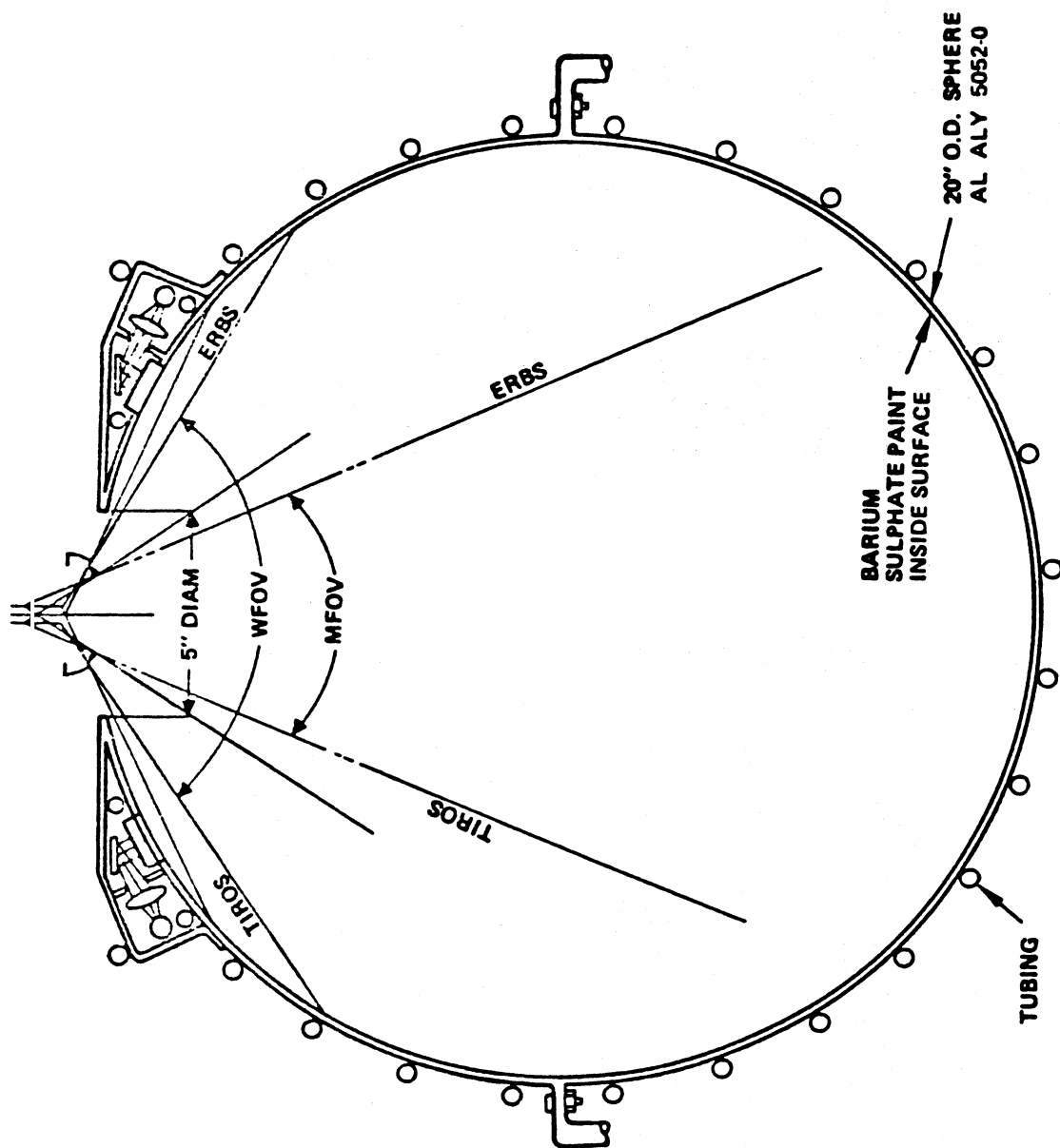


Figure 20. Integrating Sphere

The intensity of the light entering the sphere can be varied by blocking part of the radiation from the entrance ports. Thus, various levels of shortwave radiation can be mixed with a given intensity of longwave radiation emitted by the sphere wall. The sphere wall temperature is controlled by circulating a water and alcohol mixture through a tubing around the outer wall of the sphere. By making measurements of the sphere wall radiance at various levels of shortwave (including lamps off or no shortwave) and longwave radiation whose intensity is known by the SiPD measurements, it is possible to calibrate the scanners by scanning the uniform sphere wall.

During the ground calibration the integrating-sphere data showed the following characteristics:

- (1) The NFOV scanning sensors measure non-uniformities (8%) on the sphere wall after known sources of error are taken into account to the extent possible.
- (2) The MFOV nonscanner sensor consistently measures a higher irradiance than does the WFOV nonscanner sensor for both longwave and shortwave radiation.
- (3) The integrating sphere photodiode response shows nonlinear characteristics relative to the nonscanner measurements.
- (4) With the lamps off, the nonscanner sensors measure a higher (longwave) irradiance than expected by about 10 - 20 W/m².

The non-uniformity of the sphere wall can be seen in Fig. 21 which shows measurements of the ERBE shortwave sensor as it scans the sphere wall. As a result of the non-uniformity and the other unexpected phenomena, the SiPD measurements, having a wide field-of-view, do not provide the shortwave intensity. The causes of these effects are investigated and explained in [9] which also suggests a different procedure to calibrate the shortwave ERBE scanners and nonscanners.

B. Calibration Procedures.

The objective of the calibration is to obtain the coefficients necessary for the interpretation of the sensor output, namely, obtaining the coefficients in the algorithm developed

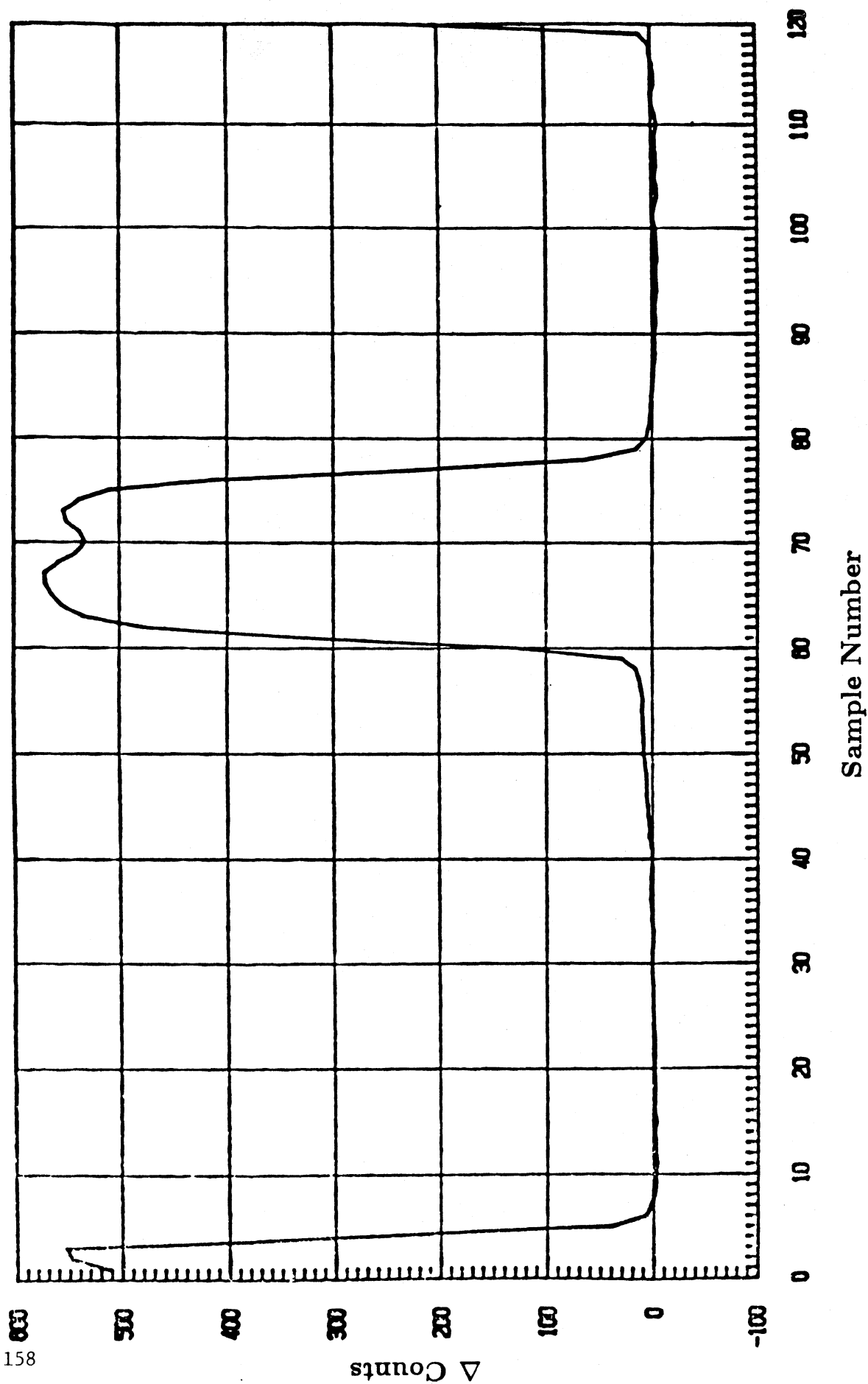


Figure 21. Actual Measurements of the ERBE Shortwave Scanner
Instrument Scanning the ERBE Integrating Sphere

in Section II-D. These coefficients consist of AV , AVA , AHA and AD in (24) and the offsets $\sigma(t)$ which are then substituted into (23) to compute the estimate of the radiative power absorbed by the active flake.

Originally, a constant offset throughout the complete scan had been expected. However, during the ground calibration, significant variations in the offset during a scan were noticed. When scanning a uniform wall, the scanner output tends to vary according to the sample number, repeating regularly in successive scans. As a result an offset, $\sigma(t)$, which depends on the sample number during the scan, but not on the particular scan, is included in the sensor interpretation algorithm (23). The precise cause of this variable offset is not determined; however, it is thought to be of electronic origin, possibly due to power supply ground reference variations, and electromagnetic pulse effects at different configurations during the scan, transients due to pulses which occur every scan, etc.

For the scanner instrument on the NOAA-9 satellite, the transmission of the housekeeping data every scan (4 sec.) produced significant transients in the electronics. To avoid the contamination of the radiometric signal by this effect, the algorithm in (23) was slightly modified so that the housekeeping data is transmitted once every eight scans. Thus, the transient occurs only once every 32 seconds, and does not contaminate the remaining seven scans. The modified algorithm is shown in Table 2.

1. Total and Longwave Channels

The total and longwave channels are calibrated using MRBB data. The data is obtained by scanning the MRBB inside the calibration chamber, after it has reached a uniform temperature set at various levels. The temperatures generally have been varied from -60° C to $+45^{\circ}$ C at six or seven different temperature levels.

The algorithm coefficients are determined directly by a least-squares method of (23) and (24) to determine AV , AVA , AHA and AD and a constant offset bias, say b , added to the offsets $\sigma_a(t)$. The offsets $\sigma_a(t)$ are obtained by scanning a uniform wall in air. The offset bias, b , represents the vacuum to air correction which is applied to the in-air-offsets,

Table 2. NOAA-9 Count Conversion Equations

$$CC(I, J, K) = GAIN(J) * (RC(I, J, K) - COFF(J, K) - SC(I, J)) \\ + OFFSET(I, J) * W(K) + \frac{AVA(J)}{VB * CVLT(J)} * OFFST1(J) * MOD(I - 1, 8)$$

where

I – Scan Counter

J – Channel Indicator

W – Sample Counter

$$GAIN(J) = AV(J) / (VB * CVLT(J))$$

$$OFFST1(J) = AHA(J) * THDIF(J) + AB(J) * ABDIF + AD(J) * VDDIF(J)$$

$$OFFSET(I, J) = (AVA(J) / (VB * CVLT(J))) * (SCDIF(I, J) + OFFST1(J))$$

$$CVLT(COUNTS/VOLTS) = 409.5$$

COEFFICIENTS	TOTAL CHANNEL	LONGWAVE CHANNEL	SHORTWAVE CHANNEL
<i>AV</i>	5493.6354	3261.6735	4221.3476
<i>AHA</i>	-17.11888	-3.90308	-15.963174
<i>AB</i>	0.0	0.0	0.0
<i>AD</i>	2.048750	0.7042702	0.0816490
<i>AVA</i>	-6302.2166	-8534.51306	-2673.2286

$$DELAY(\tau) = .046 \text{ Seconds}$$

i.e.,

$$\sigma(t) = \sigma_a(t) + b \quad (25)$$

On the other hand, the data $\hat{L}_d(t - \tau)$ is obtained by its definition in (1):

$$\hat{L}_d(t - \tau) = \int_0^\infty \tau(\lambda) L_B(\lambda, T_{BB}(t)) d\lambda \quad , \quad (26)$$

where $L_B(\lambda, T)$ is Planck's equation for a cavity at temperature T , $T_{BB}(t)$ is the average MRBB temperature at time t .

2. Shortwave Channels

Due to the unexpected non-uniformity, of the ERBE integrating sphere, the calibration procedure developed for this channel is significantly more complicated. The basic philosophy is to use the total and longwave channels as transfer standards, and calibrate the integrating sphere output using these two channels which have been MRBB-calibrated. The remaining step is to similarly use a least-squares approach to determine the algorithm coefficients. The shortwave channels were calibrated using the following procedure:

- (1) Check longwave output of integrating sphere (at nadir) using longwave channel MRBB calibrated count conversion coefficients, integrating sphere wall temperature and longwave spectral response

$$L_{sLW} = \int_0^\infty \tau_{LW}(\lambda) L_B(\lambda, T_w) d\lambda$$

- (2) Estimate shortwave output of integrating sphere (at nadir) using total channel MRBB calibration.

- a) Obtain \hat{L}_{sT} using MRBB count coefficient algorithm.
- b) Obtain $\hat{L}_{sT} - \int_0^\infty \tau_T(\lambda) L_B(\lambda, T_w) d\lambda \approx \int_0^\infty \tau_T(\lambda) [c\bar{L}_{s\lambda 1}] d\lambda$. $\bar{L}_{s\lambda 1}$ is output due to lamp.
- c) Solve for c .

(3) Compute L_{sSW}

$$L_{sSW} = \int_0^\infty \tau_{SW}(\lambda) [c\bar{L}_{s\lambda 1} + L_B(\lambda, T_w)] d\lambda$$

(3) Assumption: integrating sphere output is

$$L_\lambda = c\bar{L}_{s\lambda 1} + L_B(\lambda, T_w)$$

(4) Use integrating sphere sample 41 data (thought to be clean) at different shortwave levels and many scans to obtain count conversion coefficients.

The calibration coefficients thus obtained for the three ERBE satellites are shown in Tables 3, 4 and 5.

C. In-Flight Offset Stability.

The ERBS satellite provides a capability to test the sensor offsets for stability over a period of time. The offsets can be tested by a pitch-over maneuver where the satellite pitch angle is commanded to 180°. In this position, the sensors scan space, one of the most uniform sources provided the sun or moon are not in the field-of-view.

The stability of the scanner offsets is in question as it is related to power supply reference variations over long periods of time. Table 6 shows the variation of the offsets determined from two pitch-over maneuvers approximately one year apart, from October 1984 to October 1985. The mean variations are less than 0.27 W/m²-sr.

Table 7 shows in-flight calibration results analyzed to indicate the stability of the offsets. This also shows a relatively small variation in the offsets of as much as 0.9 W/m²-sr for the ERBS total scanner.

D. SWICS Stability.

The in-flight calibration source for the shortwave scanners, the SWICS, appears to indicate a drift in its SiPD amp output. This can be seen in Fig. 22 which shows the NOAA-9 SWICS amp output over time. The amplifier output is clearly drifting.

Table 3. ERBE ERBS (FM1) Scanner Data Interpretation Coefficients

COEFFICIENTS	TOTAL CHANNEL	LONGWAVE CHANNEL	SHORTWAVE CHANNEL
<i>AV</i>	5477.2314	3174.3511	4267.8746
<i>AHA</i>	15.604489	9.5852644	-11.568366
<i>AB</i>	0.0	0.0	0.0
<i>AD</i>	0.1164209	5.4351765	5.665687
<i>AVA</i>	-7810.8822	-8354.0546	-7968.1652

Table 4. ERBE NOAA-9 (PFM) Scanner Data Interpretation Coefficients

COEFFICIENTS	TOTAL CHANNEL	LONGWAVE CHANNEL	SHORTWAVE CHANNEL
<i>AV</i>	5695.2	3130.0	4392.0
<i>AHA</i>	139.47	-98.59	-506.26
<i>AB</i>	0.0	0.0	0.0
<i>AD</i>	182.30	-409.27	170.25
<i>AVA</i>	-7265.6	-3985.7	-4445.8

Table 5. ERBE NOAA-10 (FM2) Scanner Data Interpretation Coefficients

COEFFICIENTS	TOTAL CHANNEL	LONGWAVE CHANNEL	SHORTWAVE CHANNEL
<i>AV</i>	5773.01	3080.27	4188.21
<i>AHA</i>	-12.4677	70.8466	0.0
<i>AB</i>	0.0	0.0	0.0
<i>AD</i>	11.6246	-11.1559	0.0
<i>AVA</i>	-2811.24	-1001.32	-4941.11

Table 6. ERBS Scanner Offset Stability

ERBS SCANNER OFFSETS: (AS CURRENTLY IMPLEMENTED)

Position	Total	LW	SW
15	.85	1.52	-5.09
25	2.39	4.56	-7.63
40	2.08	4.60	-6.75
55	9.12	16.02	-4.48
65	9.54	17.33	-3.51

ERBS SCANNER OFFSETS: (AS DETERMINED FROM PITCHOVER OCT. 85)

800 scans of space

Position	Total (1 σ)	LW (1 σ)	SW (1 σ)
15	1.97 (2.25)	4.27 (4.63)	-0.71 (3.62)
25	1.61 (2.23)	6.18 (4.17)	-8.55 (4.51)
40	0.66 (2.10)	3.98 (3.73)	-8.59 (4.63)
55	6.48 (2.18)	14.39 (3.21)	-7.69 (4.15)
65	7.92 (2.24)	17.75 (3.37)	-4.17 (3.46)

$$\text{mean} = \frac{1}{N} \sum_{i=1}^n |\text{diff}_i|$$

mean (counts)	1.516	1.408	2.202
mean (W/m ² - sr)	0.243	0.134	0.271
max (counts)	2.64	2.75	4.38
max (W/m ² - sr)	0.423	0.26	0.5399

Table 7. ERBS Total Scanner

FLIGHT CALIBRATION

OFFSET STABILITY AND NOISE LEVELS

COMPARISON OF RADIANCE FALLING ON ACTIVE FLAKE

DATE	CAL. SOURCE DYNAMIC RANGE (W/m^2 - sec)	OFFSET (W/m^2 - sec)	NOISE STANDARD DEV (W/m^2 - sec)
2/06/85	101-136	5.9565	0.2960
8/07/85	106-143	5.0751	0.5659
1/22/86	107-145	5.1475	0.4996

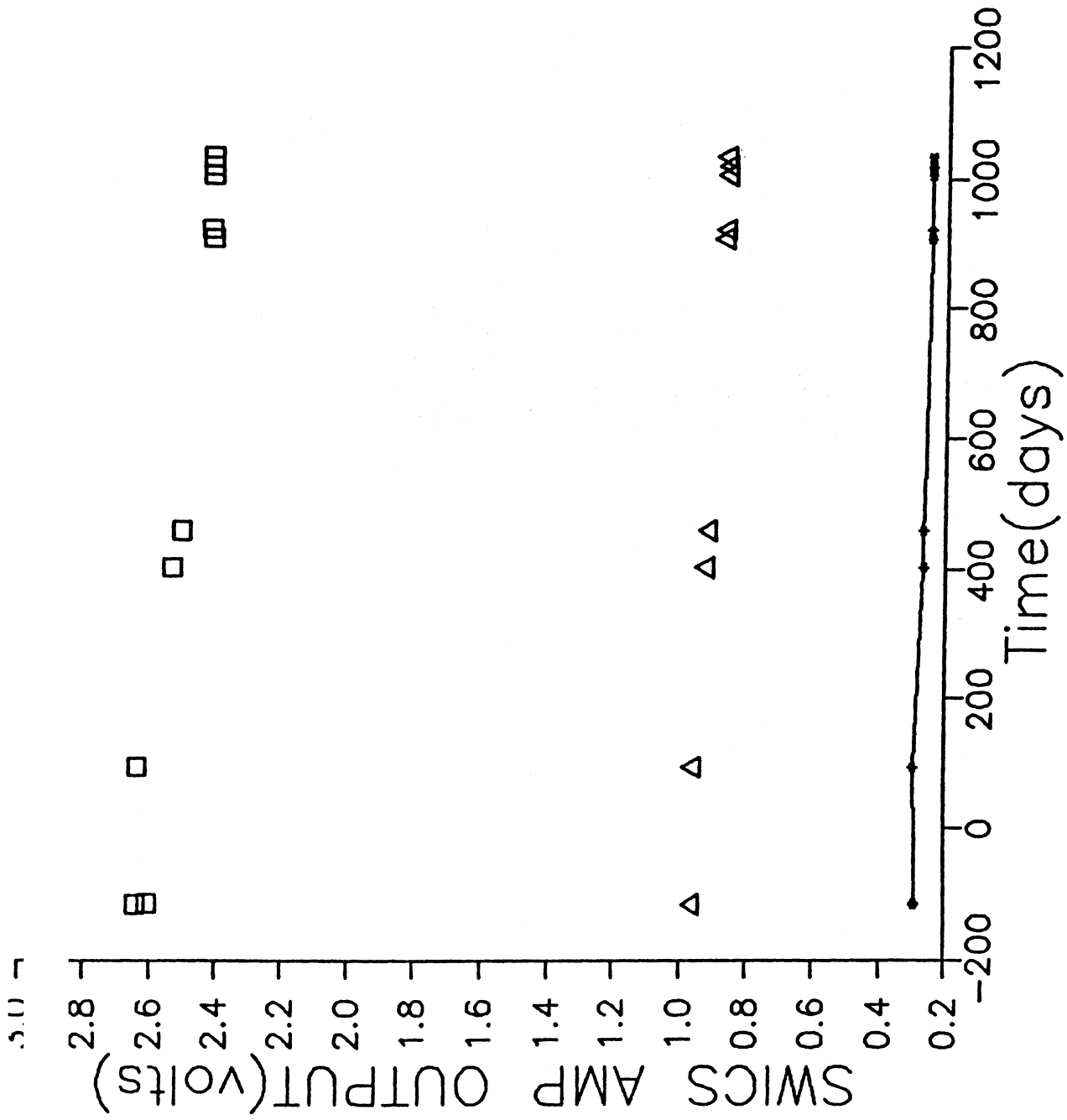


Figure 22. NOAA-9 SWICS AMP Output

However, this does not mean that the SWICS output itself is drifting. In fact, Fig. 23 implies that the drift is actually in the SWICS photodiode output, rather than its own radiative output. Figure 23 which shows the NOAA-9 shortwave scanner looking at the SWICS with its lamps on shows no drift at all. Therefore, it is more likely that the NOAA-9 shortwave sensor and the SWICS are stable while the SiPD is drifting.

E. "Striping" Algorithm.

During flight, features which appear as stripes on the data charts were observed by investigators. Closer analysis shows that, occasionally, the space clamp seems to jump to a new value, stay there for several scans, then jump back to a new value. However, the earth-viewing portion of the scan did not appear to be influenced by this phenomenon. So that, at every jump of the space clamp, all the values would also show a jump with the appearance of a stripe. This "striping" phenomenon has been noted on the ERBS and NOAA-9 scanners, but not so far on NOAA-10. The following empirical algorithm has been implemented with significant reduction of this effect.

1. Read a record from the telemetry tape.
2. Calculate the zero radiance at the internal calibration position (sample 74).
3. Compare this to the space clamp.
4. If the difference between the space clamp and the zero radiance at the internal calibration position is greater than a threshold (≈ 5 counts), then check to see which value has the greatest dispersion (using a window which includes the value of interest and 4 values ahead and behind it).
5. Replace the space clamp with the internal calibration radiance if the space clamp's dispersion is greater than the zero radiance at internal calibration dispersion. (Note, the threshold and dispersion tests are bypassed for all 3 channels if the scanner is not in the normal scan mode and for the shortwave channel if the scanner is performing an internal calibration.)
6. Store the revised telemetry record on a direct access file which resides on a removable

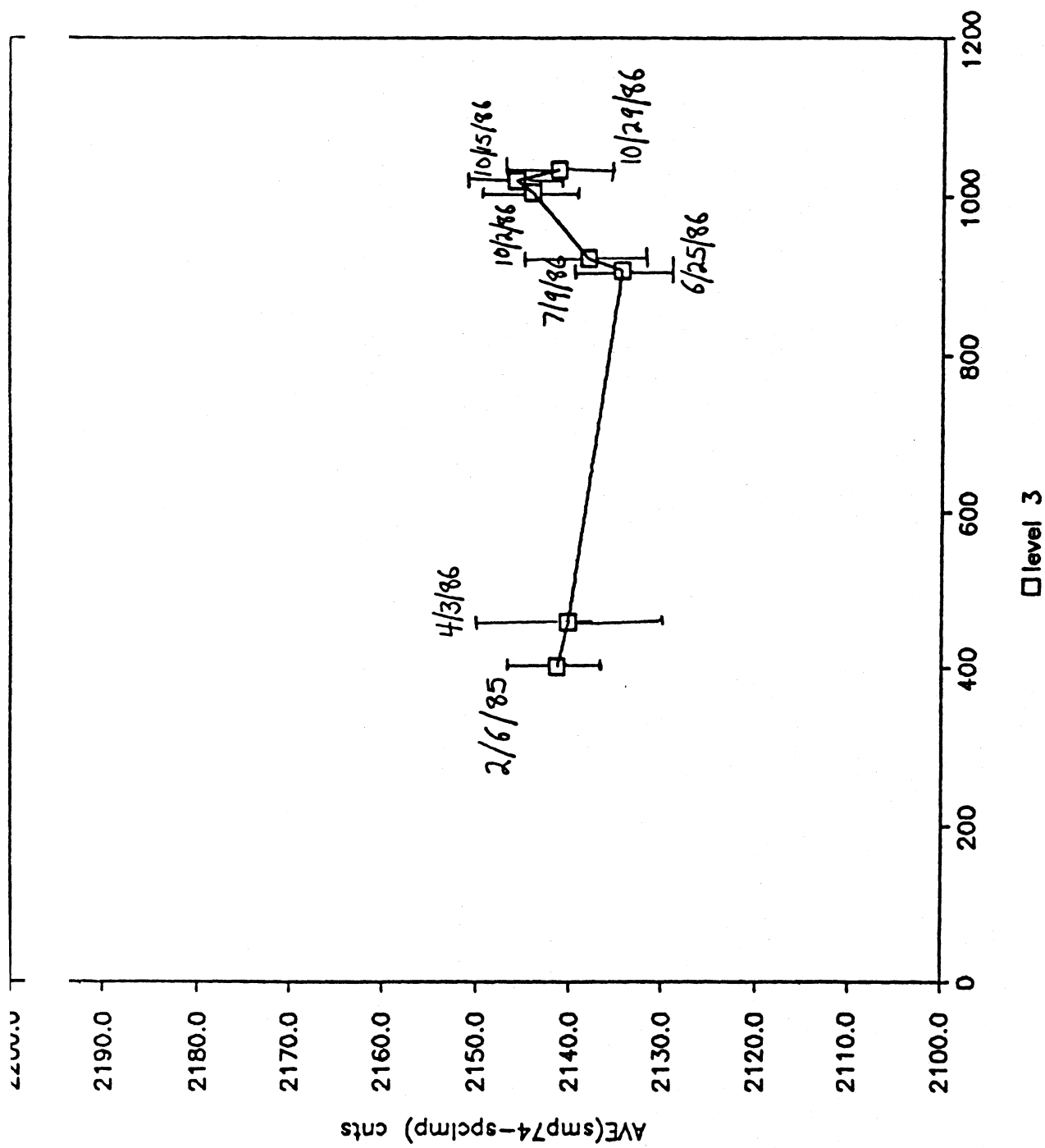


Figure 23. NOAA-9 Scanner SW Channel: SWICS Data

disk pack. (Note, this is a temporary file which is purged at the end of the run.)

REFERENCES

1. Barkstrom, B. R., "The Earth Radiation Budget Experiment (ERBE)," *Bull. Am. Meteorol. Soc.*, 65, (11), 1170-1185, 1984.
2. Barkstrom, B. R. and G. L. Smith, "The Earth Radiation Budget Experiment: Science and Implementation," *Rev. Geophys.*, 24, No. 2, 379-390, May 1986.
3. Halyo, N. and S. T. Stallman, "A Parametric Study of Aliasing Error for a Narrow Field of View Scanning Radiometer," NASA CR-3294, 1980.
4. Huck, F. O., S. K. Park, N. Halyo and S. T. Stallman, "Aliased Noise in Radiometric Measurements," *NASA Tech. Pap. 1639*, May 1980.
5. Halyo, N., S. H. Choi, D. A. Chrisman, Jr. and R. W. Samms, "Development of Response Models for the Earth Radiation Budget Experiment (ERBE) Sensors: Part 1 - Dynamic Models and Computer Simulations for the ERBE Nonscanner, Scanner and Solar Monitor Sensors," NASA CR-178292, 1987.
6. Carman, S. L., "Deep Concentric Grooves Enhance Blackbody Spectral and Spatial Uniformity," *Proc. SPIE Int. Soc. Opt. Eng.*, 416, 178-186, 1983.
7. Carman, S. L. and R. J. Hesser, "An Integrating Sphere as a Precision Radiometric Calibration Source," *Proc. SPIE Int. Soc. Opt. Eng.*, 416, 111-118, 1983.
8. Kopia, L. P., "Earth Radiation Budget Experiment Scanner Instrument," *Rev. Geophys.* 24, No. 2, 400-406, May 1986.
9. Halyo, N. and D. B. Taylor, "Explicit Solution of the Spectral Radiance in Integrating Spheres with Application to the Earth Radiation Budget Experiment Ground Calibration," *J. Opt. Soc. Am. A*, 5, No. 4, 520-534, April 1988.

Report Documentation Page

1. Report No. NASA CR-181818		2. Government Accession No.		3. Recipient's Catalog No.	
4. Title and Subtitle Modeling and Characterization of the Earth Radiation Budget Experiment (ERBE) Nonscanner and Scanner Sensors				5. Report Date March 1989	
				6. Performing Organization Code	
7. Author(s) Nesim Halyo, Dharendra K. Pandey, and Deborah B. Taylor				8. Performing Organization Report No. FR-688104	
				10. Work Unit No. 665-45-30-01	
9. Performing Organization Name and Address Information & Control Systems, Incorporated 28 Research Drive Hampton, VA 23666				11. Contract or Grant No. NAS1-18018	
				13. Type of Report and Period Covered Contractor Report	
12. Sponsoring Agency Name and Address National Aeronautics and Space Administration Langley Research Center Hampton, VA 23665-5225				14. Sponsoring Agency Code	
15. Supplementary Notes Langley Technical Representative: Robert J. Keynton Final Report					
16. Abstract The Earth Radiation Budget Experiment (ERBE) is making high-absolute-accuracy measurements of the reflected solar and earth-emitted radiation as well as the incoming solar radiation from three satellites: ERBS, NOAA-9 and NOAA-10. Each satellite has four earth-looking non-scanning radiometers and three scanning radiometers. A fifth non-scanner, the solar monitor, measures the incoming solar radiation. This report describes the development of the ERBE sensor characterization procedures using the calibration data for each of the earth-looking non-scanners and scanners. Sensor models for the ERBE radiometers are developed including the radiative exchange, conductive heat flow and electronics processing for transient and steady state conditions. The steady state models are used to interpret the sensor outputs, resulting in the data reduction algorithms for the ERBE instruments. Both ground calibration and flight calibration procedures are treated and analyzed. The ground and flight calibration coefficients for the data reduction algorithms are presented.					
17. Key Words (Suggested by Author(s)) Earth Radiation Budget Experiment, sensor modeling, calibration, characterization, data reduction algorithm, active cavity radiometer, non-scanning radiometer, thermistor bolometer, scanning radiometer, ground calibration, flight calibration			18. Distribution Statement Unclassified - Unlimited Subject Category 47		
19. Security Classif. (of this report) Unclassified		20. Security Classif. (of this page) Unclassified		21. No. of pages 182	
				22. Price A09	